Ph.D Thesis
박사 학위논문

Artificial Tactile System and Signal Processing for Haptic applications

Minkyung Sim(심 민 경 沈 玟 炅)

Department of
Information and Communication Engineering

DGIST

2021

Ph.D Thesis
박사 학위논문

Artificial Tactile System and Signal Processing for Haptic applications

Minkyung Sim(심 민 경 沈 玟 炅)

Department of
Information and Communication Engineering

DGIST

2021

Artificial Tactile System and Signal Processing for Haptic applications

Advisor: Professor Jae Eun Jang
Co-advisor: Professor Cheil Moon

by

Minkyung Sim

Department of Information and Communication Engineering
DGIST

A thesis submitted to the faculty of DGIST in partial fulfillment of the requirements for the degree of Doctor of Philosophy in the Department of Information and Communication Engineering. The study was conducted in accordance with Code of Research Ethics.[1]

November. 26. 2020

Approved by

Professor Jae Eun Jang (signature)
(Advisor)

Professor Cheil Moon (signature)
(Co-Advisor)

[1] Declaration of Ethical Conduct in Research**:** I, as a graduate student of DGIST, hereby declare that I have not committed any acts that may damage the credibility of my research. These include, but are not limited to: falsification, thesis written by someone else, distortion of research findings or plagiarism. I affirm that my thesis contains honest conclusions based on my own careful research under the guidance of my thesis advisor.

Artificial Tactile System and Signal Processing for Haptic applications

Minkyung Sim

Accepted in partial fulfillment of the requirements for the degree of Doctor of Philosophy.

November. 26. 2020

Head of Committee	문 제 일 (signature)	Prof. Cheil Moon
Committee Member	장 재 은 (signature)	Prof. Jae Eun Jang
Committee Member	최 지 웅 (signature)	Prof. Ji-Woong Choi
Committee Member	황 재 윤 (signature)	Prof. Jae Youn Hwang
Committee Member	이 정 협 (signature)	Prof. Junghyup Lee

Ph.D/IC
201322008

심 민 경. Minkyung Sim. Artificial Tactile System and Signal Processing for Haptic applications. Department of Information and Communication Engineering. 2021. 124p. Advisors Prof. Jae Eun Jang, Co-Advisors Prof. Cheil Moon

ABSTRACT

Human have the ability to interact with the external environment through five main senses which are vision, hearing, smell, taste and touch. Most of all, the sensation like vision or hearing have been well developed and the use of various applications like TV, Camera, or artificial cochlear have been widely generalized. As the next steps, recently, the tactile sensor to mimic the tactile system of human have been attracted by many groups. Especially, after the development of Apple's iPhone, the public interest about touch sensing applications have been increased explosively. Other researches for tactile sensing have focused on enhancing the performance of tactile sensor like the sensitivity, stability, response time and so on. As a result, there are some researches that the sensor performance of certain criteria is better than that of human tactile system. However, a human tactile system is not only very sensitive but also complex. In other words, ultimately, the tactile system mimicking the human tactile sensation should detect various parameters such as the pressure, temperature, hardness or roughness and also decide the psychological feeling like the pain by a hot material in touching or the smooth/roughness feeling in sliding the certain material. Therefore, in this thesis, it has been studied for the development of multifunctional tactile sensing system detecting various tactile parameters and deciding the kinds of psychological tactile feeling by measured stimulation.

As the first step for the development of tactile system, we have studied the tactile sensor using ZnO nanowire. Therefore, in this chapter, the basic characteristics of ZnO nanowire are investigated to confirm the possibility for the tactile sensor. In addition, structural design factors of sensor units have been studied in order to enhance the sensitivity of ZnO nanowire-based tactile sensor. We have primarily demonstrated the effect of a square pattern array design in a pressure sensor using ZnO nanowires. Nanowires grown on the edge of cells can be bent easily because of growth direction, density of nanowires, and buckling effect. Since smaller square pattern arrays induce a higher circumference to cell area ratio, if one sensor unit consists of many micro-level square pattern arrays, the design enhances the piezoelectric efficiency and the sensitivity. As a result, 20um × 20um cell arrays showed three times higher pressure sensitivity than 250um × 250um cell array structures at a pressure range from 4kPa to 14kPa. The induced piezoelectric voltage with the same pressure level also increased drastically. Therefore, the smaller pattern array design is more appropriate for a high-sensitive pressure sensor than a simple one-body cell design for tactile systems, and it has the advantage of better power efficiency, which is also important for artificial tactile systems.

Even if, in previous experiments, the possibility of piezoelectric materials as the tactile sensor and the method for the enhancement of pressure sensitivity are confirmed well, the tactile sensor for mimicking the human tactile sensation should measure various parameters as well as the pressure. However, many studies about 'smooth-rough' sensation depend on the machine learning technology with simple tactile sensors rather than developing the sensors that can measure various parameters like surface topography, hardness, quality of

materials at the same time. Therefore, after the development of the pressure sensor, specific structures based on PDMS are proposed to measure and analyze above-mentioned parameters related to 'smooth-rough' decision, as like fingerprint of human. To find the optimized structure, three kinds of the structure shape (cone, cylinder and dome) are fabricated and the pressure sensitivity according to the shape are also measured. FEM simulation is also carried out to support the experimental result. Our tactile sensor with optimized dome structure (500um height) provides high shear force sensitivity, fast response time, stability, and durability. The high sensitivity about the shear force enables better the tactile sensor to measure the various surface information such as the pitch of pattern, the depth, the sliding velocity, the hardness and so on.

In addition, after the study to measure the various surface information by dome structure, the research to measure the other surface information is also followed. In our previous study, we confirmed that the surface topography can be reconstructed by mapping the piezoelectric signals according to the location. In this research, to reduce the number of measurements from dozens to once and minimize the data loss at the empty space between adjacent sensors, the electrode array of Zig-Zag type is applied to the tactile sensor. As a result, with just one measurement, the surface topography of broad region can be successfully reconstructed by our tactile sensor as the high-resolution image. Additionally, the temperature sensor based on the resistive mechanism is fabricated between the Zig-Zag electrode lines to measures the temperature of surface materials when the tactile sensor rubs on the materials in real time.

Over the development of the tactile sensing applications, the demand for an artificial system like human tactile sensation have been much more increased. Therefore, in this study, as a surrogate for human tactile sensation, we propose an artificial tactile sensing system based on the developed sensors in previous sections. For this, the piezoelectric tactile signal generated by touching and rubbing the material is transferred to DAQ system connected with our tactile sensor. First, the system decides whether the contacted material is dangerous or not. If dangerous like sharp or hot materials, the warning signal is generated by our artificial tactile system. If not, the sensor connected with the system rubs the materials and detects the roughness of the materials. Especially, the human test data related to 'soft-rough' detection is applied to a deep learning structure allowing personalization of the system, because tactile responses vary among humans. This approach could be applied to electronic devices with tactile emotional exchange capabilities, as well as various advanced digital experiences.

In this thesis, human-like tactile sensing system based on the piezoelectric effect is successfully confirmed through various experiments. Although there are still some issues that need to be improved, this research is expected to be fundamental results for human-like tactile sensing system detecting a variety of the parameters such as the pressure, temperature, surface morphology, hardness, roughness and so on. In the future, through collaborative research with other fields like brain science, signal processing, we hope that this research can mimic psychological tactile sensations and communicate emotional exchange with external environment like real human skin.

Keywords: Artificial Tactile sensor, Piezoelectric effect, ZnO nanowire, PVDF-TrFE, Pressure sensor, Temperature sensor, Roughness sensor.

List of Contents

List of Tables

List of Figures

I. INTRODUCTION

1.1 Motivation

Humans have interacted with the external environment by five main senses, which are vision, hearing, smell, taste and touch in real time. To avoid the dangerous situation or communicate with other people easily, the real-time data perceived from these five senses is important and if humans lose any other of the five senses like disabled person, it would be very inconvenient. In addition, recently, with the development of artificial intelligence technology, the interest to develop the humanoid robot have been also dramatically increased.[1-8] Developed humanoids should detect various information using artificial five senses. Therefore, it is very attractive topic to develop bio-mimicking applications for replacing the five senses.

Among these senses, the applications mimicking the vision and hearing have been developed a lot in the form of Camera, TV, recorder and speaker. There are also many tactile applications based on the pressure sensor with various sensing mechanism. Ultimately, future tactile applications should detect various stimuli such as a temperature, roughness, hardness, shape as well as the pressure. Also, artificial tactile sensing system similar to human tactile feeling process should be developed like Figure 1.1. However, the level of development of the tactile applications similar to human skin is very low comparing these results. This is because there are various mechanoreceptors required to be mimicked in following Figure 1.2[9]. and the tactile sensing mechanism of human is not investigated from a bioengineering point of view, perfectly. Various parameters, such as their shape, size, hardness, friction, temperature, texture, vibration, and so on, can be measured by these tactile receptors in human skin.[9-12] Based on the information measured from the tactile receptors, the tactile sense plays a significant role in many aspects of life, such as grasping, and perceiving

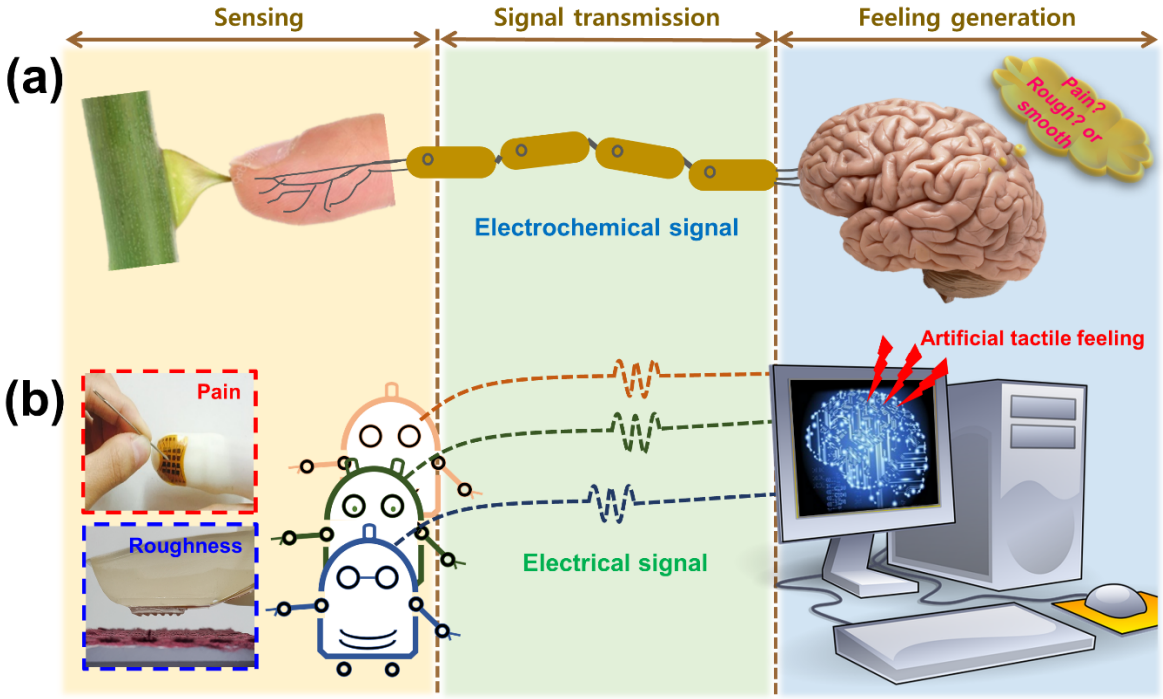

Figure 1.1. A schematic image of tactile feeling process of (a) humans and (b) artificial tactile system.

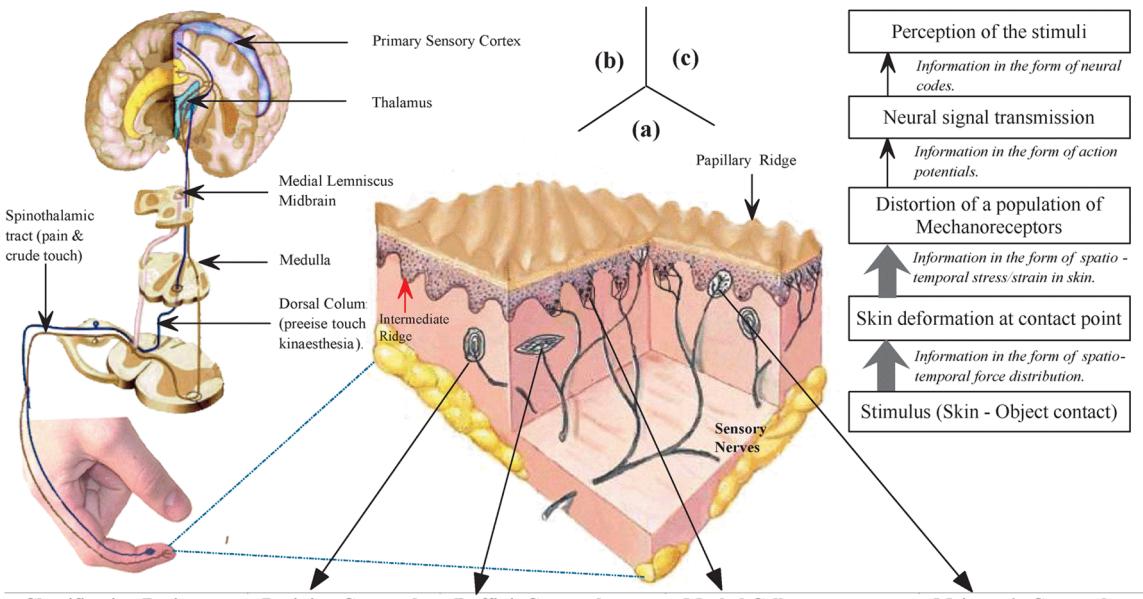

Classification Basis		Pacinian Corpuscle	Ruffini Corpuscle	Merkel Cells	Meissner's Corpuscle
Type		FA II	SA II	SA I	FA I
Adaptation Rate		Fast	Slow	Slow	Fast
Spatial Acuity (mm)		10+	7+	0.5	3-4
Vibration/rapid indent. threshold	Best(μm)	0.01	40	8	2
	Mean(μm)	0.08	300	30	6
Stimuli Frequency (Hz)		40-500+	100-500+	0.4-3	3-40
Conduction Velocity (m/s)		35-70	35-70	40-65	35-70
Effective Stimuli		Temporal changes in the skin deformation	Sustained downward Pressure; Lateral skin stretch; Skin slip.	Spatial deformation; Sustained pressure; Curvature, edge, corners.	Temporal changes in skin deformation
Sensory Function		High frequency vibration detection; Tool use.	Finger position; Stable grasp; Tangential Force; Motion direction	Pattern/form detection; texture perception; Tactile flow perception.	Low frequency vibration & motion detection; Grip control; Tactile flow perception.

Figure 1.2. The various mechanoreceptors in human skin[9]

objects.[13-20] So, to replace the receptors, there are various transduction mechanisms, such as the resistive[21-25], capacitive[26-30], piezoelectricity[31-35], triboelectricity[36-40] and so on, converting external stimulation to electrical signal. Because the merit and demerit are various and different according to each transduction mechanism in Table 1.1, better mechanism than others can't be decided. Among various mechanisms, after a great success of the touch screen application of Apple's iPhone, the capacitive sensing mechanism has been much used in industrial fields due to their various advantage such as high sensitivity, large-area fabrication, multi-touch ability, wiring problems and so on. Even if commercialized touch applications show the excellent performance to measure and detect the pressure and pressed position, the demand for the human-like tactile device have been gradually increased in the field of medical or robotic engineering. Over the tactile applications based on the pressure sensor, the future device should detect the various stimuli such as the pressure, temperature, smooth/roughness of the surface and so on. Furthermore, basic tactile senses based on such physical parameters, humans have the ability to detect and form psychological feelings for sensations such as warmth, softness, roughness, smoothness and pain. These psychological feelings enrich human interactions with others and with objects, and are too important to be neglected in human lives. However, unfortunately, most studies of artificial tactile sensors so far have focused on increasing sensitivity to physical parameters such as pressure, strain and temperature.[41-46] In addition, the integration of different sensors measuring various physical parameters currently requires a bulky structure and complex fabrication processes, and is less reliable as well.[47-50]. Therefore, the development of novel tactile sensor detecting various parameters, fabricated simply, and deciding the psychological feeling based on the parameters has been constantly required.

Transduction mechanism	**Advantage**	**Disadvantage**
Capacitive	➢ High sensitivity ➢ Low cost ➢ Multi – touch ➢ High spatial resolution	➢ Hysteresis ➢ Complex electronics ➢ Power consumption ➢ Limited sensing range ➢ Response time
Resistive	➢ Low cost ➢ Easy electronics ➢ Simple fabrication ➢ Low noise	➢ Poor durability ➢ Hysteresis ➢ Temperature sensitive ➢ Response time ➢ Power consumption
Triboelectricity	➢ Self-power system ➢ Simple fabrication ➢ High output	➢ Durability ➢ Limited sensing range ➢ High impedance ➢ Response time
Piezoelectricity	➢ Dynamic response ➢ Self-power system ➢ High bandwidth ➢ High sensitivity	➢ Static response ➢ Low spatial resolution ➢ Thermal dependent ➢ Repeatability

Table 1.1. The advantages and disadvantages of various transduction mechanisms.

Here, the researches for the development of a self-powered multifunctional tactile sensor detecting various parameters and fabricated simply have been accomplished using the piezoelectric effect. Our sensor can measure a variety of parameters like the pressure with high sensitivity, hardness, depth, pitch of pattern, surface topography and temperature and so on. Additionally, the novel tactile senor should communicate with human or humanoid robots as the concept of the psychological feeling to replace the tactile sense in reality. Therefore, in the future, it is one of the interest research topics combining the measured parameters with the deep learning process to replace the tactile and psychological feeling mechanism of human not investigated.

1.2 Various transduction mechanisms for the tactile sensor

1.2.1 Capacitive mechanism

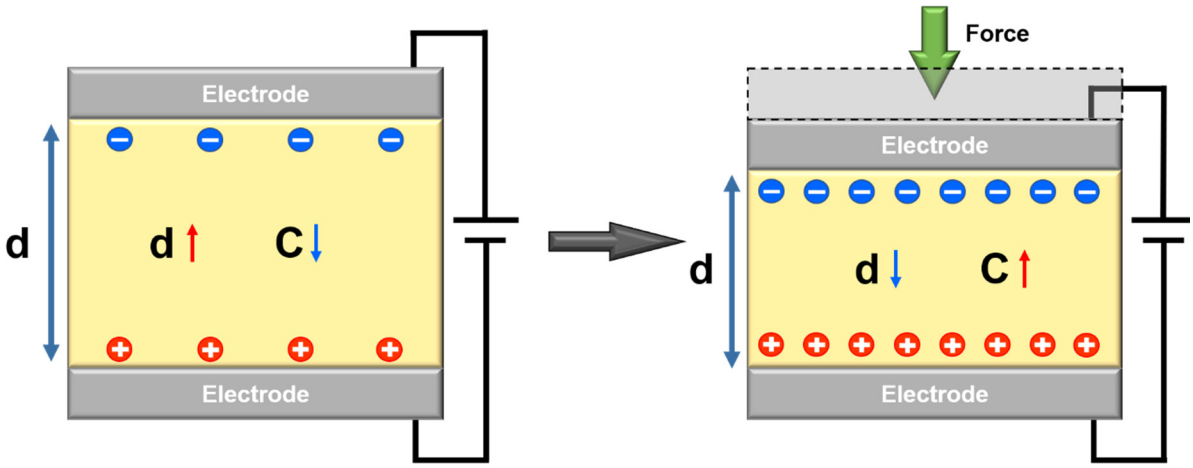

Figure 1.3. The principle schematic of capacitive tactile sensor

The capacitance C of a parallel plate capacitor is expressed by following equation (1.1).

$$C = \varepsilon_0 \varepsilon_r {}^{A}/_{d} \tag{1.1}$$

ε_0 is the free space permittivity, ε_r is relative permittivity, A is the area, and d is the distance between electrodes in Figure 1.3. The pressure or tactile sensor based on the capacitive mechanism detects the change of these parameters (A, and d). The normal force is detected by changing the distance d and the change of area A is related to the shear force.[51-54] The advantage of capacitive mechanism are high sensitivity, compatibility and low power consumption. However, the smaller capacitance with small area A is applied to the device for high resolution, the poorer the signal-to-noise ratio occur.[55] The specific external source or parasitic capacitance can interrupt the operation of sensor based on capacitive mechanism. In addition, elastomer dielectric materials to fabricate the capacitive sensor result in the degradation of sensitivity or response time.

1.2.2 Resistive mechanism

Resistive sensors measure the pressure level by the resistance changes when the external force is applied to the tactile sensor. The principle of resistive sensor is demonstrated in Figure 1.4. Although, there are various mechanisms changing the resistance such as conductive polymer, percolation, quantum tunneling, and so on (Figure 1.5), the principle changing the resistance by conduction path is a common factor.

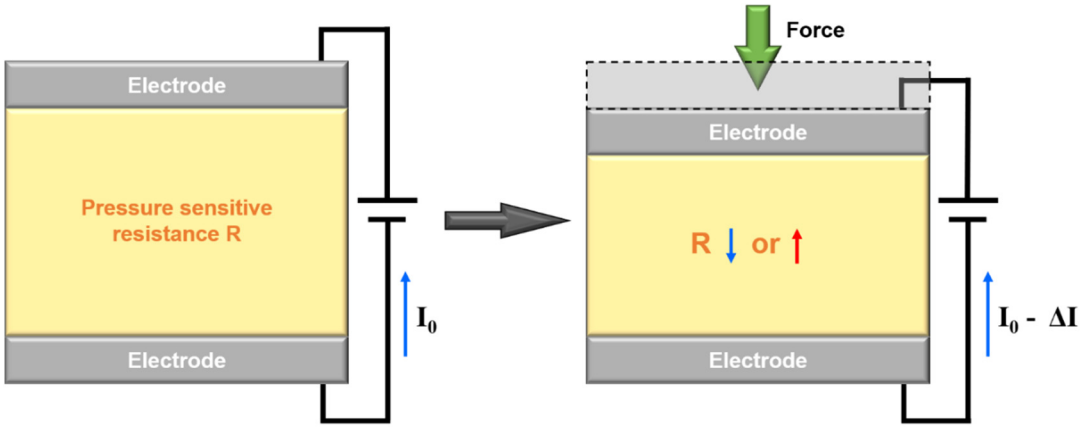

Figure 1.4. The working principle of tactile sensor using resistive mechanism

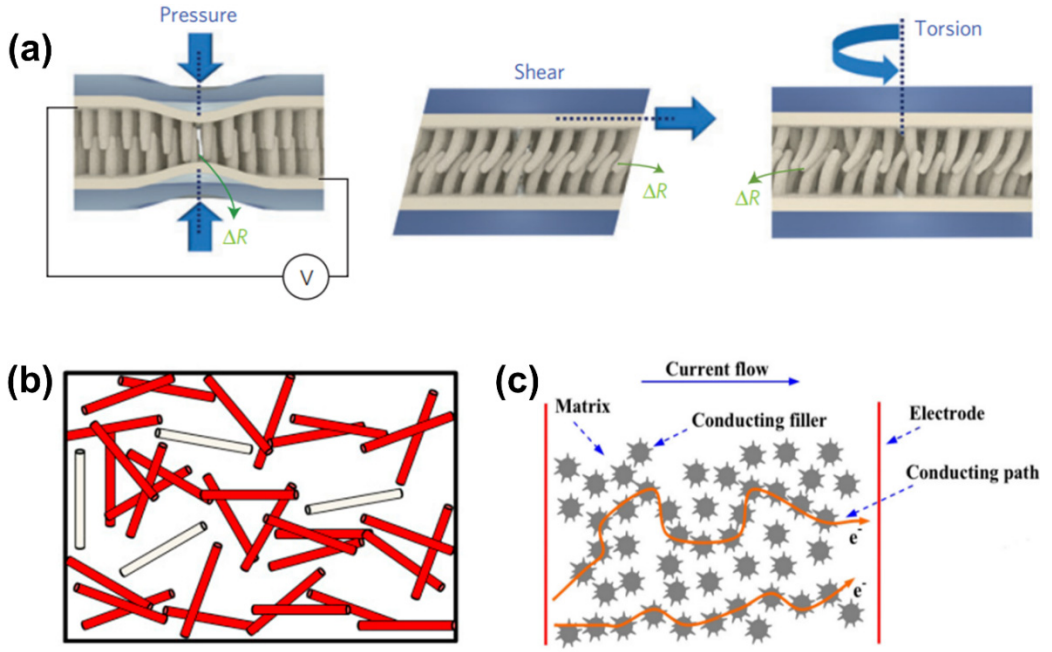

Figure 1.5. The various mechanism for resistive tactile sensor. (a) interlocked structure[56], (b) percolation mechanism[57], (c) quantum tunneling mechanism[58] to control the resistance.

1.2.3 Triboelectric effect

Triboelectric effect is the relationship between the mechanical energy and electric energy similar to the piezoelectric effect.[59] However, this effect is generated by the difference of electron affinity when two different materials are in contact with each other. For example, if certain material has higher electron affinity than that of other material, it will tend to take the electrons from the other materials. The triboelectric series is the table arranging the difference of electron affinity among various materials in Figure 1.6. In this series, the materials of positive direction (positively charged) tend to give the electrons to the materials toward the bottom (negatively charged). Then, the more difference of electron affinity between two materials is, the higher the triboelectric effect can be generated.

Generally, the sensing application by triboelectric effect is based on the triboelectric effect-nanogenerator (TENG). The working principle is demonstrated in following Figure 1.7. In Figure 1.7(a), When two different materials are in contact with each other, the surface charges are induced with opposite polarity determined by the difference of electron affinity in accordance with triboelectric series. After the accumulation of surface triboelectric charges by external pressure, the charge flow through external circuit is generated to balance the electric potential difference between electrodes during releasing in Figure 1.7(b) to (d). Even if the triboelectric effect has various advantages such as self-powered characteristic with high output, low cost, light, simple fabrication, conversion efficiency, this mechanism could not be suitable for electronic skin due to several drawbacks such as the durability, limited pressure range and stability under humidity environment and temperature sensing ability.

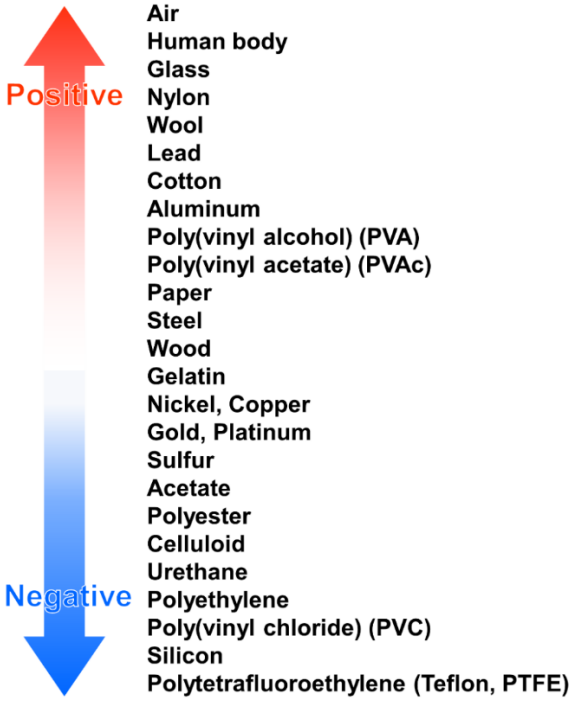

Figure 1.6. A conventional triboelectric series of oxide dielectric materials.

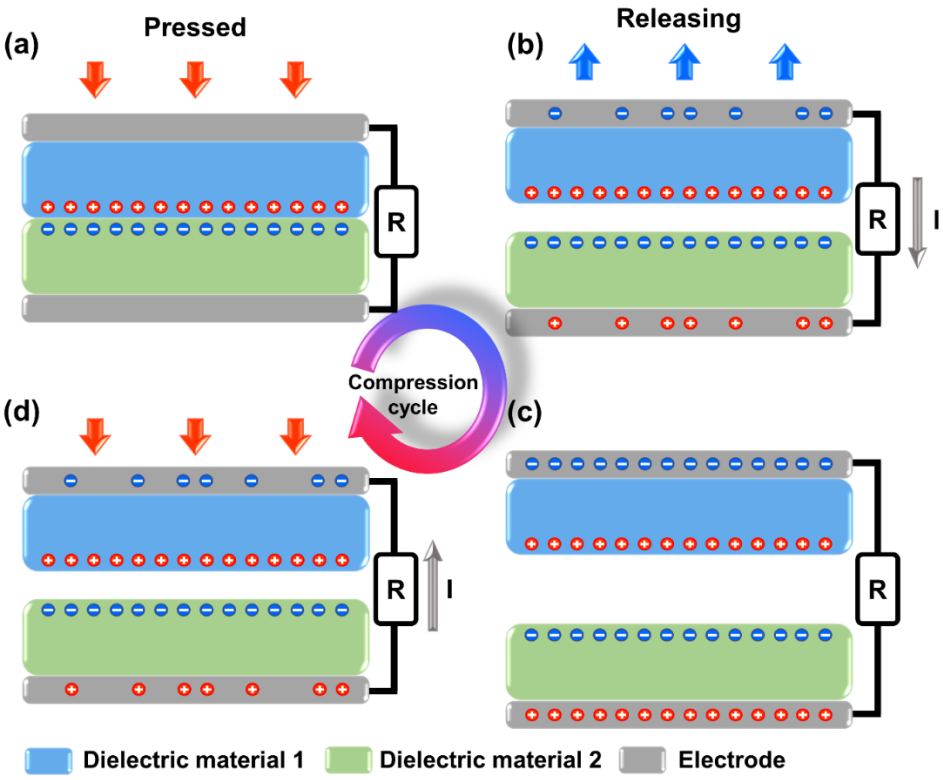

Figure 1.7. Working principle of triboelectric nanogenerator. (a) triboelectrification process by external force, (b) the electrostatic induction during release, (c) balanced potential difference state by no external force, (d) the electrostatic induction through an external circuit to balance the potential by external force.

1.2.4 Piezoelectric effect

In NaCl-type cubic materials, whether the external force is applied, the center of negative and positive charge is coincided in the unit cell of general crystal structure. Therefore, net polarization is not generated along the unit cell and P = 0 like Figure 1.8. On the other hand, certain crystalline materials are polarized along the structure if they are mechanically stressed like Figure 1.9. When deformed by the external force, at the surfaces of the material, charges by the polarization are accumulated. As a result, the voltage difference along the materials is generated by accumulated charges and this is named as the piezoelectric effect. This effect results from no center of symmetry of piezoelectric materials unlike other materials in Figure 1.8. As mentioned above, the piezoelectric effect is the conversion relationship between the mechanical and electrical energy in certain solid materials having no center of symmetry.[60] There are two piezoelectric effect by conversion situations.[61] One is the direct piezoelectric effect and the other is the converse piezoelectric effect. Two piezoelectric effect are demonstrated in following Figure 1.10. The direct piezoelectric effect generates the electrical polarization along the materials by the strain or deformation of the material structure in Figure 1.10(a). Whereas the converse piezoelectric effect is the deformation of material structure when the external electric field is applied to the piezoelectric material in Figure 1.10(b). The direct piezoelectric effect is demonstrated by following equation.

$$D_i = d_{ij} T_j \tag{1.2}$$

In this equation, D_i is the piezoelectric displacement along i direction, T_j is the applied mechanical stress along the j direction and d_{ij} is the piezoelectric coefficient of i direction when the external stress of j direction is applied to the piezoelectric materials.

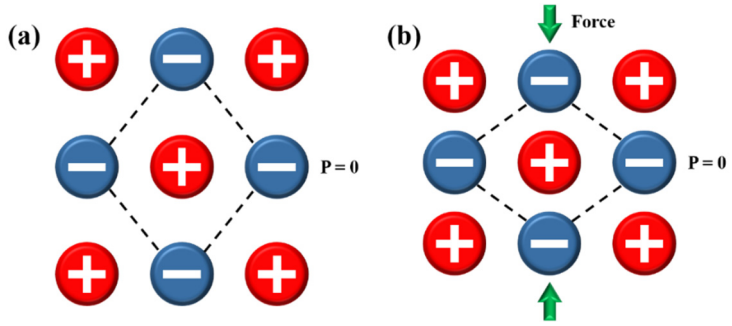

Figure 1.8. A cubic unit cell of certain materials having a center of symmetry. Coincident center of negative and positive charge (a) without and (b) with external force.

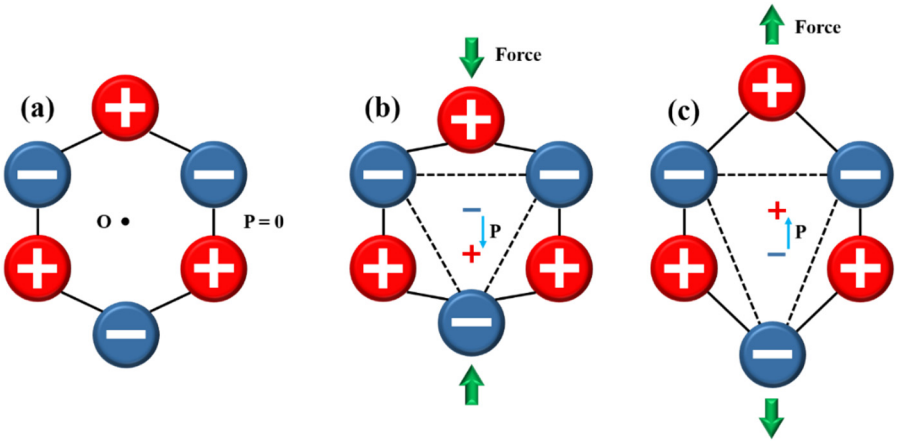

Figure 1.9. Hexagonal structure of piezoelectric materials. (a) neutral case coinciding the center of negative and positive charge without external force and polarized case along the structure by (b) compressive and extensive force.

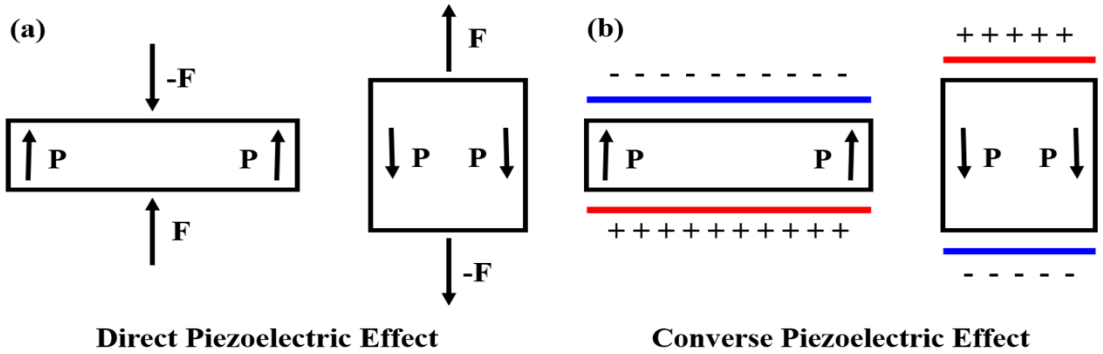

Figure 1.10. The schematic of direct and converse piezoelectric effect, (a) direct piezoelectric effect, (b) converse piezoelectric effect.

The converse piezoelectric effect related to the electrical field and strain is manifested by following equation.

$$S_j = d_{ij}E_j \tag{1.3}$$

In this equation, S_j is the induced strain and E_j is the applied electrical field along the j direction, respectively. Based on previous equation, the piezoelectric current and voltage by external force is demonstrated like following equations.

$$D_i = \frac{Q_{piezo}}{A} = d_{ij}\frac{F_j}{A} \tag{1.4}$$

$$Q_{piezo} = d_{ij}F_j \tag{1.5}$$

$$I_{piezo} = \frac{dQ_{piezo}}{dt} = \frac{d(d_{piezo}F)}{dt}, \qquad V_{piezo} = I_{piezo}R \tag{1.6}$$

1.3 Objectives

Here, this dissertation demonstrates a self-powered multi-functional tactile sensor system based on the piezoelectric effect to detect various surface information, such as the pressure, temperature, hardness, surface topography and so on. For this, three main objectives are demonstrated in following sections.

First is the study to enhance the piezoelectric effect and sensitivity of ZnO based-tactile sensor. In this study, unlike other researches, the structural solution is proposed by patterning the forest of ZnO nanowire and proved by FEM simulation. This method simply increases the piezoelectric efficiency without other annealing at high temperature or doping process.

Second, to effectively collect the surface information from the piezoelectric tactile sensor, the special structure based on PDMS is demonstrated to amplify the signal from the materials surface. By dome structure, the piezoelectric signal by the interaction between the tactile sensor and surface topography is amplified and the specific information like hardness, depth, the pitch of pattern and surface structure can be measured effectively.

Then, because the tactile sensing results from complex information of touched materials, third objective is to develop the multi-functional tactile sensor to detect various surface information. So, Zig-Zag arrayed tactile sensor is designed to reconstruct the surface topography based on measured piezoelectric signal and detect the temperature in sliding or touching.

1.4 Reference

[1] K. Hirai, M. Hirose, Y. Haikawa and T. Takenaka, "The development of Honda humanoid robot," Proceedings. 1998 IEEE International Conference on Robotics and Automation (Cat. No.98CH36146), Leuven, Belgium, 1998, pp. 1321-1326 vol.2

[2] K. Rajan and A. Saffiotti, “Towards a science of integrated AI and Robotics”, Artificial Intelligence, 247, 2017, pp. 1-9.

[3] L. Kunze, N. Hawes, T. Duckett, M. Hanheide and T. Krajník, "Artificial Intelligence for Long-Term Robot Autonomy: A Survey," IEEE Robotics and Automation Letters, 3(4), 2018, pp. 4023-4030.

[4] M. Asada, K. F. MacDorman, H. Ishiguro, and Y. Kuniyoshi, “Cognitive developmental robotics as a new paradigm for the design of humanoid robots”, Robotics and Autonomous System, 3(2), 2001, pp. 185-193.

[5] J. Torresen, “A review of future and ethical perspectives of robotics and AI”. Frontiers in Robotics and AI, 4, 2018, 75

[6] W. He, W. Ge, Y. Li, Y. Liu, C. Yang and C. Sun, "Model Identification and Control Design for a Humanoid Robot," IEEE Transactions on Systems, Man, and Cybernetics: Systems, 47(1), 2017, pp. 45-57

[7] R. R. Murphy, Introduction to AI robotics, MIT press, 2019.

[8] M. Chen, J. Zhou, G. Tao, J. Yang and L. Hu, "Wearable Affective Robot," IEEE Access, 6, 2018 pp. 64766-64776.

[9] R. S. Dahiya, G. Metta, M. Valle and G. Sandini, "Tactile Sensing—From Humans to Humanoids," in *IEEE Transactions on Robotics*, 26(1), 2010, pp 1-20.

[10] Tactile sensing for dexterous in hand manipulation in robotics-a review

[11] C. H. Lin, T. W. Erickson, J. A. Fishel, N. Wettels and G. E. Loeb, "Signal processing and fabrication of a biomimetic tactile sensor array with thermal, force and microvibration modalities," *2009 IEEE International Conference on Robotics and Biomimetics (ROBIO)*, Guilin, 2009, pp. 129-134

[12] S. J. Lederman and R. L. Klatzky, *Cognitive. Psychol*. **1987**, *19*, 342.

[13] J. Kim. et al., Stretchable silicon nanoribbon electronics for skin prosthesis, Nat. Commun 2014, 5, 5147.

[14] J. Lee. et al., Highly Sensitive and Multifunctional Tactile Sensor Using Free-standing ZnO/PVDF Thin Film with Graphene Electrodes for Pressure and Temperature Monitoring. Sci. Rep. 2015, 1, e1500661.

[15] V. Maheshwari, R. F. Saraf, High-resolution thin-film device to sense texture by touch. Science, 2006, 312, 1501-1504.

[16] R. S. Dahiya, G. Metta, M. Valle, G. Sandini, Tactile sensing—from humans to humanoids. IEEE Trans. Robot, 2010, 26, 1-20.

[17] H. Yousef, M. Boukallel, K. Althoefer, Tactile sensing for dexterous in-hand manipulation in robotics—a review. Sensor. Actuat. A-Phys, 2011, 167, 171-187.

[18] L. A. Huet, J. W. Rudnicki, and M. J. Z. Hartmann, Tactile Sensing with Whiskers of Various shape: Determining the Three-Dimensional Location of Object Contact Based on Mechanical Signals at the Whisker Base. Soft Robotics, 2017, 4, 88-102.

[19] R. Crowder, Toward robots that can sense texture by touch. Science, 2006, 312, 1478-1479.

[20] V. Lippiello, F. Ruggiero, B. Siciliano, L. Villani, Visual grasp planning for unknown objects using a multifingered robotic hand. IEEE/ASME Trans. Mechatronics, 2013, 18, 1050-1059.

[21] K. Weiss and H. Worn, "The working principle of resistive tactile sensor cells," IEEE International Conference Mechatronics and Automation, 1, 2005, pp. 471-476.

[22] Park, J., Lee, Y., Hong, J., Lee, Y., Ha, M., Jung, Y., Lim. H, Kim S. Y. and Ko, H. “Tactile-direction-sensitive and stretchable electronic skins based on human-skin-inspired interlocked microstructures” ACS nano, 8(12), 2014, pp. 12020-12029.

[23] Pan, L., Chortos, A., Yu, G., Wang, Y., Isaacson, S., Allen, R., Shi. Y, Dauskardt. R. and Bao, Z. “An ultra-sensitive resistive pressure sensor based on hollow-sphere microstructure induced elasticity in conducting polymer film”. Nature communications, 5(1),

2014 pp.1-8.

[24] Pyo, S., Lee, J., Kim, W., Jo, E., and Kim, J. “Multi-Layered, Hierarchical Fabric-Based Tactile Sensors with High Sensitivity and Linearity in Ultrawide Pressure Range” Advanced Functional Materials, 29(35), 1902484.

[25] Park, M., Park, Y. J., Chen, X., Park, Y. K., Kim, M. S., and Ahn, J. H. “MoS2-based tactile sensor for electronic skin applications”, Advanced Materials, 28(13), 2016, pp. 2556-2562.

[26] Mannsfeld, S. C., Tee, B. C., Stoltenberg, R. M., Chen, C. V. H., Barman, S., Muir, B. V., Sokolov. A. N., Reese. C, Bao. Z, “Highly sensitive flexible pressure sensors with microstructured rubber dielectric layers”, Nature materials, 9(10), 2010, pp. 859-864.

[27] H. K. Kim, S. Lee, and K. S. Yun, “Capacitive tactile sensor array for touch screen application”. Sensors and Actuators A: Physical, 165(1), 2011, pp. 2-7.

[28] T. Li, T., H. Luo, Q. Lin, X. Wang, Z. Xiong, H. Ding, Y. Gu, Z. Liu and T. Zhang, “Flexible capacitive tactile sensor based on micropatterned dielectric layer” Small, 12(36), 2016, pp. 5042-5048.

[29] Wan, S., Bi, H., Zhou, Y., Xie, X., Su, S., Yin, K., and Sun, L. “Graphene oxide as high-performance dielectric materials for capacitive pressure sensors”, Carbon, 114, 2017, pp. 209-216.

[30] Maiolino, P., Maggiali, M., Cannata, G., Metta, G., and Natale, L. “A flexible and robust large scale capacitive tactile system for robots”, IEEE Sensors Journal, 13(10), 2013, pp. 3910-3917.

[31] Li, C., Wu, P. M., Lee, S., Gorton, A., Schulz, M. J., and Ahn, C. H., “Flexible dome and bump shape piezoelectric tactile sensors using PVDF-TrFE copolymer”, Journal of Microelectromechanical Systems, 17(2), 2008, pp. 334-341.

[32] Ghosh, S. K., and Mandal, D. “Synergistically enhanced piezoelectric output in highly aligned 1D polymer nanofibers integrated all-fiber nanogenerator for wearable nano-tactile sensor”, Nano Energy, 53, 2018, pp. 245-257.

[33] Wang, X., Song, W. Z., You, M. H., Zhang, J., Yu, M., Fan, Z., Ramakrishna. S., and

Long, Y. Z. “Bionic single-electrode electronic skin unit based on piezoelectric nanogenerator”. ACS Nano, 12(8), 2018, pp. 8588-8596.

[34] Persano, L., Dagdeviren, C., Su, Y., Zhang, Y., Girardo, S., Pisignano, D., Huang. Y. and Rogers, J. A., “High performance piezoelectric devices based on aligned arrays of nanofibers of poly (vinylidenefluoride-co-trifluoroethylene)”, Nature communications, 4(1), 2013, pp. 1-10.

[35] Lee, M., Chen, C. Y., Wang, S., Cha, S. N., Park, Y. J., Kim, J. M., Chou. L-J and Wang, Z. L. “A hybrid piezoelectric structure for wearable nanogenerators”, Advanced Materials, 24(13), 2013, pp. 1759-1764.

[36] X. Wang, Y. Zhang, X. Zhang, Z. Huo, X. Li, M. Que, Z. Peng, H. Wang and C. Pan, “A highly stretchable transparent self-powered triboelectric tactile sensor with metallized nanofibers for wearable electronics”. Advanced Materials, 30(12), 2018, 1706738.

[37] Z. Wen, Y. Yang, N. Sun, G. Li, Y. Liu, C. Chen, J. Shi, L. Xie, H. Jiang, D. Bao, Q. Zhuo, and X. Sun, “A wrinkled PEDOT: PSS film based stretchable and transparent triboelectric nanogenerator for wearable energy harvesters and active motion sensors”, Advanced Functional Materials, 28(37), 2018, 1803684.

[38] X. Pu, M. Liu, X. Chen, J. Sun, C. Du, Y. Zhang, J. Zhai, W. Hu, and Z. L. Wang, Ultrastretchable, transparent triboelectric nanogenerator as electronic skin for biomechanical energy harvesting and tactile sensing. Science advances, 3(5), 2017, e1700015.

[39] X. Wang, H. Zhang, L. Dong, X. Han, W. Du, J. Zhai, C. Pan, and Z. L. Wang, Self-powered high-resolution and pressure-sensitive triboelectric sensor matrix for real-time tactile mapping. Advanced materials, 28(15), 2016, pp. 2896-2903.

[40] M. Ha, S. Lim, S. Cho, Y. Lee, S. Na, C. Baig, and & H. Ko, Skin-inspired hierarchical polymer architectures with gradient stiffness for spacer-free, ultrathin, and highly sensitive triboelectric sensors. ACS nano, 12(4), 2018, pp. 3964-3974.

[41] L. Persano, C. Dagdeviren, Y. Su, Y. Zhang, S. Girardo, D. Pisignano, Y. Huang, J. A. Rogers, High performance piezoelectric devices based on aligned arrays of nanofibers of poly (vinylidenefluoride-co-trifluoroethylene). Nat. Commun, 2013, 4, 1633.

[42] L. Pan, A. Chortos, G. Yu, Y. Wang, S. Isaacson, R. Allen, Y. Shi, R. Dauskardt, Z. Bao, An ultra-sensitive resistive pressure sensor based on hollow-sphere microstructure induced elasticity in conducting polymer film. Nat. Commun, 2014, 5.

[43] S. Gong, W. Schwalb, Y. Wang, Y. Chen, Y. Tang, J. Si, B. Shirinzadeh, W. Cheng, A wearable and highly sensitive pressure sensor with ultrathin gold nanowires. Nat. Commun, 2014, 5.

[44] J. Chun, K. Y. Lee, C. Y. Kang, M. W. Kim, S. W. Kim, J. M. Baik, Embossed Hollow Hemisphere-Based Piezoelectric Nanogenerator and Highly Responsive Pressure Sensor. Adv. Funct. Mater, 2014, 24, 2038-2043.

[45] C. Pang, G.-Y. Lee, T.-i. Kim, S. M. Kim, H. N. Kim, S.-H. Ahn, K.-Y. Suh, A flexible and highly sensitive strain-gauge sensor using reversible interlocking of nanofibres. Nat. Mater, 2012, 11, 795-801.

[46] W.-P. Shih, L.-C. Tsao, C.-W. Lee, M.-Y. Cheng, C. Chang, Y.-J. Yang, K.-C. Fan, Flexible temperature sensor array based on a graphite-polydimethylsiloxane composite. Sensors, 2010, 10, 3597-3610.

[47] S. Gupta, D. Shakthivel, L. Lorenzelli and R. Dahiya, IEEE. Sens. J. 2019, 19, 435.

[48] K. Kanao, S. Harada. Y. Yamamoto, W. Honda, T. Aire, S. Akita and K. Takei, RSC. Adv. 2015, 5, 30170.

[49] J. S. Lee, K-Y. Shin, O. J. Cheong, J. H. Kim and J. Jang, Sci. Rep, 2015, 7887.

[50] S. Harada, K. Kanao, Y. Yamamoto, T. Aire, S. Akita and K. Takei, ACS Nano, 2014, 8, 12851.

[51] C. Metzger, E. Fleisch, J. Meyer, M. Dansachmueller, I. Graz, M. Kaltenbrunner, C. Keplinger, R. Schwoediauer, and S. Bauer, “Flexible-foam-based capacitive sensor arrays for object detection at low cost”. Applied Physics Letters, 92(1), 2008, 013506

[52] D. J. Lipomi, M. Vosgueritchian, B. C.-K. Tee, S. L. Hellstrom, J. A. Lee, C. H. Fox, and Z. Bao, “Skin-like pressure and strain sensors based on transparent elastic films of carbon nanotubes”, Nature nanotechnology, 6(12), 2011, pp. 788-792.

[53] J. A. Dobrzynska and M. A. M. Gijs, “Polymer-based flexible capacitive sensor for

three-axial force measurements", Journal of Micromechanics and Microengineering, 23(1), 2012.

[54] J. A. Dobrzynska, and M. A. Gijs, "Flexible polyimide-based force sensor", Sensors and Actuators A: Physical, 173(1), 2012, pp. 127-135.

[55] R. Puers, "Capacitive sensors: When and how to use them", Sensors and Actuators A: Physical, 37, 1993, pp. 93-105.

[56] Ha, M., Lim, S., Park, J., Um, D. S., Lee, Y., Ko, H. "Bioinspired interlocked and hierarchical design of ZnO nanowire arrays for static and dynamic pressure-sensitive electronic skins", Advanced Functional Materials, 25(19), 2015, pp. 2841-2849.

[57] Selvan, N. T., Eshwaran, S. B., Das, A., Stöckelhuber, K. W., Wießner, S., Pötschke, P., Nando. G. B., Chervanyov. A. I., and Heinrich, G., "Piezoresistive natural rubber-multiwall carbon nanotube nanocomposite for sensor applications" Sensors and Actuators A: Physical, 239, 2016, pp. 102-113.

[58] Stassi, S., Cauda, V., Canavese, G., & Pirri, C. F. "Flexible tactile sensing based on piezoresistive composites: A review", Sensors, 14(3), 2014, pp. 5296-5332.

[59] Z. L. Wang, L. Lin, J. Chen, S. Niu, and Y. Zi, *Triboelectric nanogenerators*. Basel, Switzerland, Springer International Publishing, 2016.

[60] Kasap, S. O. "Principles of electronic materials and devices", McGraw-Hill, 2006.

[61] Tichý, J., Erhart, J., Kittinger, E., and Privratska, J. "Fundamentals of piezoelectric sensorics: mechanical, dielectric, and thermo dynamical properties of piezoelectric materials", Springer Science & Business Media, 2010.

II. BASIC CHARACTERISITICS AND THE METHOD FOR ENHANCING THE PRESSURE SENSITIVITY OF THE TACTILE SENSOR BASED ON ZnO NANOWIRE

2.1. Introduction

Recently, high-sensitive and self-powered pressure sensors have become a popular area of research in the bioelectrical engineering field because they can form one of the important base parts of an artificial tactile system, a wearable pulsimeter, or even a touch sensor[1-4]. In the research field of android robots, there have been many attempts to imitate the human sense of touch using pressure sensors. Resistive[5,6] and capacitive[7,8] pressure sensors have been in competition for tactile system applications, and recently, the capacitive type has been mainly used because of multi touch problems and sensitivity. However, an external constant power source is necessary for the operation of capacitive pressure sensors. As a result, a capacitive mechanism could have critical disadvantages when applied to future artificial tactile systems such as android robots or mobile devices. In the case of human skin, the principle of touch sensing is similar to the piezoelectric and pyroelectric effect, i.e., an electrical signal is generated when a pressure or a temperature is applied to the skin[9]. Therefore, power or energy consumption can be minimized for sensing. Because of this, self-powered pressure sensors using a piezoelectric material could provide an ideal solution for an artificial tactile system. A piezoelectric material can detect various external stimulation without external and constant power source. Although there are various piezoelectric materials, the materials for artificial skin are limited. Recently, the use of toxic materials in various electronics have been limited by policy or bill because of biocompatibility and/or environmental problems. For example, the EU classified Pb, Hg, Cd, Cr6+, PBB, and PBDE as the Restriction of Hazardous Substances (RoHS) and will prohibit the sale of electronics

containing these materials. Although Pb(Zr,Ti)O3 (PZT) are well known for having a high piezoelectric coefficient, the toxicity of Pb can be barrier for applying it to artificial skin. Then, the real artificial skin should be flexible whether the device is for humans or robotics. Flexible substrate of device should be stable from fabrication to using. Although the artificial skin is used at room temperature, the fabrication can be processed at high or low temperature. However, because flexible substrate cannot be generally enduring the high temperature process, the low temperature fabrication should be considered for other flexible electronics. Therefore, the high temperature process (~1100℃) cannot be applied to flexible electronics because the flexible substrate cannot generally withstand a high temperature fabrication process[10]. These days, many piezoelectric nanostructures have been researched for various applications[11-18]. Among the various nanomaterials, ZnO nanowire has been studied widely because the single crystal characteristic and nano-structural effect of a ZnO nanowire induces a better piezoelectric efficiency than a film or a bulk type of ZnO, as well as ZnO itself being nontoxic and bio-compatible. Additionally, ZnO nanowires are easily grown by a hydrothermal process below 90℃, meaning that the process can be applied to most flexible substrates, and the cost of the fabrication process is cheaper than that of vacuum deposition processes. In particular, low temperature processes such as hydrothermal[19] or sol-gel synthesis[20] processes should be considered for flexible electronics. However, the piezoelectric coefficient of ZnO nanowires is still smaller than that of other materials such as PZT[21] and BaTiO3[22]. The piezoelectric coefficients of these materials are ten to hundreds of times higher than that of ZnO nanowires. Despite the process temperature advantage of ZnO nanowires, the poor piezoelectric coefficient of ZnO nanowires limits their performance as a pressure sensor. Therefore, better device performance or other advantages were obtained by combining a ZnO nanostructure with PVDF-TrFE[16]. In other researches[20,22,23], to enhance

the piezoelectric efficiency, the longitudinal bending motion of nanowires has been studied for a strain sensor or a generator. Although this structure supplements the low piezoelectric coefficient of ZnO nanowire because the big deformation occurs, this has disadvantages for high resolution pressure sensor. Furthermore, the fabrication process of these researches is also one of the obstacles for the artificial skin. Especially, comparing to the fabrication process of other researches[22,23], we can assume that the fabrication time and cost of our device are much simpler. In ref. 22, they grew the BaTiO3 nanoparticle by hydrothermal process and mixed nanoparticle with a graphitic carbon. Then, this mixture is stirred and poured into a PDMS matrix for the final p-NC product. To fabricate device, the p-NC is spin casted onto substrates. Finally, the curing and poling process are following. And, in ref. 23, to prepare KNLN (alkaline niobite) particles, they dried the raw powder at the oven for more than 1 week. Then, in the middle of preparation process, the high temperature process at 750℃ and 1050℃ should be processed. On the other hand, the fabrication process of our device just consists of RF sputtering, simple photolithography, and low temperature hydrothermal. Although the fabrication process in various research cannot be quantitatively compared because the objective and use of research are different, it is clear that the fabrication for flexible artificial skin should be simpler.

In this study, we have studied the basic characteristics of ZnO nanowire and a structural solution for enhancing the sensitivity and voltage generation of a self-powered pressure sensor based on ZnO nanowires without a complicated fabrication process and the addition of other materials. As the structural solution, micro-level square pattern arrays of ZnO nanowires were employed for the sensor structure for high sensitivity. Generally, a hydrothermal growth mechanism of ZnO nanowires shows a high-density growth of ZnO nanowires similar to densely grown trees in a jungle. In this case, it is not easy to bend nanowires under

the influence of the surrounding nanowires except for those nanowires positioned at the edge of the cell structure. However, for the smaller micro-size cell array pattern design, the proportion of nanowires positioned on the edge of the square cell is greater. As a result, enhanced sensitivity and higher voltage generation were obtained with the other effect, that is, the growth direction of the nanowires. The simulation data of nanowire bending was well-matched to the experimental results which demonstrate the effect of the structural solution.

2.2. Basic characteristics of ZnO nanowire

ZnO nanowire is one of one-dimensional (1D) materials actively studied in nanotechnology.[24,25] Because ZnO has various properties such as n-type semiconductor material with wide band gap(~3.37eV), piezo and pyroelectricity, non-toxic and so on, wide range of applications in optics, optoelectronics, sensors, actuators, energy, biomedical sciences have developed by many researches.[26-33] Generally, ZnO has the wurtzite structure consisted of a hexagonal unit cell with lattice parameters a = 0.3296, and c = 0.52065 nm in Figure 2.1. A tetrahedral unit of ZnO consists of oxygen anions (O^{2-}) and zinc cations (Zn^{2+}) like Figure 2.2. The central charge asymmetry is specific characteristic of this structure and this asymmetry induces the piezoelectricity of ZnO.

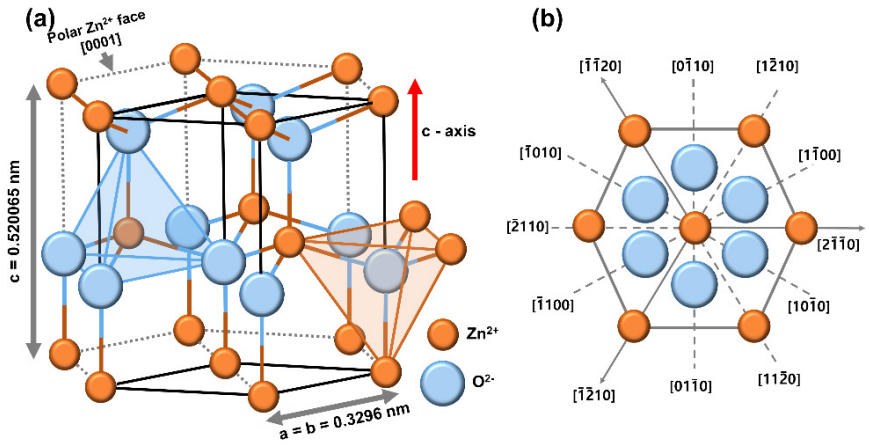

Figure 2.1. (a) The wurtzite structure of ZnO Crystal and (b) various types of facets from top view.

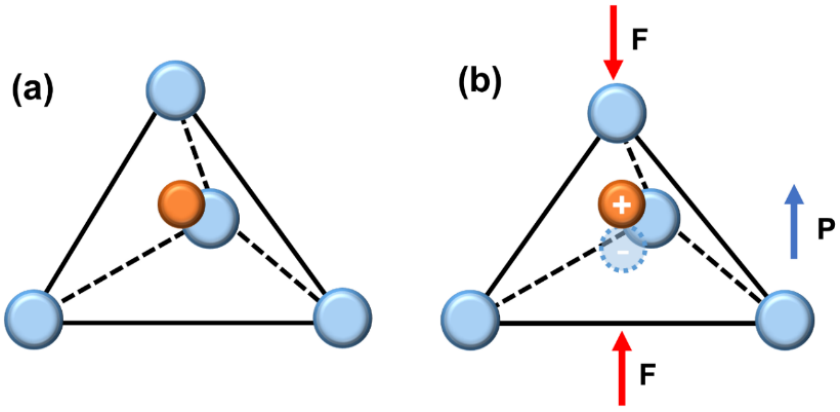

Figure 2.2. Schematics showing the piezoelectric effect in tetrahedral ZnO unit, (a) the case of (a) no external pressure and (b) the generation of the dipole by external force.

Property	*Unit*	
d_{31}	$10^{-12}CN^{-1}$	-5.43
d_{32}		-5.43
d_{33}		11.37
p_3	$10^{-5}Cm^{-2}K^{-1}$	
a_a	$10^{-6}K^{-1}$	4.36
a_c		2.49
s_{11}	$10^{-12}Pa^{-1}$	11.12
s_{12}		-4.56
c_{11}	$10^{10}N/m^2$	20.97
c_{12}		12.11

Table 2.1. Material coefficients of ZnO. Piezoelectric and Pyroelectric coefficient, thermal expansion coefficient, elastic constant and compliances.

One of attractive properties of ZnO nanowire is the piezoelectricity. This effect results from the atomic scale polarization. Figure 2.2 related to atom with a positive charge surrounded tetrahedrally by anions demonstrates the piezoelectricity of ZnO nanowire. If there is no external pressure, the center of the negative charges and tetrahedron are matched. However, if the external pressure is applied to the ZnO crystal, the tetrahedron structure is deformed and the center of the negative and positive charge do not coincide. As a result,

from the center of positive charge to negative charge, the electric dipole is generated. Therefore, the macroscopic dipole by the distortion of structure results in the piezoelectric effect along the ZnO nanowire. The electrical properties about the piezoelectricity of the ZnO nanowire is mainly demonstrated in following.

In this research, ZnO nanowires are grown by hydrothermal synthesis. For the hydrothermal synthesis, two kinds of zinc powder (zinc nitrate hexahydrate ($Zn(NO_3)_26H_2O$, from Sigma Aldrich Co) or zinc chloride ($ZnCl_2$, from Sigma Aldrich Co)) and hexamethylenetetramine (HMTA, $(CH_2)_6N_4$), from Sigma Aldrich Co) were used as main sources. Because $ZnCl_2$ show a bit of better characteristics through various test, $ZnCl_2$ is used for following experiments. First, to grow the ZnO nanowire hydrothermally, $ZnCl_2$ and HMTA were dissolved in de-ionized water. The ratio of $ZnCl_2$ and HMTA was 1:1. The molar concentration was 25mM. Thin ZnO film was formed by RF sputtering as a seed layer. This film-type seed layer allowed ZnO nanowires to grow on selected areas. The patterned seed film can be achieved easily using a photolithography process. Samples were immersed into the base solution at 90°C. To study the dimensional factors of nanowires depending on the growth process time, especially the ratio of diameter to length, 24h, 48h, and 72h were selected as process time. The growth results and crystallinity were observed by scanning electron microscopy (SEM), X-ray diffraction (XRD), and photoluminescence (PL).

Figure 2.3 (a) shows the top and cross-sectional SEM image of ZnO nanowire in accordance with the growth time. Based on the nanowire size of the SEM image, the average diameter and length are measured in Figure 2.3(b) and (c). The results indicate that the diameter and length are increased with longer growth time, simultaneously. Even if the length of ZnO nanowire is increased linearly, the diameter of nanowire is dramatically grown from 48h to 72h. As a result, the aspect ratio (length/diameter) of 48h-grown nanowire show the

highest value. Because the higher aspect ratio, the superior piezoelectric characteristics is generated,[34] the 48h-grown nanowire is used for following experiments. The piezoelectric voltage of the ZnO nanowire pressure sensor is measured in Figure 2.3(d). The result in Figure 2.3(e) also shows the higher piezoelectric characteristics of 48h-grwon nanowire with the high aspect ratio.

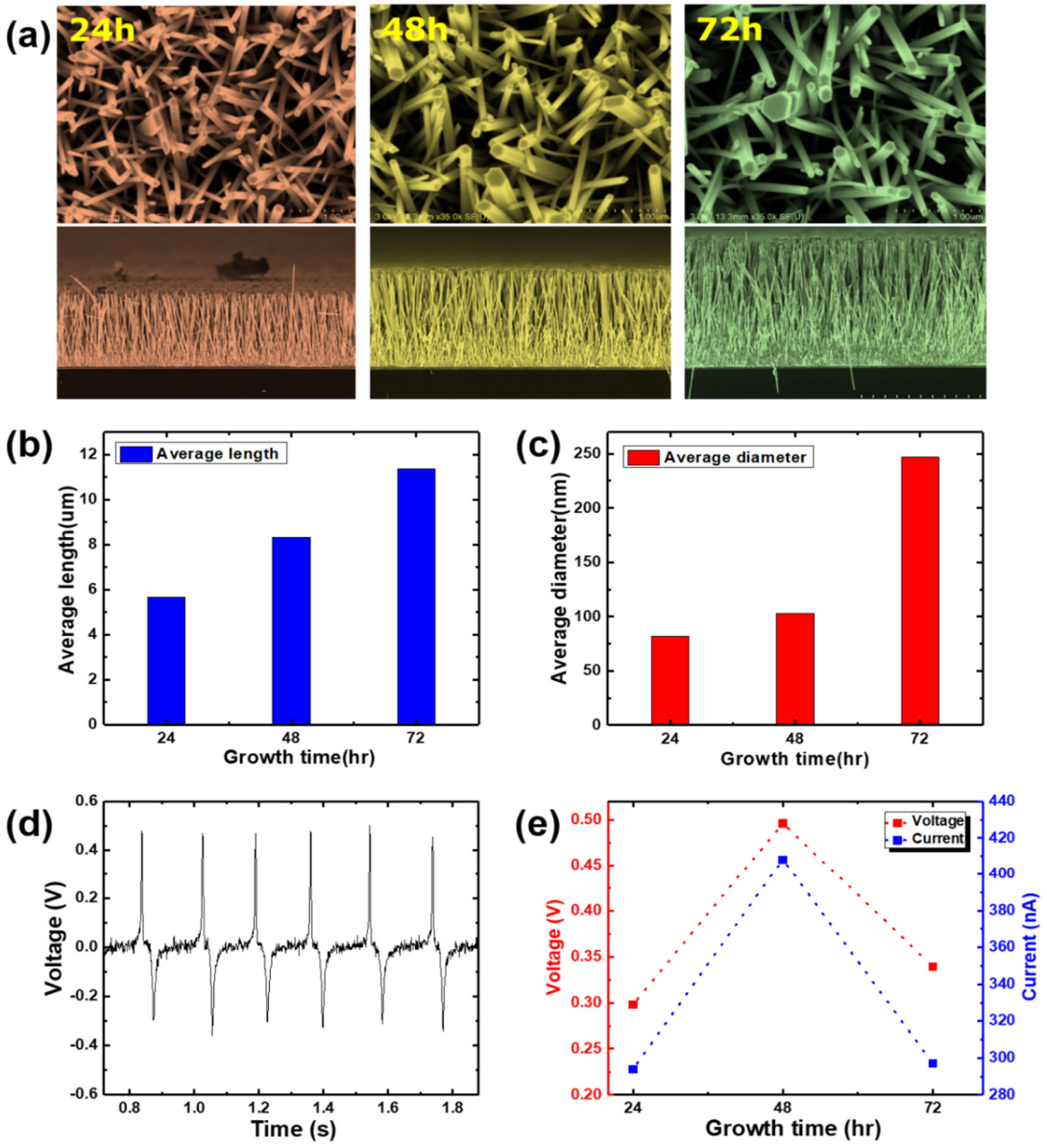

Figure 2.3. The characteristics of ZnO nanowire in accordance with the growth time (a) the top and cross view of SEM image of ZnO nanowire, (b) the average length and (c) diameter when the growth time is 24h, 48h, and 72h, respectively, (d) the piezoelectric signal of ZnO nanowire and (e) the piezoelectric voltage and current in accordance with growth time.

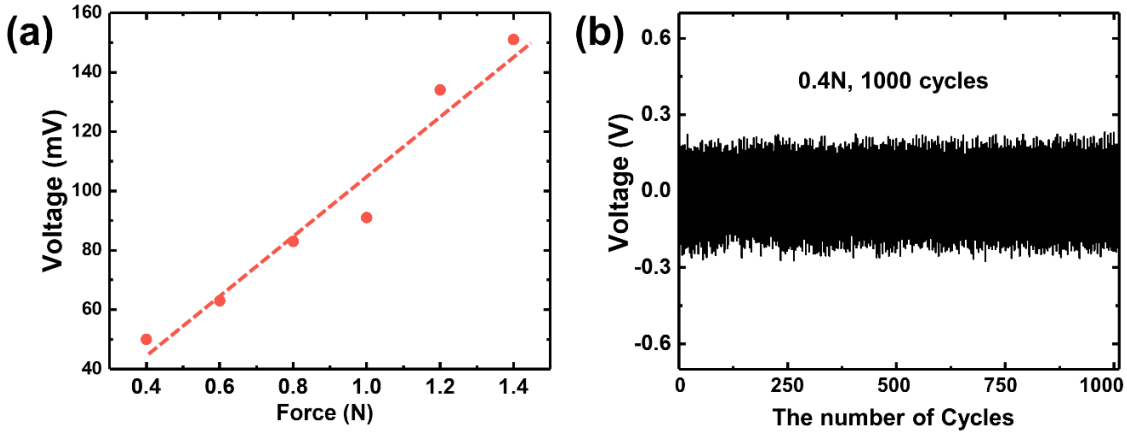

Figure 2.4. (a) The voltage sensitivity and (b) the stability during 1000 cycles of 48h grown-ZnO nanowire

The pressure sensitivity of the pressure sensor with ZnO nanowire is measured from 0.4N to 1.4N in Figure 2.4(a). The linear property means the possibility as the piezoelectric pressure sensor based on ZnO nanowire. Then, to confirm that the fabricated nanowire consists of Zn and O atom, Energy Dispersive Spectrometry (EDS) measurement is conducted to single ZnO nanowire in Figure 2.5. These SEM images show the mapped Zinc and Oxygen ion along the nanowire.

Another property of ZnO is inherent n-type semiconductor. This n-type characteristic of ZnO from native defects by Zn interstitials and O vacancies results in native conductivity. In addition, as-grown ZnO nanowires have some defects such as oxygen vacancies, zinc interstitials or other impurities.[35-39] As a result, because there are free carriers by various impurities, the n-type characteristics is inherent in as-grown ZnO nanowire. In this thesis, the nanowire is grown by using two kinds of chemicals (Zinc nitrate hexahydrate, Zinc chloride). So, the defect level of two cases in the nanowire is proved by photoluminescence (PL) in Figure 2.6 (a) and (b). Even if main peak of ZnO nanowire is about 380 nm because the band gap is 3.37eV, the broad peak is observed from 500 nm to 800nm. This emission results from various defects of as-grown nanowire.

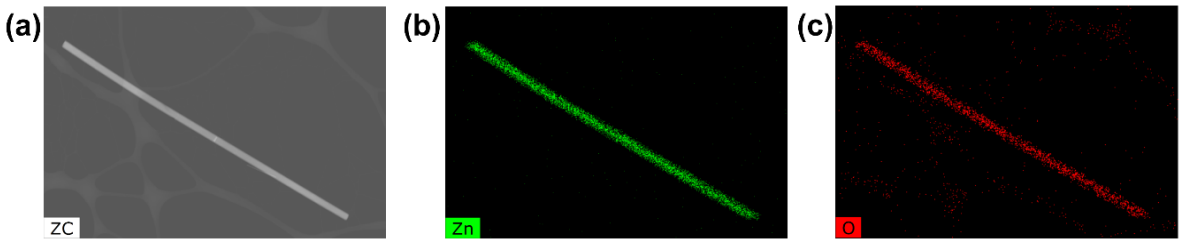

Figure 2.5. High resolution Energy Dispersive Spectrometry (EDS) image of the ZnO nanowires. (a) SEM image of (a) single ZnO nanowire, SEM image of ZnO nanowire with (b) Zn and (b) O ion mapped data. The white scale bar is 1um.

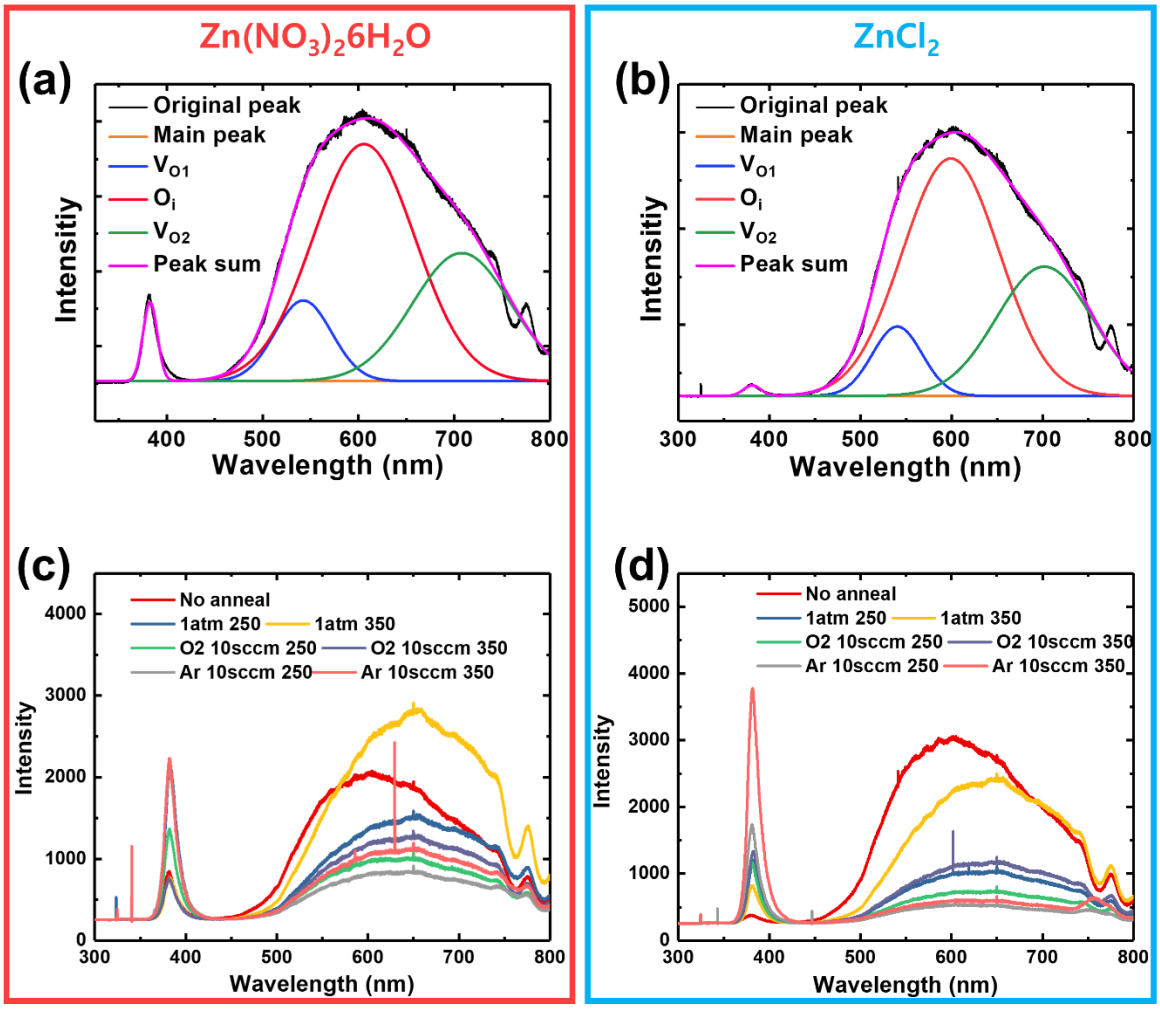

Figure 2.6. The Photoluminescence (PL) intensity of ZnO nanowire and the defects in accordance with (a), (b) the kinds of Zn chemical and (c) and (d) various annealing condition.

Currently, native n-type semiconductor characteristic of ZnO has limited the development of the device based on p-type ZnO nanowire. Specially, when the piezoelectric application is developed, this conductivity results in the decrease of piezoelectric efficiency because the free carriers move to the direction to screen the piezoelectric polarization. Therefore, to remove the free carriers of ZnO and enhance the piezoelectric effect, the annealing and other methods have been carried out by many researches.[40-43] In this study, the annealing with high temperature and certain gas is conducted in Figure 2.6(c) and (d). The kinds of gases are Ar, O, and atmosphere and high temperature of 250℃ and 350℃ are used for annealing. Even if the annealing at 250℃ in atmosphere is a bit of better than the case of 350℃, the other gases like Argon and Oxygen are much more effective than atmosphere environment. When comparing argon with oxygen, the annealing using argon gas is more successful than that using oxygen if the annealing temperature is same. We assume that oxygen gas for compensating the oxygen vacancies is less efficient if the main defect is oxygen interstitial like Figure 2.6(a) and (b). In addition, if the gas condition is same, 250 ℃ is a little better than 350 ℃. This means that high energy by high temperature over 350 ℃ can reduce existing defects while simultaneously causing other defects.

After the annealing process, the photoluminescence (PL) spectrum of the as-grown nanowire is compared with annealed ZnO nanowire in Figure 2.7(a). The PL spectrum of as-grown ZnO nanowires usually exhibits two strong-luminescence bands: a band edge emission (UV band) and a visible broad band. The UV band is attributed to the direct recombination of excitons through an exciton-exciton collision process and the visible broad band originates from a variety of deep level defects, such as vacancies of oxygen, zinc interstitials, or other impurities. The PL spectrum of as-grown ZnO nanowire shows the broad peak in visible light region and it means that there are some defects, whereas, the PL

spectrum of annealed ZnO nanowire usually exhibits sharp band edge emission (UV band) due to the reduction of defects by annealing process. Then, Figure 2.7(b) shows the relative atomic percent of Zn and O in as-grown and annealed nanowire by high resolution EDS analysis. The results mean that electrons produced by the defects like oxygen vacancies is a major carrier. Furthermore, as the other test to confirm the free carrier in ZnO nanowire, the test is carried out to confirm the seebeck effect generated by the movement of free carrier when the high temperature is applied to the nanowire.

The piezo-Seebeck effect using as-grown and annealed ZnO nanowire is measured as shown in Figure 2.7(c). The sensor structure was pressed by heated object. As shown in the result, the Seebeck current was obtained between piezoelectric sharp signals due to thermal energy in as-grown ZnO nanowire (The upper graph of Figure 2.7(c)). However, the dc-like Seebeck current is not observed for the annealed ZnO nanowire (The lower graph of Figure 2.7(c)). Therefore, we can detect the part of thermal energy separately from press state, although the design employing a single material is selected for simplifying device structure to generate artificial tactile feeling in contrast with the piezoelectric-pyroelectric combination. As a result, the Seebeck voltage of ZnO nanowire was measured by applying the heat source to device from 313K to 393K (Figure 2.7(d)). From this result, we can calculate the Seebeck coefficient S of ZnO nanowire by using following equation.

$$\boldsymbol{S} = -\frac{\boldsymbol{\Delta V}}{\boldsymbol{\Delta T}} \tag{2.1}$$

ΔV is the voltage difference and ΔT is the temperature difference between the hot and cold sides of ZnO nanowire. The calculated Seebeck coefficient is -64μV/K (Figure 2.7(d)). Since the Seebeck effect of ZnO nanowire comes from the electron movement by heat source, equation (2.1) should include the negative sign. Therefore, Seebeck current $I_{seebeck}$ can be expressed by equation (2.2).

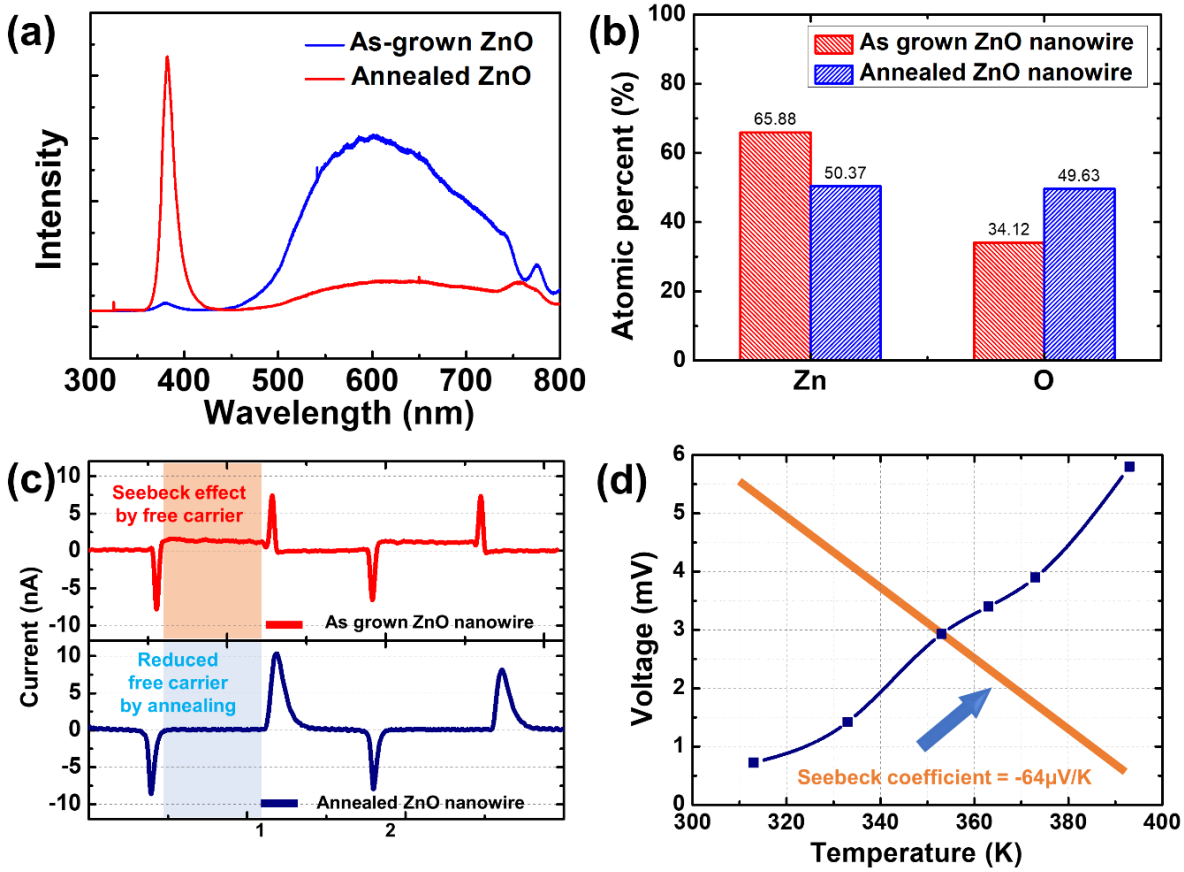

Figure 2.7. ZnO characteristics by free carrier in ZnO nanowire, (a) photoluminescence (PL) and (b) atomic percent of as-grown and annealed ZnO nanowire, (c) the current generation by free carrier and (d) the seebeck coefficient of ZnO nanowire.

$$I_{Seebeck} = \frac{-S\Delta T}{R_L} \tag{2.2}$$

R_L is the resistance of external load. The detail theoretical basis of Seebeck effect is in our previous result. Similar result of Seebeck effect of ZnO nanowire system was reported in energy harvesting field.[31] In addition, to verify the details more, seebeck potential simulation was performed. The simulation is carried out by heating the top or bottom side of the ZnO nanowire to confirm the movement of free carriers. When the temperature increases on the top electrode of the sensor, the free carriers go down toward the bottom electrode and the Seebeck potential of top electrode (the third image of Figure 2.8(a)) is higher than that of bottom electrode. On the contrary, when the heat is applied to the bottom electrode, the

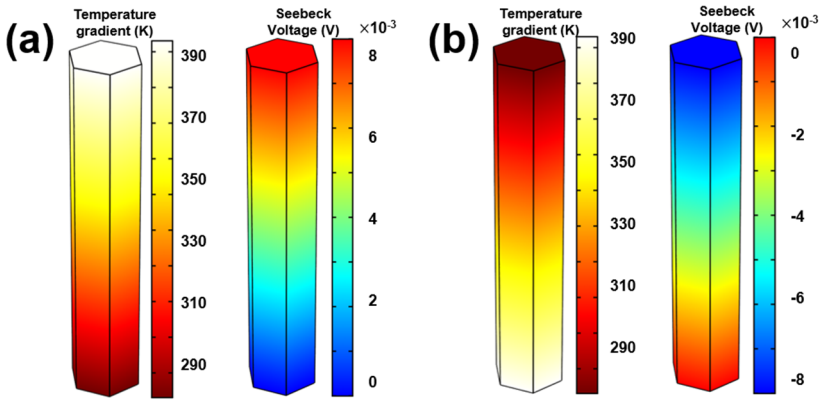

Figure 2.8. Simulation result of seebeck effect of ZnO nanowire when the temperature is applied to the (a) top or (b) bottom side.

free carriers move opposite to the heat source and the Seebeck potential is generated from the bottom to the top electrode like the third image of Figure 2.8(b). This implies that the seebeck voltage can be produced by the accumulation of free carrier movement at high temperature condition.

2.3. Device Fabrication

Figure 2.9 shows the schematics of the sensor unit using the pattern structure for the artificial tactile system. SiO_2 /Si or plastic substrate was used as a base substrate. It was cleaned with acetone and isopropanol alcohol (IPA) by ultrasonicating for 5min. Then, O_2 plasma washing was done to remove the polymer residue and to enhance the adhesion of photoresist, as shown in Figure 2.9(a). RF sputtering and photolithography were used to deposit the bottom electrode metals, as shown in Figure 2.9(b).

In this study, we used a Cr (10nm) and Au (100nm) layer as the bottom electrode. The 10 nm Cr layer played a role in the adhesion layer by reducing the lattice mismatch between the substrate and the electrode material. The Au layer was used to form the Schottky barrier between the ZnO nanowires and metal layer with an electrode function. Due to the semiconductive characteristic of the ZnO nanowires, at least one side of the Schottky barrier

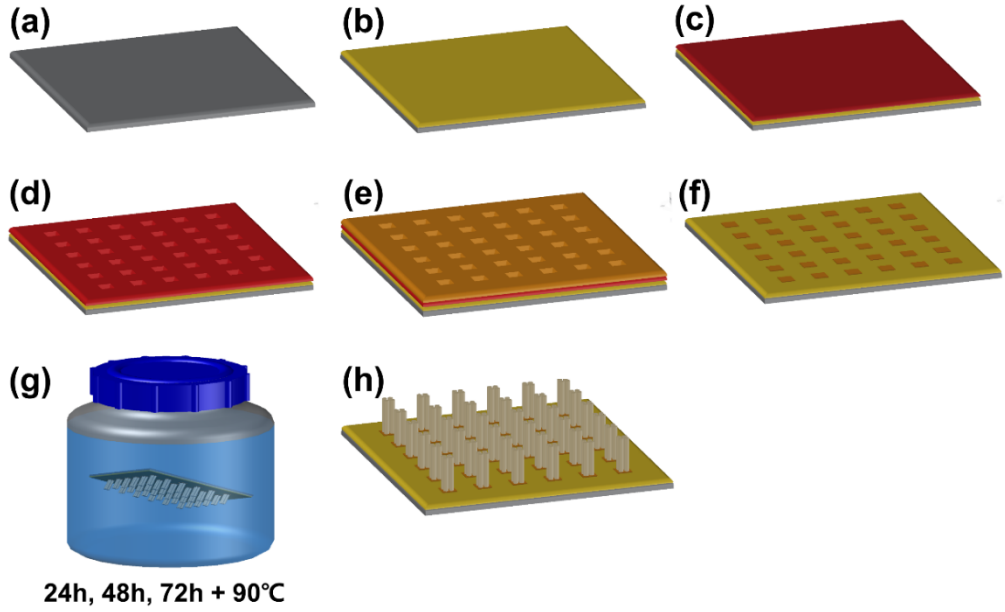

Figure 2.9. Schematic of an artificial tactile system using a pattern structure, (a) SiO_2/Si substrate, (b) Cr/Au thin film for bottom electrode deposited by RF sputtering, (c) spin coating of positive photoresists (GXR-601), (d) photolithography and development for square pattern, (e) ZnO seed layer deposited by RF sputtering, (f) after lift-off of ZnO seed layer, (g) hydrothermal growth of ZnO nanowire, (e) grown ZnO nanowire.

is favored to obtain charge accumulation between the nanowires and the metal electrode and to generate good electrical power and signal.[44] In Figure 2.9(c) and (d), to make the cell array structure of the sensor, photolithography and RF sputtering were performed. In this research, AZ GXR-601 was spin-coated at 3000rpm, and the soft bake was performed for 2min at 100°C. Then, hydrothermal synthesis was applied to grow the ZnO nanowires at 90°C for 24h, 48h, and 72h (Figure 2.9(d)). After the growth, the sample was taken out of the sealed bottle and the ZnO residue of the sample back plate was cleaned with acetone, IPA, and de-ionized water (Figure 2.9(e)). The ITO-coated substrate was placed on the cell array of nanowires as the top electrode in order to measure the piezoelectric signal of the ZnO nanowires. After that, two substrates were assembled with soft polymer glue. Finally, the lead line was connected to the bottom metal contact line in order to measure the electro-chemical characteristics as shown in Figure 2.9(f).

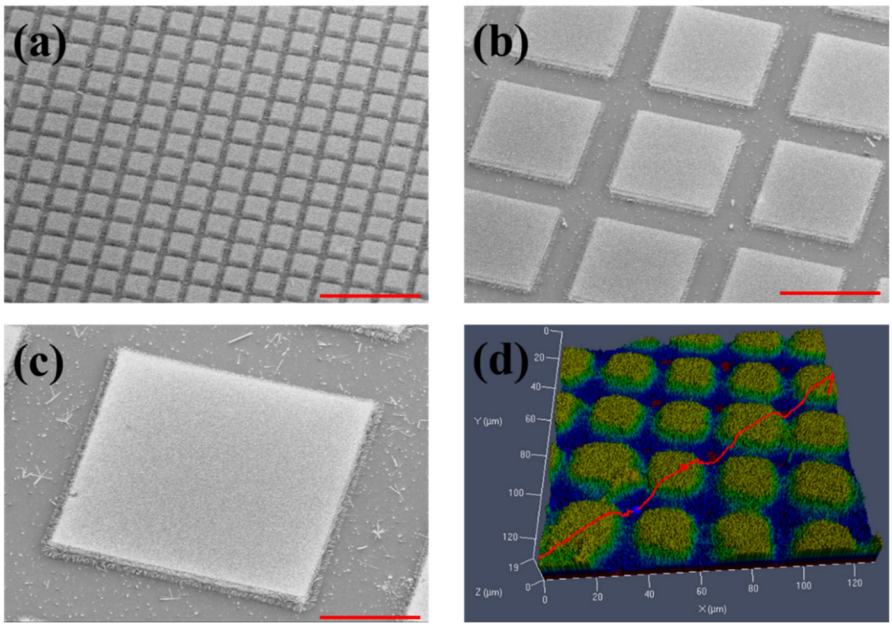

Figure 2.10. The growth result of ZnO nanowire with square pattern, the SEM image of ZnO Nanowire with a pattern of (a) 20um, (b) 100um, (c) 250um, and (d) the confocal microscopy image of 20um pattern. The red scale bar is 100um.

2.4. Morphological and electrical characteristics

Figure 2.10 shows the morphological characteristics and quality of the ZnO nanowires. Figure 2.10(a) to (c) show the SEM images of the ZnO nanowires depending on the pattern size of 20um × 20um, 100um × 100um, and 250um × 250um, respectively. The percentage of area on which the nanowires were grown was kept constant at a value of 50% for all pattern cases. Figure 2.10(d) shows a confocal microscopy image showing the pattern structure of the ZnO nanowire array. All pattern samples had a high density of ZnO nanowires on the center of the square-shaped cell structure. The density value is $7.5 \times 10^8/cm^2$, and this value is inferred from the top view of the SEM image. Whether the samples are patterned or not, the density of the nanowires at the center of cell is almost the same. Due to the nanowires on the edge grown at an angle, not vertically, the edge of the pattern is not sharp, and a different color which corresponds to the length of nanowire is shown in Figure 2.10(d). The details of this are discussed later.

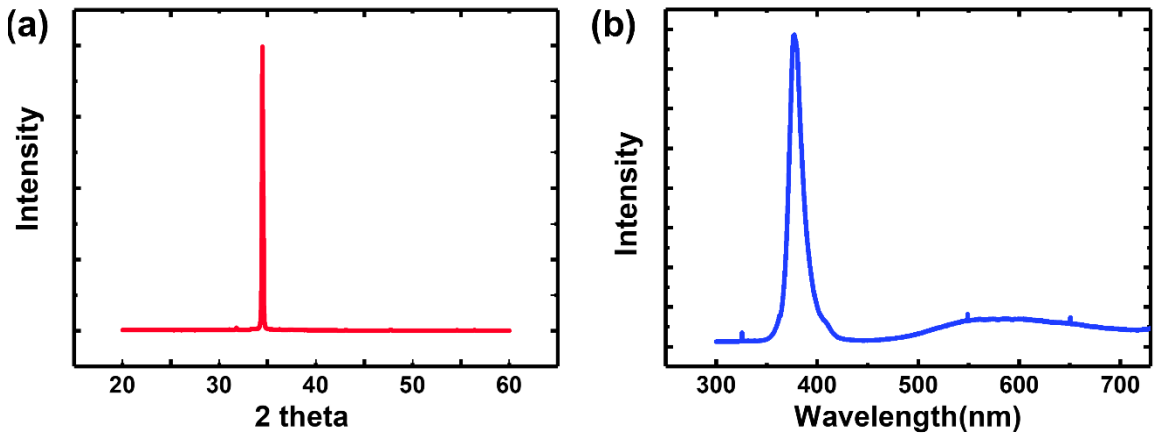

Figure 2.11. Material characteristics of ZnO nanowire, (a) X-ray diffraction analysis and (f) photoluminescence of ZnO Nanowire.

In Figure 2.11(a), the XRD pattern of the ZnO nanowires shows the quality and alignment of the nanowire array. Since most of the ZnO nanowires have a single crystal form of wurtzite structure, and the growth direction of the c-axis is vertically aligned to the substrate, one strong diffraction peak at (0002) is detected.[45] Therefore, quite good crystalline materials are grown by the hydrothermal method, even though the process temperature is at just 90°C. Other small peaks come from the substrate materials, Au and Si. To verify further details of the material's own characteristics, PL property is observed in Figure 2.11(b). This result shows the highest UV emission at 385nm, which corresponds with free-exciton emission energy of ZnO. The small broad emission from 550nm to 700nm is due to a deep-trap level, mainly due to oxygen vacancies and impurities in ZnO or surface defects.[46] Therefore, although the ZnO nanowires are in a good crystalline state, they have some defects, but their concentration is not high. Some defects can be removed by thermal annealing. However, for artificial tactile sensors, many low-melting temperature materials are needed as base materials, such as plastic substrates and polymers, and because of that we did not apply thermal annealing in this experiment.

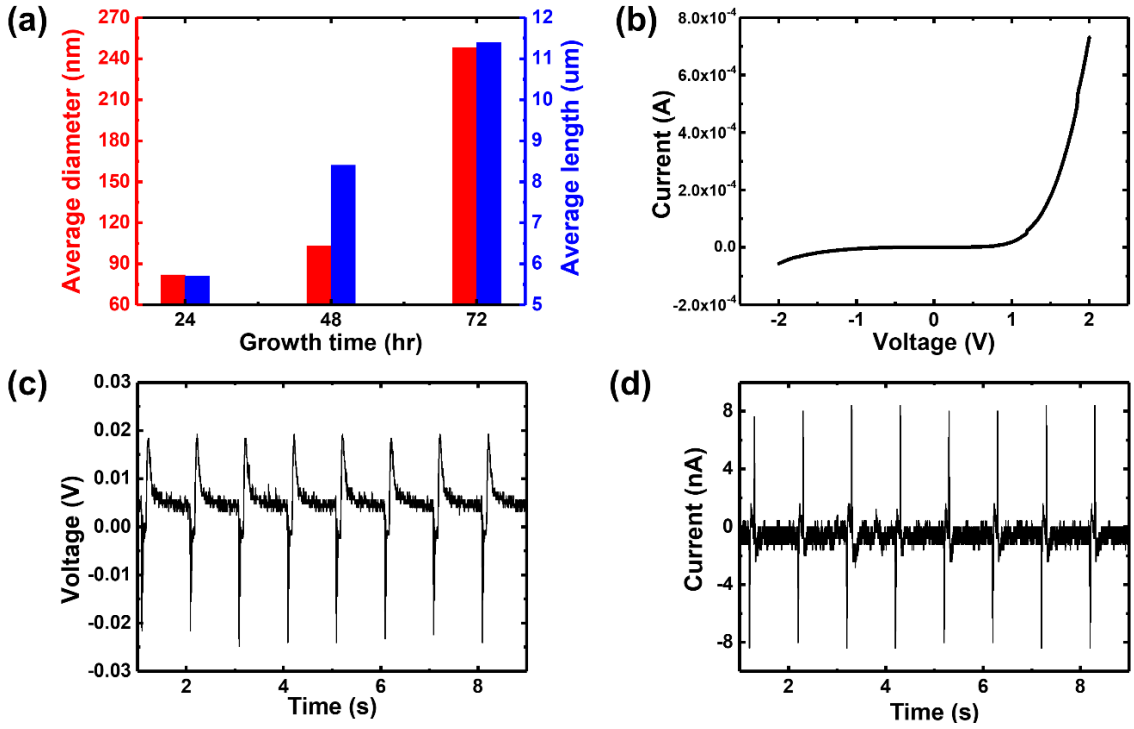

Figure 2.12. The dimension of the ZnO nanowires depending on growth time and electrical characteristics, (a) the average diameter and length, (b) I-V characteristics of Schottky barrier, (c) piezoelectric voltage and (d) piezoelectric current.

As shown in Figure 2.12(a), the average diameter and the average length of the nanowires change from 82nm to 248nm and from 5.7um to 11.4um with increasing growth time, respectively. The length generally increases linearly with the growth time, but the diameter increases rapidly between 48h and 72h. As a result, the aspect ratio between the length and the diameter of the nanowires is at its highest level when the growth time is 48hr. The aspect ratio of the ZnO nanowires affects piezoelectric polarization and generated voltage level. Generally, a high-aspect nanowire can generate higher electrical voltage when applying the same pressure.[47] Therefore, we chose mainly 48hr as the growth condition to study the cell patterning effect of the piezoelectric pressure sensor. As mentioned previously, due to the semiconductive characteristic of the ZnO nanowires, a Schottky barrier-which is one of the easier solutions—is required to obtain high power generation or high sensitivity between voltage signals and pressure.

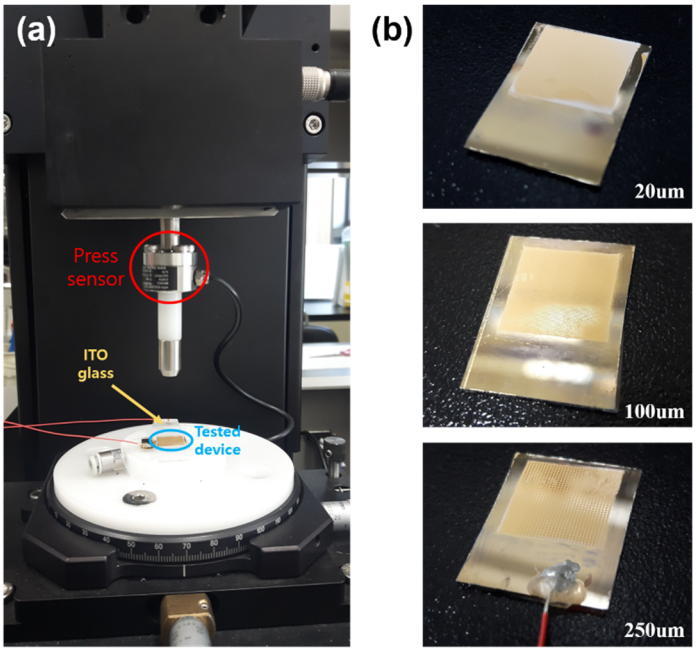

Figure 2.13. (a) The pressure measurement system and (b) the tested samples corresponding with pattern size.

To form a Schottky barrier with ZnO nanowires, which exhibits n-type semiconductor behavior due mainly to oxygen vacancies, Au thin film was employed as a bottom electrode. Since electron affinity of ZnO nanowires is about 4.5eV and the work function of Au is about 5.2eV, the Schottky barrier height between the ZnO nanowires and Au is 0.7eV.[48] To confirm the Schottky barrier formation, the I-V characteristic is measured and the rectifying characteristic is observed in Figure 2.12(b). The result shows a good formation of the Schottky barrier between the ZnO nanowires and the Au electrode. We then measured the practical piezoelectric voltage and current, as shown in Figure 2.12(c) and (d). The level is about 23mV and 8nA when the pressure is 10kPa. Additionally, the working performance as a pressure sensor based on the piezoelectric effect is very stable. To measure the piezoelectric signal, we set the pressure measurement system shown in Figure 2.13(a). The metal tip descends, and pressure from 4 to 14kPa is applied to the samples. The generated piezoelectric signal is transferred to the oscilloscope connected to the device.

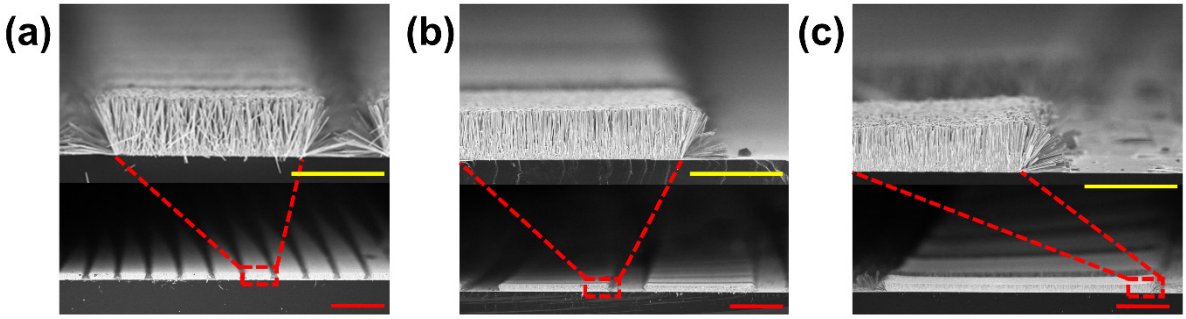

Figure 2.14. SEM images of nanowire with pattern size, (a) 20um, (b) 100um and (c) 250um cell structure. The yellow scale bar is 10um and red scale bar is 50um.

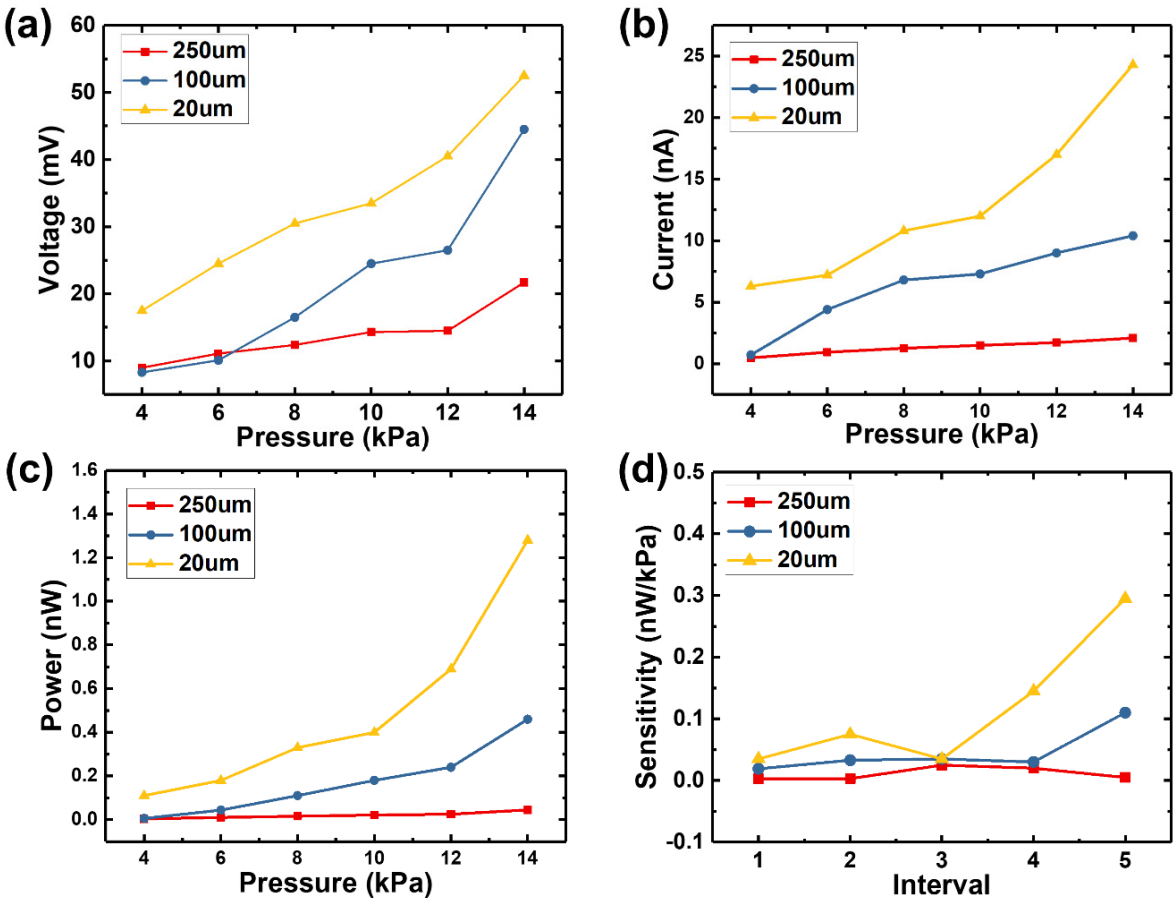

Figure 2.15. The pressure sensitivity of the pressure sensor using the ZnO nanowires depend on the pattern size, (a) the piezoelectric voltage, (b) piezoelectric current and (c) power generation with various cells and increasing pressure from 4 kPa to 14 kPa, (d) the sensitivity depending on the pressure measurement interval.

2.5. Pattern structure for enhanced pressure sensitivity

For seed-assisted growth of the ZnO nanowires, the nanowires grow without adequate empty space. As a result, it is not easy to bend nanowires under the influence of the surrounding nanowires by low pressure. Therefore, the densely grown nanowires induced a low sensitivity to pressure due to their low power or low signal generation efficiency. In the case of the nonpatterned samples, low pressure levels (< 14kPa) cannot be detected. To enhance the pressure sensitivity and the power generation, a density control of nanowires is required as one of the solutions since the low density of nanowires can guarantee a proper space for bending. Unfortunately, the population control of ZnO nanowires is not easy. Even if it is possible, it makes the problem of material quality or material dimension such as the aspect ratio between length and diameter. The change of unit cell structure can be considered as one good solution. In this study, by dividing the one-body cell structure into many small cell arrays, the density of nanowires can be decreased, and free space between pattern structures become available to more easily bend nanowires. Figure 2.14(a) to (c) show the SEM images of the cross section of nanowires with pattern size. The ZnO nanowires were grown only on the patterned seed area. The total area of the seed layer was reduced to 50% by the small pattern design, but the total size of the sensor was still kept to the same size of a nonpatterned design. It means that the number of nanowires per total area is almost reduced to 50%. Therefore, the pressure level loaded per nanowire is much higher than that of a one-body design. Another structural point is that of the obliquely grown nanowires at the edge region. The details of this are mentioned in following section. As shown in in Figure 2.15(a) to (d), the smaller cell design shows a better pressure sensitivity and power generation efficiency. With increasing pressure, all the cell structures have a higher piezoelectric voltage, since the deformation of the ZnO nanowires is increased. For the 20um cell design, all the

induced voltage levels are higher than 10mV, which is enough to be measured by a general sensing circuit. Although the 250um × 250um cell pattern structure shows the lowest power generation efficiency, the level is still higher than that of the one-body structure due to the decrease in population of the ZnO nanowires. From 4kPa to 12kPa, the generation voltage sensitivity of the 20um, 100um, and 250um cell designs are 3.5mV/kPa, 3.6mV/kPa, and 1.27mV/kPa, respectively. Although the sensitivity of 20um and 100um is similar, the generated piezoelectric voltage of 20um is higher. It means that the sensing limit of the 20um design for low pressure (<14kPa) is better. In addition, the generated current level of 20um is 2-11 times higher than that of other patterns depending on pressure level. Considering power generation, the cell pattern effect is much clearer. The average power sensitivity of 20um is 0.12nW/kPa, as shown in Figure 2.15(c), and this value is also much higher than in other cases. The 20um pattern is not the optimized condition. The smaller cases can be better, but the edge nanowires of smaller cells can overlap with each other because the length of the nanowires can be larger than the space between the cells. Therefore, the edge effect can decrease. In addition, it is not easy to obtain a good yield with the lithography process as well as the growth of nanowires without the precise control of processes for much smaller patterns.

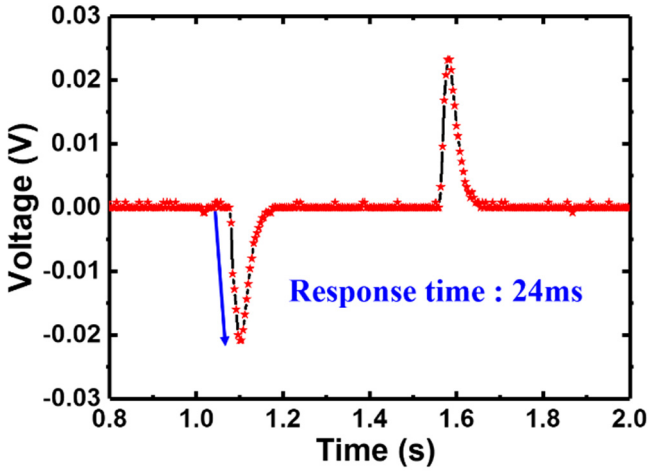

Figure 2.16. The response time of the ZnO nanowire pressure sensor

In Table 2.2, we compared the pressure sensitivity of other research[44,49-53] with our results. In ref. 31, the device structure is noticeable because the enhanced sensitivity is achieved by special structure like a hierarchical design. This means that the structural solution can enhance the sensitivity of pressure sensor. Even if there is the case of randomly calculated sensitivity to unify the unit of sensitivity and there will be more superior results in other researches, our results are also fully comparable with other results. Then, Figure 2.16 shows the response time of the piezoelectric voltage of the ZnO nanowires. This value is faster than that of the pressure sensors using other sensing mechanisms in other researches[8,14,54]. The response time is also one of the most important factors in designing an artificial tactile sensor. In this study, the measured piezoelectric voltage error was below 5%, and it showed reliable results under 1000 tests. The durability and reproducibility of piezoelectric devices using ZnO nanowires have already been proven in various studies[14,15,44].

	Sensitivity	**Note**
This research	3.6mV/kPa	ZnO nanowire
Xu et al. [24]	0.08mV/kPa	ZnO nanowire
Deng et al. [29]	0.403mV/kPa (403mV/MPa)	ZnO nanorod
Nabar et al. [30]	0.053mV/kPa	ZnO nanorod
Ha et al. [31]	3.6mV/kPa	ZnO nanowire (hierarchical design)
Sharma et al. [32]	0.5mV/kPa	PVDF-TrFE (higher piezocoefficient)
Choi et al. [33]	0.031mV/kPa	PZT thin film (highest piezocoefficient)

Table 2.2. The sensitivity comparison of various sensors using piezoelectric materials

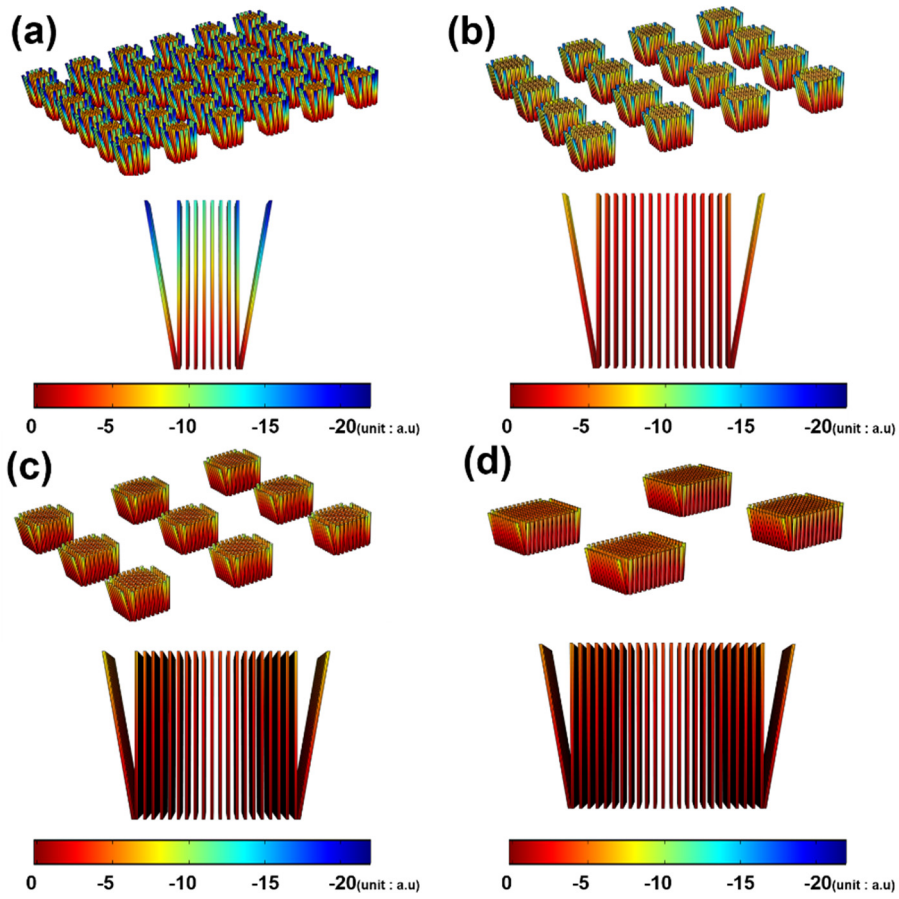

Figure 2.17. The simulation results depending on the pattern structure, (a) 25um, (b) 50um, (c) 62.5um and (d) 75um pattern are applied in the COMSOL simulation. The nanowire diameter is 1um and the length is 10um. The angle of the slanted nanowire is 10°. The pressure is 10 kPa in all cases.

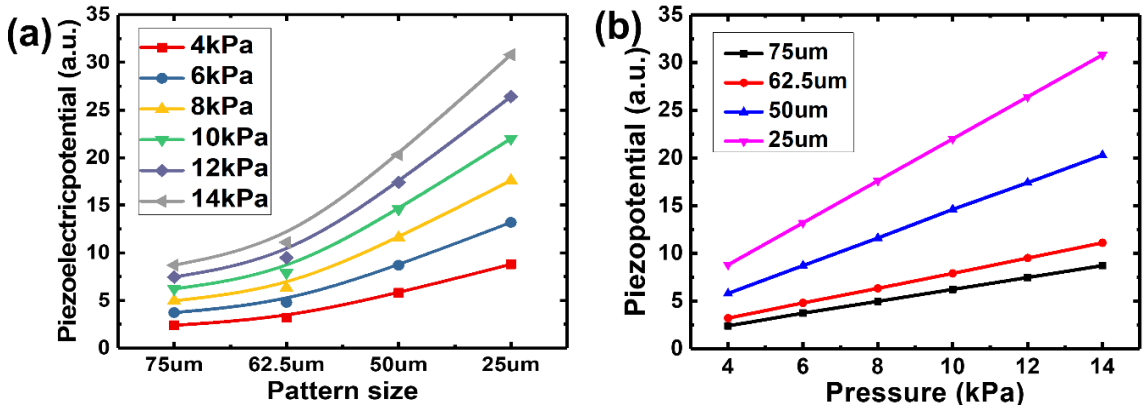

Figure 2.18. The maximum piezoelectric potential in accordance with pattern size or pressure, (a) the maximum piezoelectric potential with pattern size when the pressure is constant, (b) the maximum piezoelectric potential with pressure when the pattern size constant in the simulation result.

2.6. The simulation result of piezoelectric effect for pattern structure

To verify the effect of patterned cell design more clearly, the displacement and induced piezoelectric voltage were simulated with different cell structures at various pressure levels. COMSOL simulation was applied to prove the advantage of the micro pattern structure, and then the simulation was focused more on smaller pattern sizes from 25um to 75um. The spacing between patterns was modified to keep a ratio of real ZnO cell structures. These real structural factors such as the area ratio and the angle of grown nanowires were considered in the simulation models. The obliquely grown nanowires are expressed in Figure 2.17 and Figure 2.19. There are two effects resulting in voltage increase in the pattern structure. One is the density control. If there is no square pattern structure, the nanowires are grown on an overall substrate. In this case, since the density of the nanowires is too high ($7.5\times10^8/cm^2$), the nanowires cannot be bent easily at low pressure, as mentioned previously. In fact, when low pressure from 4kPa to 14kPa was applied to the nonpatterned structure, the piezoelectric signal was hardly observed. However, if the seed layer was patterned by the lithography process, the nanowires grew on the seed layer. Therefore, the density of grown nanowires can be controlled depending on the area of the seed layer. In this research, the total area of the patterned seed layer was also kept to 50% compared to the nonpatterned case. The number of nanowires pressed by the top electrode is also reduced to 50% by simple calculation. The voltage increase by the density control can be expressed by the following equation:

$$\mathrm{P} = \ F/S = F/(NS_n) \tag{2.3}$$

P is the pressure applied to the total nanowires, and F is the force applied to the top electrode. S is the pressed area. N is the real number of pressed nanowires and S_n is the tip area of the nanowires. As a result, even when the same force is applied to the device, the

pressure per nanowire for the patterned cell design is double because the pressure is the force per area. The center nanowires of the square pattern are mainly affected by this density control. Therefore, the piezoelectric potential of the nanowires of the smaller pattern can be increased compared to the nanowires of the nonpatterned or larger-patterned device. This effect is confirmed by the simulation in Figure 2.17. Figure 2.17(a) to (d) show the piezoelectric potential of the nanowire model with pattern size. This result indicates that the piezoelectric potential of the 25um pattern in the center region is higher than that of the other cases in Figure 2.17(a) to (d). Due to the density control, the smaller pattern helped the nanowires generate a high piezoelectric potential, as shown in Figure 2.18(a) and (b).

The simulation model also indicates that the edge nanowires generated higher piezoelectric potential than that of the center nanowires, since the edge nanowires were additionally affected by not only the density control but also another factor. This is the buckling effect. The following equation explains this phenomenon:

$$\sigma_{cr} = \{P_{cr}/(\overline{N}A)\} \cdot F(b) = \{\pi^2 E cos\theta/(L_e/r)^2\} \cdot F(b) \quad (2.4)$$

where, σ_{cr} is critical stress, P_{cr} is $P\cos\theta$ and critical pressure of the column. P is vertical pressure, and θ is the angle of the obliquely grown nanowires. $\overline{N}$ is the number of nanowires per unit area, A is the tip area of the nanowires, and *F(b)* is a correction function related to the surrounding environment. E is the elastic modulus of the column and L_e/r is the slenderness ratio, which is a similar concept to the aspect ratio of the ZnO nanowires. Equation (2) indicates the behavior of an ideal column under pressure. When the critical stress is applied to the column, buckling occurs in the nanowires.[55] As a result, the piezoelectric polarization can be increased due to the intensive and sudden deformation from the buckling effect along the nanowires. This effect is controlled by some factors. First, this is the effect of density control. Because of the empty space between patterns, the density of

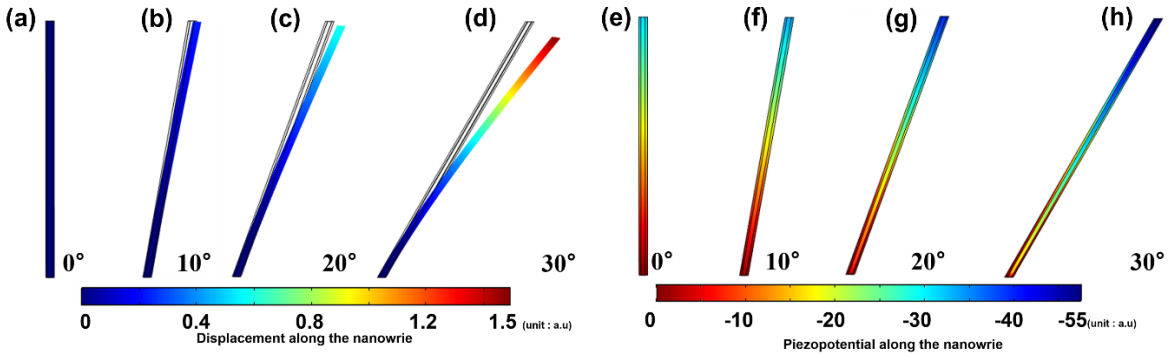

Figure 2.19. The displacement of nanowire depending on the angle (a) 0°, (b) 10°, (c) 20°, and (d) 30°. The piezoelectric potential depending on the angle (e) 0°, (f) 10°, (g) 20°, and (h) 30°.

the nanowires at the edge region is decreased, i.e., $\overline{N}$ decreases. As a result, strong pressure over the critical pressure is applied to the nanowires. Second is the angle effect of the edge nanowires. The oblique nanowires were simulated to prove the enhancement of sensitivity, as shown in Figure 2.19. The same vertical pressure (10kPa) is applied to the various nanowires grown obliquely with angles (0°, 10°, 20°, 30°). Figure 2.18(a) to (d) show the displacement of nanowires depending on the angle of the grown nanowires, and Figure 2.19(e) to (h) show the piezoelectric potential of Figure 2.17(a) to (d) at the same pressure, respectively. Larger displacement and piezoelectric potential were observed in the large angle case. This is due to the lateral pressure component. The oblique nanowires are affected by the lateral pressure component, although vertical pressure is applied. Therefore, even a small θ value induces the lower critical pressure of the buckling effect when other factors are constant. As a result, the nanowires can be deformed easily when low stress is also applied to the nanowires. As shown in the SEM image of Figure 3.6(a) to (c), the edge nanowires are a little longer than that of the center nanowires. Because of the high slanderous ratio of the longer nanowires, the critical stress is also reduced by (2.4). As a result, the lateral pressure component and longer nanowires in the edge region decrease the critical stress of the buckling effect. Therefore, large deformation and high piezoelectric potential can occur at

low pressure level. (<14kPa) In the simulation result, the maximum piezoelectric potential of 30° is twice as higher than cases of 0°. The smaller the pattern size is, the larger the circumference to cell area ratio is induced. Therefore, the piezoelectric effect from edge nanowires considerably increases in the 20um pattern case. These simulated results prove that the density control and the buckling effect of nanowires considerably influenced the piezoelectric polarization of ZnO nanowires.

In this chapter, we have demonstrated the basic characteristics of ZnO nanowire and a structural solution for enhanced pressure sensitivity using ZnO nanowires for an artificial tactile sensor. The piezoelectric property of ZnO nanowires can play a role as the power source and pressure-sensing mechanism. To enhance pressure sensitivity, we changed a one-body cell design to smaller cell arrays (20um, 100um, and 250um) for the structural solution. As the fill factor of the ZnO nanowires was maintained at 50%, the pattern structure can reduce the density of nanowires and increase the force per unit area applied to the ZnO nanowire array. In addition, since the patterned cell structure induces an increase of nanowires on the edge of the cell structure, the oblique growth angle of the nanowires and the empty space between the square patterns helped the nanowires bend easily. Then, the pressure sensitivity enhanced drastically. These are proven through simulation data which corresponds well to the experimental results. As a result, the voltage and current sensitivity, depending on pressure variation, were increased by about three (1.3 mV/kPa to 3.6 mV/kPa) and 11 times (0.16 nA/kPa to 1.8 nA/kPa), respectively. The suggested idea and design are realized easily, with the result that it can be an attractive option to be applied to an artificial tactile sensor for android robots, disabled people, and other electrical devices.

2.7. Reference

[1] Y. Chuo, C. Landrock, B. Omrane, J. Aristizabal, J. N. Patel, M. Marzencki, and B. Kaminska, "Towards Self-Powering Touch/Flex-Sensitive OLED Systems," IEEE Sens J, vol. 11, pp. 2771-2779, 2011.

[2] B. P. Nabar, Z. Celik-Butler, and D. P. Butler, "Self-Powered Tactile Pressure Sensors Using Ordered Crystalline ZnO Nanorods on Flexible Substrates Toward Robotic Skin and Garments," IEEE Sens J, vol. 15, pp. 63-70, 2015.

[3] Y. Jeong, M. Sim, J. H. Shin, J.-W. Choi, J. I. Sohn, S. N. Cha, H. Choi, C. Moon, and J. E. Jang, "Psychological tactile sensor structure based on piezoelectric nanowire cell arrays," RSC Adv, vol. 5, pp. 40363-40368, 2015.

[4] Y. Yang, H. Zhang, Z.-H. Lin, Y. S. Zhou, Q. Jing, Y. Su, J. Yang, J. Chen, C. Hu, and Z. L. Wang, "Human skin based triboelectric nanogenerators for harvesting biomechanical energy and as self-powered active tactile sensor system," Acs Nano, vol. 7, pp. 9213-9222, 2013.

[5] L. Shu, X. Tao, and D. D. Feng, "A new approach for readout of resistive sensor arrays for wearable electronic applications," IEEE Sens J, vol. 15, pp. 442-452, 2015.

[6] B. Zhu, Z. Niu, H. Wang, W. R. Leow, H. Wang, Y. Li, L. Zheng, J. Wei, F. Huo, and X. Chen, "Microstructured graphene arrays for highly sensitive flexible tactile sensors," Small, vol. 10, pp. 3625-3631, 2014.

[7] S. Kim, W. Choi, W. Rim, Y. Chun, H. Shim, H. Kwon, J. Kim, I. Kee, S. Kim, and S. Lee, "A highly sensitive capacitive touch sensor integrated on a thin-film-encapsulated active-matrix OLED for ultrathin displays," IEEE T Eelectron Dev, vol. 58, pp. 3609-3615, 2011.

[8] S. C. Mannsfeld, B. C. Tee, R. M. Stoltenberg, C. V. H. Chen, S. Barman, B. V. Muir, A. N. Sokolov, C. Reese, and Z. Bao, "Highly sensitive flexible pressure sensors with microstructured rubber dielectric layers," Nat Mater, vol. 9, pp. 859-864, 2010.

[9] H. Athenstaedt, H. Claussen, and D. Schaper, "Epidermis of human skin: pyroelectric and piezoelectric sensor layer," Science, vol. 216, pp. 1018-1020, 1982.

[10] H.-B. Lin, M.-S. Cao, Q.-L. Zhao, X.-L. Shi, D.-W. Wang, and F.-C. Wang, "Mechanical reinforcement and piezoelectric properties of nanocomposites embedded with ZnO nanowhiskers," Scripta Mater, vol. 59, pp. 780-783, 2008.

[11] M. Sasmal, T. K. Maiti, and T. K. Bhattacharyya, "Synthesis of ZnO nanosphere for picomolar level detection of bovine serum albumin," IEEE T Nanobiosci, vol. 14, pp. 129-137, 2015.

[12] M. Sasmal, T. K. Maiti, and T. K. Bhattacharyya, "Ultra-Low Level Detection of L-Histidine Using Solution-Processed ZnO Nanorod on Flexible Substrate," IEEE T Nanobiosci, vol. 14, pp. 634-640, 2015.

[13] R. Viter, V. Khranovskyy, N. Starodub, Y. Ogorodniichuk, S. Gevelyuk, Z. Gertnere, N. Poletaev, R. Yakimova, D. Erts, and V. Smyntyna, "Application of room temperature photoluminescence from ZnO nanorods for Salmonella detection," IEEE Sens J, vol. 14, pp. 2028-2034, 2014.

[14] W. Wu, X. Wen, and Z. L. Wang, "Taxel-addressable matrix of vertical-nanowire piezotronic transistors for active and adaptive tactile imaging," Science, vol. 340, pp. 952-957, 2013.

[15] C. Pan, L. Dong, G. Zhu, S. Niu, R. Yu, Q. Yang, Y. Liu, and Z. L. Wang, "High-resolution electroluminescent imaging of pressure distribution using a piezoelectric nanowire LED array," Nat Photonics, vol. 7, pp. 752-758, 2013.

[16] F. N. Meyers, K. J. Loh, J. S. Dodds, and A. Baltazar, "Active sensing and damage detection using piezoelectric zinc oxide-based nanocomposites," Nanotechnology, vol. 24, p. 185501, 2013.

[17] M. Y. Choi, D. Choi, M. J. Jin, I. Kim, S. H. Kim, J. Y. Choi, S. Y. Lee, J. M. Kim, and S. W. Kim, "Mechanically powered transparent flexible charge-generating nanodevices with piezoelectric ZnO nanorods," Adv Mater, vol. 21, pp. 2185-2189, 2009.

[18] B. O. Jun, G. J. Lee, J. G. Kang, S. Kim, J.-W. Choi, S. N. Cha, J. I. Sohn, and J. E. Jang, "Wireless thin film transistor based on micro magnetic induction coupling antenna," Sci Rep, vol. 5, 2015.

[19] S. Baruah and J. Dutta, "Hydrothermal growth of ZnO nanostructures," Sci. Technol.

Adv. Mater, vol. 10, p. 013001, 2009.

[20] H. Gullapalli, V. S. Vemuru, A. Kumar, A. Botello-Mendez, R. Vajtai, M. Terrones, S. Nagarajaiah, and P. M. Ajayan, "Flexible piezoelectric ZnO–paper nanocomposite strain sensor," small, vol. 6, pp. 1641-1646, 2010.

[21] X. Chen, S. Xu, N. Yao, and Y. Shi, "1.6 V nanogenerator for mechanical energy harvesting using PZT nanofibers," Nano lett, vol. 10, pp. 2133-2137, 2010.

[22] K. I. Park, M. Lee, Y. Liu, S. Moon, G. T. Hwang, G. Zhu, J. E. Kim, S. O. Kim, D. K. Kim, and Z. L. Wang, "Flexible nanocomposite generator made of BaTiO3 nanoparticles and graphitic carbons," Adv Mater, vol. 24, pp. 2999-3004, 2012.

[23] C. K. Jeong, K. I. Park, J. Ryu, G. T. Hwang, and K. J. Lee, "Large-Area and Flexible Lead-Free Nanocomposite Generator Using Alkaline Niobate Particles and Metal Nanorod Filler," Adv Funct Mater, vol. 24, pp. 2620-2629, 2014.

[24] Wang, Z. L. “ZnO nanowire and nanobelt platform for nanotechnology”, Materials Science and Engineering: R: Reports, 64(3-4), 2009, pp. 33-71.

[25] Jagadish, C., and Pearton, S. J. “Zinc oxide bulk, thin films and nanostructures: processing, properties, and applications”, 2011, Elsevier.

[26] Goldberger, J., Sirbuly, D. J., Law, M., and Yang, P. “ZnO nanowire transistors”, The Journal of Physical Chemistry B, 109(1), 2005, pp. 9-14.

[27] Soci, C., Zhang, A., Xiang, B., Dayeh, S. A., Aplin, D. P. R., Park, J., Bao. X. Y., Lo. Y. H. and Wang, D. “ZnO nanowire UV photodetectors with high internal gain”, Nano letters, 7(4), 2007, pp. 1003-1009.

[28] Dulub, O., Boatner, L. A., and Diebold, U., “STM study of the geometric and electronic structure of ZnO (0001)-Zn,(0001)-O,(1010), and (1120) surfaces”, Surface Science, 519(3), 2002, pp. 201-217.

[29] Meyer, B., and Marx, D. “Publisher’s Note: Density-functional study of the structure and stability of ZnO surfaces”, Physical Review B, 67(3), 2003, 039902.

[30] Ko, S. H., Lee, D., Kang, H. W., Nam, K. H., Yeo, J. Y., Hong, S. J., Grigoropoulos. C. P., and Sung, H. J. “Nanoforest of hydrothermally grown hierarchical ZnO nanowires

for a high efficiency dye-sensitized solar cell", Nano letters, 11(2), 2011, pp. 666-671.

[31] Shibata, T., Unno, K., Makino, E., Ito, Y., and Shimada, S. "Characterization of sputtered ZnO thin film as sensor and actuator for diamond AFM probe", Sensors and Actuators A: Physical, 102(1-2), 2002, pp. 106-113.

[32] Wang, Z. L., and Song, J. "Piezoelectric nanogenerators based on zinc oxide nanowire arrays", Science, 312(5771), 2006, pp. 242-246.

[33] Yang, Y., Guo, W., Pradel, K. C., Zhu, G., Zhou, Y., Zhang, Y., Hu. Y., Lin. L., and Wang, Z. L. "Pyroelectric nanogenerators for harvesting thermoelectric energy", Nano letters, 12(6), 2012, pp. 2833-2838.

[34] Rivera, V. F., Auras, F., Motto, P., Stassi, S., Canavese, G., Celasco, E., Bein. T., Onida. B., and Cauda, V. "Length-Dependent Charge Generation from Vertical Arrays of High-Aspect-Ratio ZnO Nanowires", Chemistry–A European Journal, 19(43), 2013, pp. 14665-14674.

[35] A. Djurišić, Y. Leung, K. Tam, Y. Hsu, L. Ding, W. Ge, Y. Zhong, K. Wong, W. Chan, H. Tam, Defect emissions in ZnO nanostructures. Nanotechnol, 2007, 18, 095702.

[36] K. Tam, C. Cheung, Y. Leung, A. Djurišic, C. Ling, C. Beling, S. Fung, W. Kwok, W. Chan, D. Phillips, Defects in ZnO nanorods prepared by a hydrothermal method. J. Phys. Chem. B, 2006, 110, 20865-20871.

[37] K. M. Wong, S. Alay-e-Abbas, Y. Fang, A. Shaukat, Y. Lei, Spatial distribution of neutral oxygen vacancies on ZnO nanowire surfaces: An investigation combining confocal microscopy and first principles calculations. J. Appl. Phys, 2013, 114, 034901.

[38] J. Fan, Y. Hao, C. Munuera, M. García-Hernández, F. Güell, E. M. Johansson, G. Boschloo, A. Hagfeldt, A. Cabot, Influence of the annealing atmosphere on the performance of ZnO nanowire dye-sensitized solar cells. J. Phys. Chem. C, 2013, 117, 16349-16356.

[39] W. Mtangi, F. D. Auret, W. Meyer, M. Legodi, P. J. van Rensburg, S. Coelho, M. Diale, J. Nel, Effects of hydrogen, oxygen, and argon annealing on the electrical properties of ZnO and ZnO devices studied by current-voltage, deep level transient spectroscopy,

and Laplace DLTS. J. Appl. Phys, 2012, 111, 094504.

[40] Lee, S., Lee, J., Ko, W., Cha, S., Sohn, J., Kim, J., Park. J., Park. Y., and Hong, J. “Solution-processed Ag-doped ZnO nanowires grown on flexible polyester for nano-generator applications”, Nanoscale, 5(20), 2013, pp. 9609-9614.

[41] Zhu, G., Wang, A. C., Liu, Y., Zhou, Y., and Wang, Z. L. “Functional electrical stimulation by nanogenerator with 58 V output voltage”, Nano letters, 12(6), 2012, pp. 3086-3090.

[42] Kim, D., Lee, K. Y., Gupta, M. K., Majumder, S., and Kim, S. W. “Self-compensated insulating ZnO-based piezoelectric nanogenerators”, Advanced Functional Materials, 24(44), 2014, pp. 6949-6955.

[43] Sohn, J. I., Cha, S. N., Song, B. G., Lee, S., Kim, S. M., Ku, J., Kim. H. J., Park. Y. J., Choi. B. Y., Wang. Z. L., Kim, J. M., and Kim. K., “Engineering of efficiency limiting free carriers and an interfacial energy barrier for an enhancing piezoelectric generation”, Energy & Environmental Science, 6(1), 2013, 97-104.

[44] S. Xu, Y. Qin, C. Xu, Y. Wei, R. Yang, and Z. L. Wang, "Self-powered nanowire devices," Nat Nanotechnol, vol. 5, pp. 366-373, 2010.

[45] B. H. Kim and J. W. Kwon, "Metal catalyst for low-temperature growth of controlled zinc oxide nanowires on arbitrary substrates," Sci Rep, vol. 4, 2014.

[46] K. Tam, C. Cheung, Y. Leung, A. Djurišic, C. Ling, C. Beling, S. Fung, W. Kwok, W. Chan, and D. Phillips, "Defects in ZnO nanorods prepared by a hydrothermal method," J Phys Chem B, vol. 110, pp. 20865-20871, 2006.

[47] V. F. Rivera, F. Auras, P. Motto, S. Stassi, G. Canavese, E. Celasco, T. Bein, B. Onida, and V. Cauda, "Length-Dependent Charge Generation from Vertical Arrays of High-Aspect-Ratio ZnO Nanowires," Chem. Eur. j, vol. 19, pp. 14665-14674, 2013.

[48] Z. L. Wang and J. Song, "Piezoelectric nanogenerators based on zinc oxide nanowire arrays," Science, vol. 312, pp. 242-246, 2006.

[49] W. Deng, L. Jin, B. Zhang, Y. Chen, L. Mao, H. Zhang, and W. Yang, "A flexible field-limited ordered ZnO nanorod-based self-powered tactile sensor array for electronic

skin," Nanoscale, vol. 8, pp. 16302-16306, 2016.

[50] B. P. Nabar, Z. Celik-Butler, and D. P. Butler, "Self-powered, tactile pressure sensing skin using crystalline ZnO nanorod arrays for robotic applications," in SENSORS, 2013 IEEE, 2013, pp. 1-4.

[51] M. Ha, S. Lim, J. Park, D. S. Um, Y. Lee, and H. Ko, "Bioinspired Interlocked and Hierarchical Design of ZnO Nanowire Arrays for Static and Dynamic Pressure-Sensitive Electronic Skins," Adv Funct Mater, vol. 25, pp. 2841-2849, 2015.

[52] T. Sharma, S.-S. Je, B. Gill, and J. X. Zhang, "Patterning piezoelectric thin film PVDF–TrFE based pressure sensor for catheter application," Sens. Actuators, A, vol. 177, pp. 87-92, 2012.

[53] W. Choi, J. Lee, Y. K. Yoo, S. Kang, J. Kim, and J. H. Lee, "Enhanced sensitivity of piezoelectric pressure sensor with microstructured polydimethylsiloxane layer," Appl. Phys. Lett., vol. 104, p. 123701, 2014.

[54] J. S. Lee, K.-Y. Shin, O. J. Cheong, J. H. Kim, and J. Jang, "Highly sensitive and multifunctional tactile sensor using free-standing ZnO/PVDF thin film with graphene electrodes for pressure and temperature monitoring," Sci Rep, vol. 5, 2015.

[55] A. Ugural, "Mechanics of materials, 1991," ed: McGraw Hill, New York.

III. DOME STRUCTURE TO MEAUSRE THE SURFACE INFORMATION

3.1. Introduction

Conventional tactile sensor detecting the pressure or temperature have been widely developed and the performance of these sensors like the sensitivity, durability, stability, and flexibility has been considerably improved by the effort of many researcher.[1-6] However, for mimicking the tactile sense of human, there are many other issues and one of the issues is the roughness sensing when the skin is in contact with or rubs certain materials. Currently, because the roughness sensing mechanism of human skin is not still perfectly investigated and results from the combination of various parameters, such as the surface morphology, hardness, pitch of pattern, and the temperature, many researches using deep learning or machine learning have been developed to efficiently process the information like the pressure, temperature and frequency from conventional tactile sensor.[7-13] However, fundamentally, to understand various parameters generating the roughness feeling, the researches for much more improvement of the roughness sensor should be carried out.

Generally, when the finger or other part of skin rubs the object, the human feels the surface roughness. Specially, because the signal by rubbing the surface is smaller than that by pushing action, it is important to amplify the generated signal. At that time, the frictional ridge of the epidermis, called the fingerprint, plays an important role to amplify and there are some researches mimicking the fingerprint to enhance the sensitivity have been conducted.[14-18] Specially, in our previous research, pin-type structure similar to the atomic force microscopy (AFM) was applied to the tactile sensor to obtain and analyze the surface information such as the surface topography, the angle of slope, the sliding speed and so on.[19]

Although the pin-type structure can successfully measure the information, their bulky structure limits the possibility of commercialization.

Here, we demonstrate the basic characteristics of P(VDF-TrFE) thin film to enhance the piezoelectric coefficient and simple special structure based on PDMS is proposed to obtain the surface information like fingerprint of human. Firstly, to find the optimized structure, three kinds of the structure shape (cone, cylinder and dome) are fabricated and the pressure sensitivity according to the shape are also measured. Then, FEM simulation supporting the experimental result is also carried out. After optimizing the shape of structure, the sliding test using the structure with different height is also conducted to investigate the effect of the structure height. Our tactile sensor with optimized dome structure provides high shear force sensitivity, fast response time, stability, and durability and so on. Specially, the high sensitivity about the shear force enables the tactile sensor to measure the various surface information such as the depth, pitch of pattern, hardness and so on.

3.2. Basic characteristics of P(VDF-TrFE)

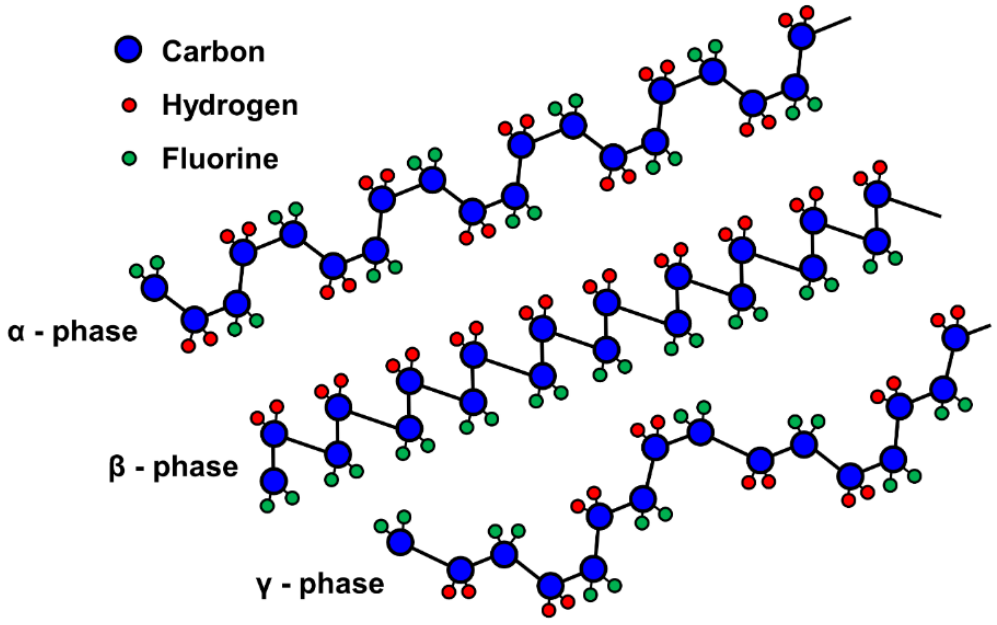

Figure 3.1. The various phase structure of polymerized P(VDF-TrFE)

Property	*Unit*	*Biaxially oriented film*	*Uniaxially oriented film*
d_{31}	$10^{-12}CN^{-1}$	4.34	21.4
d_{32}		4.36	2.3
d_{33}		-12.4	-31.5
d_h		-4.8	-9.6
p_3	$10^{-5}Cm^{-2}K^{-1}$	-1.25	-2.74
a_{11}	$10^{-4}K^{-1}$	1.24	0.13
a_{22}		1.00	1.45
s_{11}	$10^{-10}Pa^{-1}$	4.0	4.0
s_{12}		-1.57	-1.57
c_{11}	$10^{9}Pa$	5.04	5.04
c_{12}		3.25	3.25

Table 3.1. Material coefficients of PVDF polymer. Piezoelectric and Pyroelectric coefficient, thermal expansion coefficient, elastic constant and compliances.

ZnO nanowire showed the weak durability after the measurement. Despite of the structural solution in previous section, the piezoelectric efficiency of ZnO nanowire is still low. In following experiments, the higher piezoelectric efficiency should be needed to measure the shear force. So, the piezoelectric material is changed from ZnO nanowire to P(VDF-TrFE). PVDF (Polyvinylidene fluoride) is the polymerized monomer(-CH_2-CF_2-) with various phases (α, β, γ, δ-PVDF) with the dipole moment of $\mu = 7 \times 10^{-30}$Cm at the C-F bond.[2] Even if there are a series of phases organizing the PVDF polymer, the macroscopic dipole moment can be generated at only β phase. Following figure shows the alignment of the dipole in alpha and beta phase. In alpha phase of molecular structure, net dipole is zero by compensation. On the other hand, the PVDF of beta phase has the macroscopic dipole moment like Figure 3.1. However, after the synthesis, PVDF is not beta phase crystalline but the amorphous state. Generally, because the crystalline beta phase ends up the range 40 ~ 60%, the piezoelectric characteristics is poor. Therefore, there are two methods to align the electric dipole of beta phase at C-F bond in parallel and enhance the piezoelectric prop-

erty. The crystallinity of PVDF can be enhanced by the anneal process under the curie temperature (130℃) during several hours. Additionally, at evaluated temperature, the poling process at high electric field from 50 ~ 300kV/mm aligns more the dipole moment in macroscopic regions. The poling process is conducted without mechanical deformation. Both poling procedure effective symmetry. Various characteristics of poled PVDF is like Table 3.1. Sometimes, for increasing the beta phase crystallinity ratio of PVDF up to 90%, the copolymer with TrFE (trifluoroethylene) is used. The superior piezoelectric characteristic is obtained by P(VDF-TrFE) copolymer. Generally, the range of the molar ratio of copolymer with TrFE is from 20 to 40%. As a result, electromechanical coupling factor k is maximized at this molar ratio. The electromechanical coupling factor k is defined by

$$k^2 = \frac{Electrical\ energy\ converted\ to\ mechanical\ energy}{Input\ of\ electrical\ energy} \tag{3.1}$$

or

$$k^2 = \frac{Mechanical\ energy\ converted\ to\ electiral\ energy}{Input\ of\ mechanical\ energy} \tag{3.2}$$

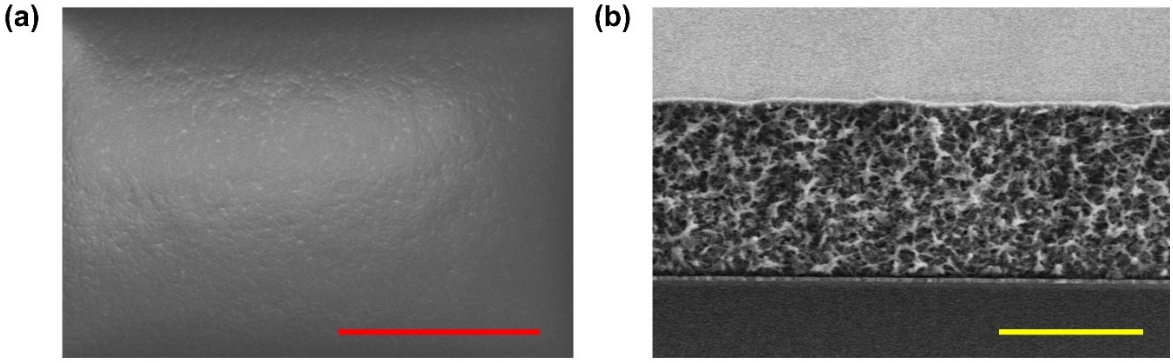

Figure 3.2. The SEM image of P(VDF-TrFE) thin film coated with 3000rpm (a) top view and (b) cross-sectional view. The red scale bar is 30um and the yellow scale bar is 3um. spin-coated P(VDF-TrFE) thin film with 3000 rpm.

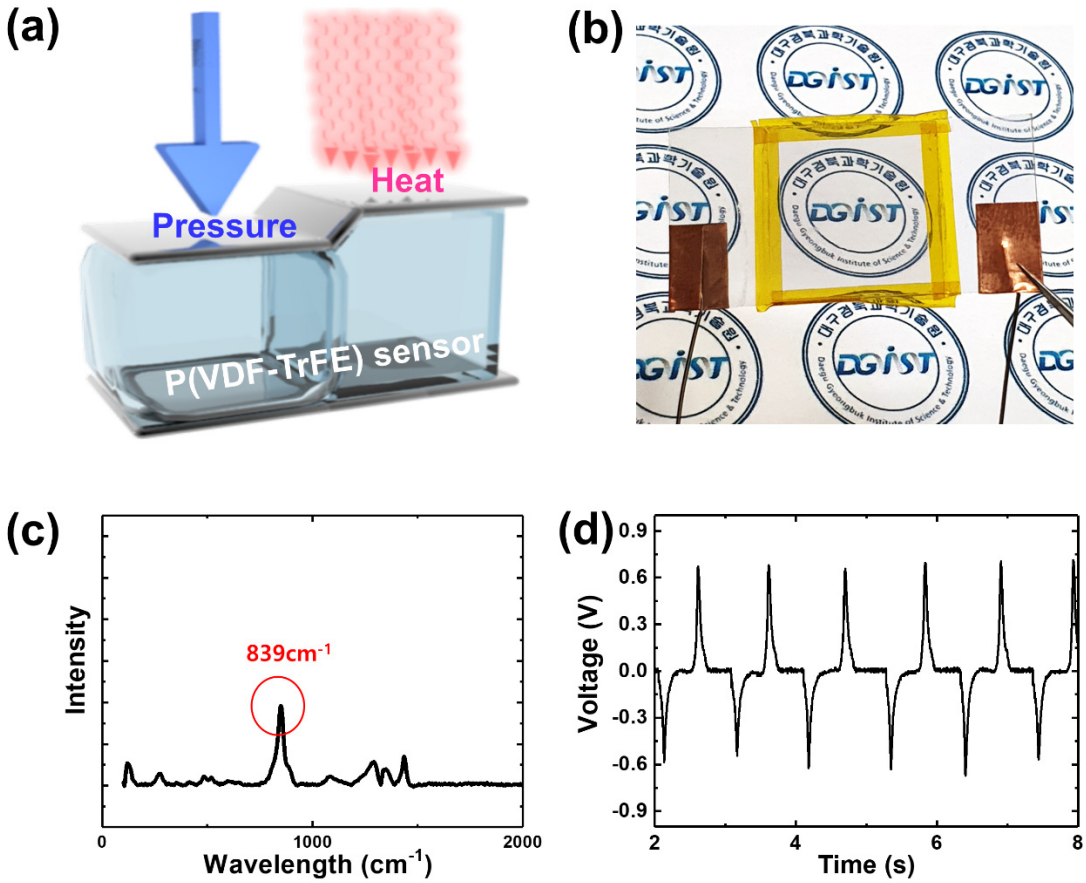

Figure 3.3. (a) The schematic of tactile sensor based on the P(VDF-TrFE) thin film, (b) the image of fabricated tactile sensor, (c) Raman shift of thin film and (d) the piezoelectric voltage from the fabricated tactile sensor.

First, in this study, P(VDF-TrFE) powder (75/25 in Mole %) from PIEZOTECH is used for P(VDF-TrFE) thin film fabrication and 2-butanone from Sigma Aldrich CO is chosen for the solvent dissolving the P(VDF-TrFE) powder. The concentration of solution is about 15 wt% for high piezoelectric efficiency. The calculation formula of weight percent is following.

$$\text{wt } \% = \frac{P(VDF-TrFE)\ weight}{Solvent\ weight+P(VDF-TrFE)} \times 100\% \qquad (3.3)$$

After that, to dissolve the powder, the stirring with 600 rpm is conducted for 2 h. The fabricated solution should be sealed by the parafilm because the solvent is well evaporated and the characteristics of the solution is changed. To fabricated the piezoelectric thin

film, the fabricated solution is spin-coated on the conductive substrate with 3000 rpm. Then, the thermal annealing at 130℃ is carried out for 2h to enhance the piezoelectric characteristic by increasing the ratio of β-phase P(VDF-TrFE). The thickness of P(VDF-TrFE) is about 3.6um (yellow scale bar: 3um) in Figure 3.2(b). Simple sensor based on P(VDF-TrFE) is fabricated to confirm the electrical characteristics of P(VDF-TrFE), like Figure 3.3(a). The fabricated simple sensor is transparent due to the transparency property of P(VDF-TrFE) thin film in Figure 3.3(b). Then, to confirm β-phase crystallinity of P(VDF-TrFE) after annealing, Raman shift is measured in Figure 3.3(c). The high peak at 839cm^{-1} means that the dominant phase in P(VDF-TrFE) thin film is β-phase and the annealing is successful.[21,22] The piezoelectricity of β-phase P(VDF-TrFE) generates the piezoelectric voltage when the external pressure is applied to the pressure sensor like Figure 3.3(d). The measured piezoelectric voltage and pressure sensitivity with increasing the force from 0.4N to 1.4N is presented in Figure 3.4(a) and (b). These results confirm that this material can effectively react to various pressure levels with good sensitivity. Figure 3.5(a) and (b) show the piezoelectric and the pyroelectric signal by room temperature and warmed water droplets.

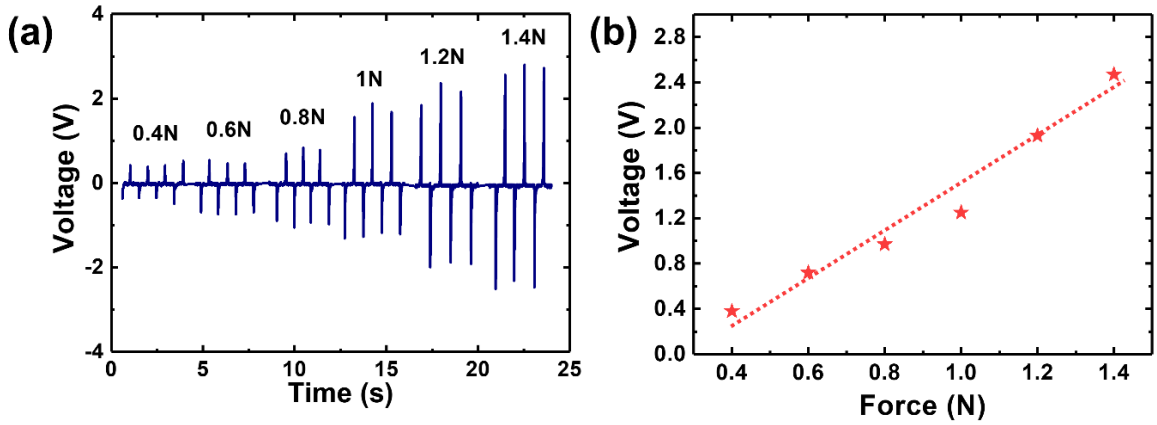

Figure 3.4. (a) The measured voltage and (b) pressure sensitivity of P(VDF-TrFE)-based tactile sensor with increasing the force from 0.4N to 1.4N

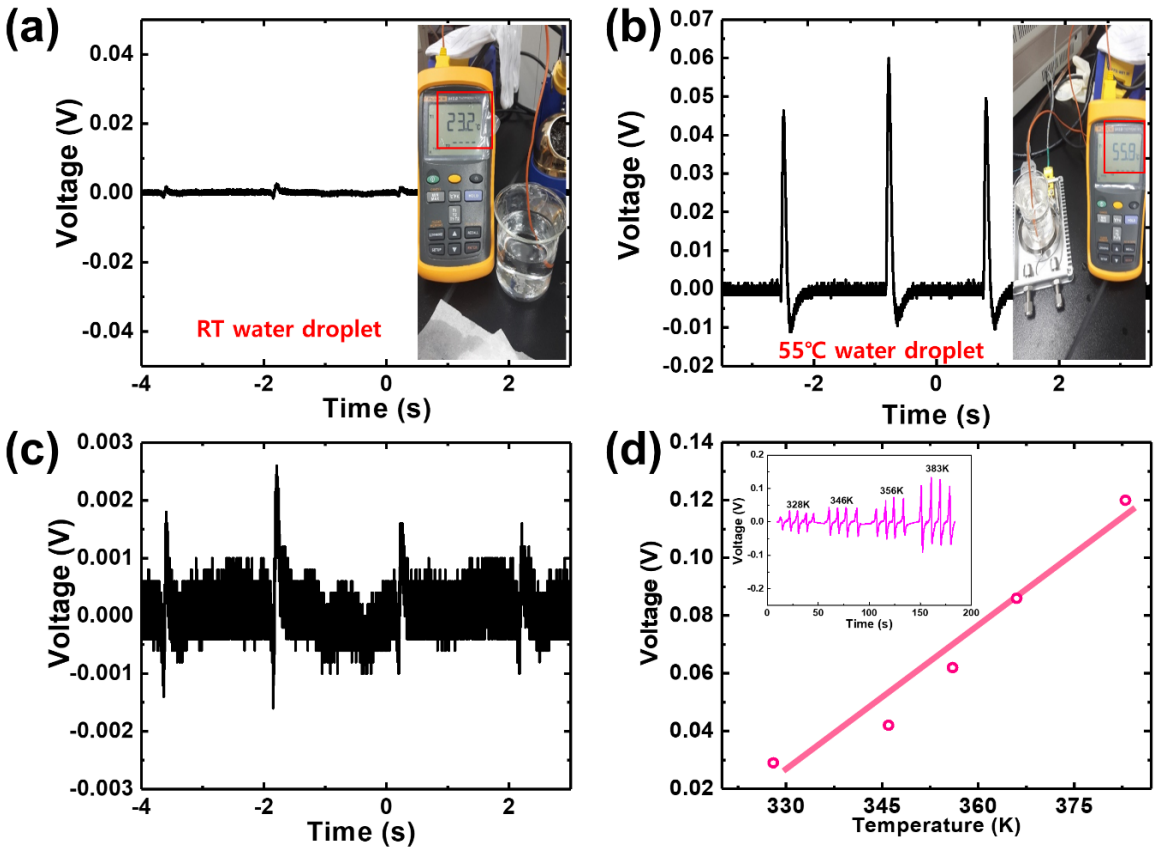

Figure 3.5. (a) The piezoelectric and (b) pyroelectric by Room temperature and warmed droplet, (c) the magnitude graph of (a), and (d) the pyroelectric voltage from 328K to 383K.

Although a quite small pressure was applied to the sensor (a water droplet of 1g & room temperature) was dropped 1cm apart, the piezoelectric signal was detected well in enlarged graph (Figure 3.5(c)). When a warm water droplet (55°C) was contacted directly on the surface of the sensor-it means that pressure was quite low and almost nothing, the pyroelectric signal was generated in the sensor structure in Figure 3.5(b). The temperature sensitivity of pyroelectric effect from 328K to 383K in Figure 3.5(d). The sensitivities increase linearly according to the applied pressure and temperature level. Therefore, P(VDF-TrFE) material can be a good candidate material for artificial tactile sensor structure in terms of sensitivity. However, an issue is the selectivity. From signal forms and its levels, it is hard to know whether the stimuli source is pressure or temperature like the case of Figure 3.6. Moreover, in the case of multiple stimulus (pressure + heat), the signal separation

between two sources is much more difficult, because the piezoelectric effect is generally much higher than the pyroelectric effect as well as the similarity of signal forms. Therefore, to confirm this compensation effect between the piezo and pyroelectric effect, the P(VDF-TrFE) tactile sensor is pressed with different pressure and temperature in Figure 3.6(a) to (c). Even if the high temperature material is applied to the pressure sensor, the piezoelectric effect is only observed in Figure 3.6(c). As shown in Figure 3.6(d), when the temperature variation with same pressure was applied to tactile sensor, special difference between wave-forms is not observed. Since the piezoelectric and pyroelectric effects are based on the equivalent principle, the piezo-pyroelectric sensor does not distinguish simply the stimulus source by the measured electrical signal.

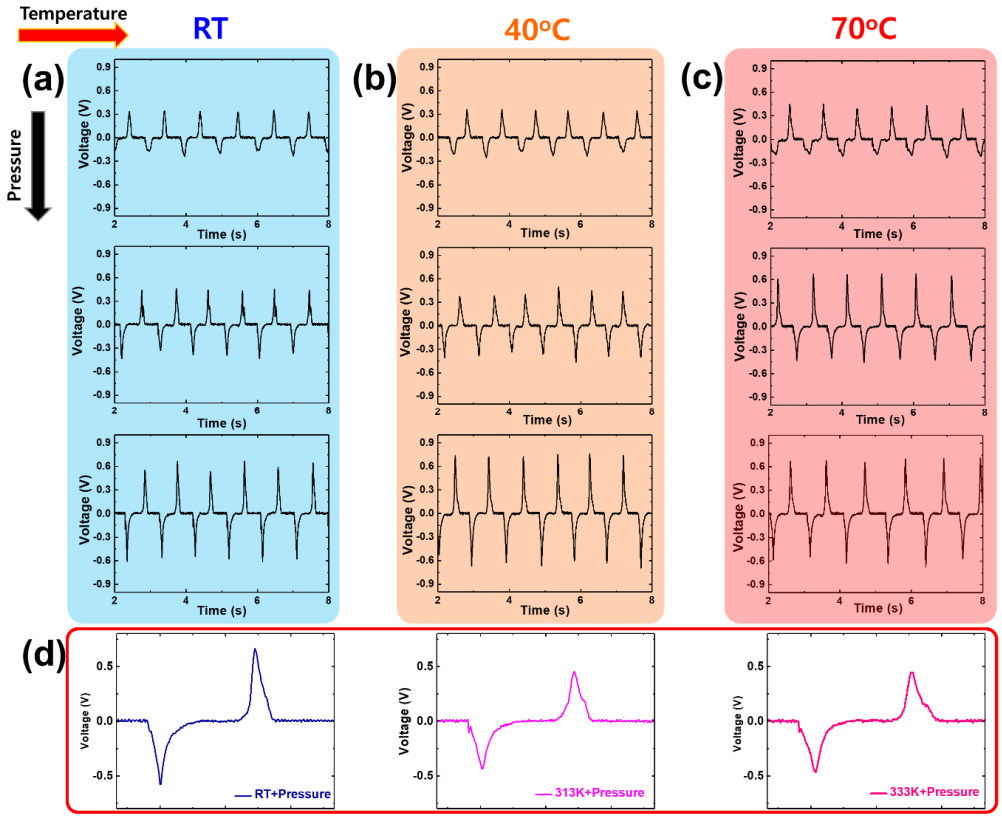

Figure 3.6. The piezo-pyroelectric effect when the pressure and temperature are applied to the tactile sensor simultaneously. The piezoelectric effect with increasing the pressure when the temperature is (a) Room Temperature, (b) 40 ℃ and (b) 70 ℃, (d) the similar shape of the piezoelectric effect with different temperature and same pressure.

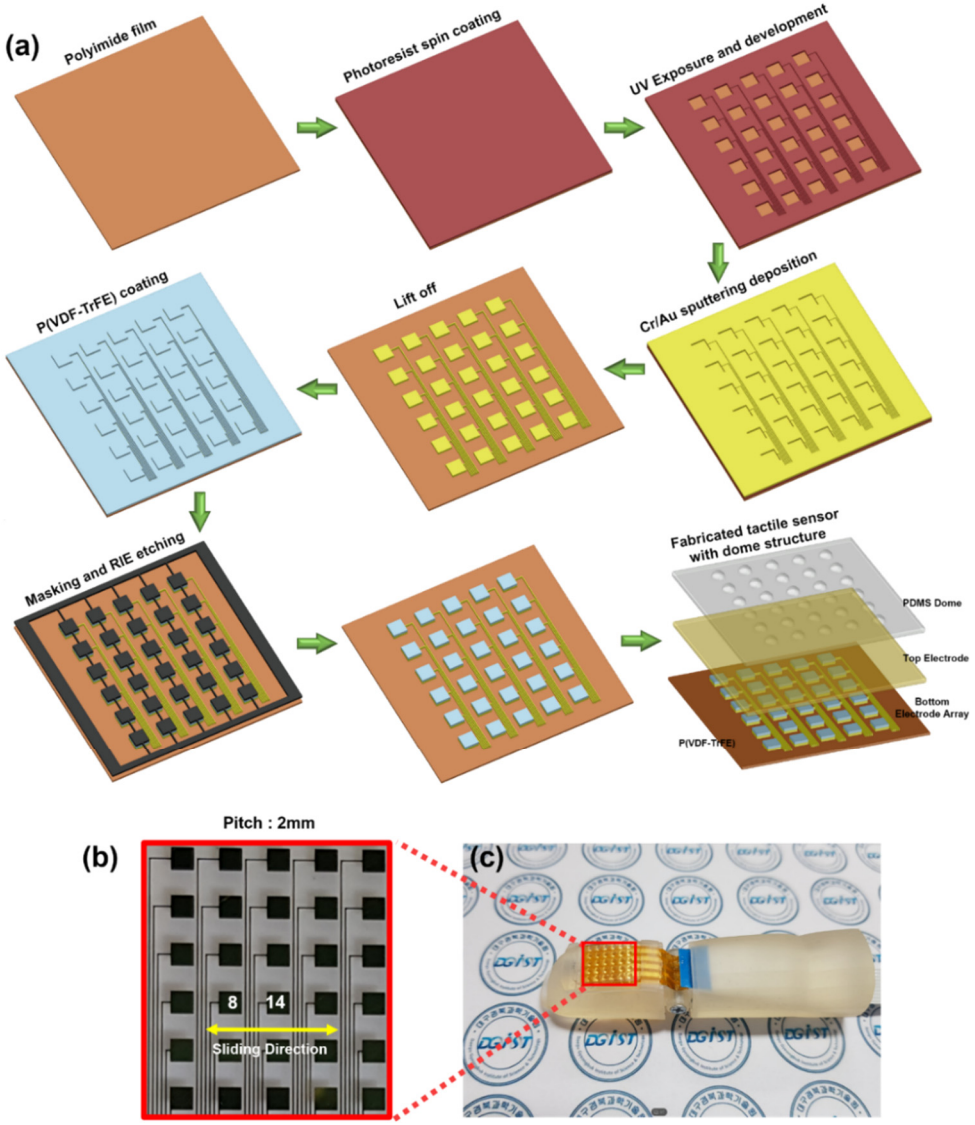

Figure 3.7. (a) Fabrication process of tactile sensor, the image of (b) fabricated tactile sensor and (c) embedded in artificial finger.

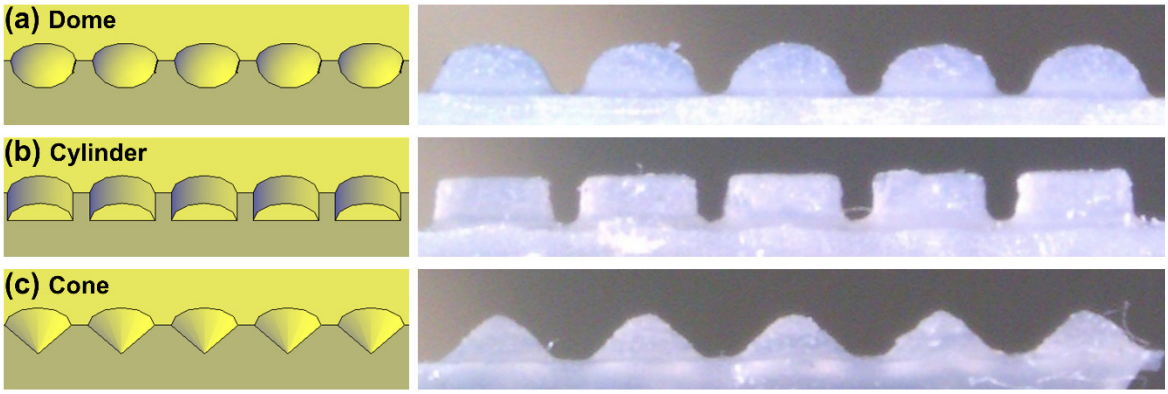

Figure 3.8. 3D CAD design and the SEM images for fabricating PDMS mold and fabricated PDMS, (a) dome shape, (b) cylinder shape, (c) cone shape

3.3. Device Fabrication

Figure 3.7(a) schematically illustrates the fabrication process of tactile sensor. It consisted of a pair of electrodes, P(VDF-TrFE) as the primary material, and a dome structure to amplify the piezoelectric signal, similar to a finger print. First, the negative photoresist (nLof 2035) is spin-coated on polyimide film of 3 × 4 cm^2 at 3000 rpm. To fabricate the pattern of bottom electrode, UV exposure (70mJ/cm^2) and development (AZ MIF 300 for 70 sec) are following. Cr/Au (10nm/100nm) layer as the bottom electrode is deposited by DC sputtering. Unnecessary metal layer was removed by a lift off process. Then, to fabricate P(VDF-TrFE) thin film for the piezoelectric effect, the P(VDF-TrFE) (75/25) powder of Piezotech is dissolved in 2-butanone to make a 15 wt% P(VDF-TrFE) solution. The mixture of powder and solvent is stirred at 600 rpm without heating for 2 hours to dissolve the P(VDF-TrFE) powder. After dissolving the powder, the solution is spin-coated on the pattern fabricated by previous process at 3000 rpm. Thermal annealing of P(VDF-TrFE) is following at 130°C for 2 h. Finally, the piezoelectric layer on the electrode line is removed by RIE etching process to reduce the cross-talk effect between adjacent sensing cells. The sensor had a 1 × 1 mm^2 cell size and 2-mm pitch (Figure 3.7(b)). To fabricate the tactile sensor, the top electrode and PDMS dome structure are placed on the sensing cells. In Figure 3.8, the special structure for enhancing the piezoelectric effect is fabricated by 3D printed mold and PDMS solution. Firstly, the mold with three shape (cone, cylinder and dome) is designed by 3D CAD program (AUTOCAD 2019). The molds are 3D-printed (ProJet 3500) for the cone, cylinder, and dome, with the radius and height of 1 mm and 0.5 mm in all cases, respectively. PDMS solution was produced by shaking the base oil and hardener (10:1). Air bubbles produced by shaking are removed over 30 min in a vacuum desiccator. Finally, the solution is poured into the 3D mold and left to harden for 12 h at 60 ℃.

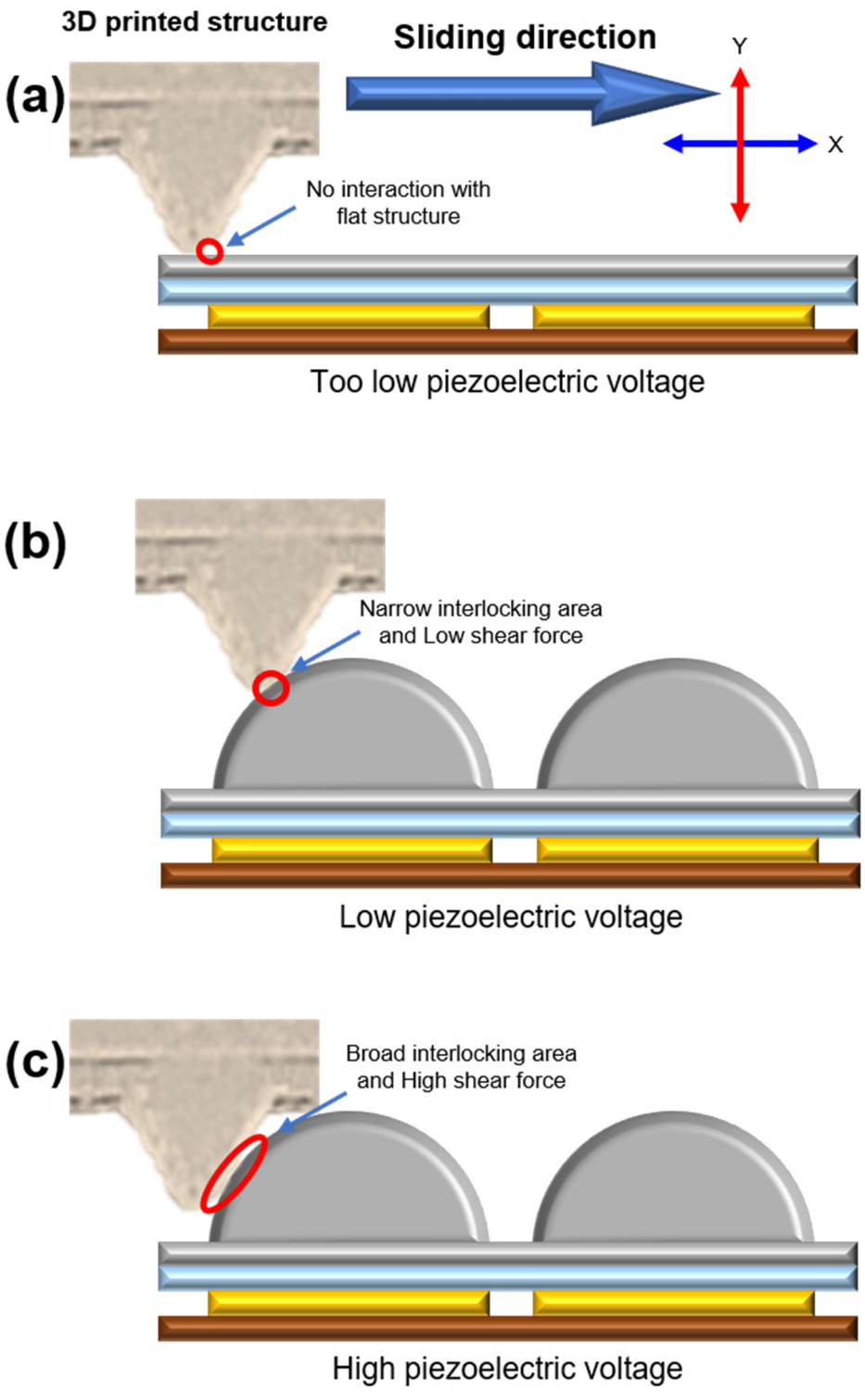

Figure 3.9. The schematic of the interlocking situation with dome structure, (a) no interaction of flat structure, (b) small interaction and big interaction between the surface and dome structure.

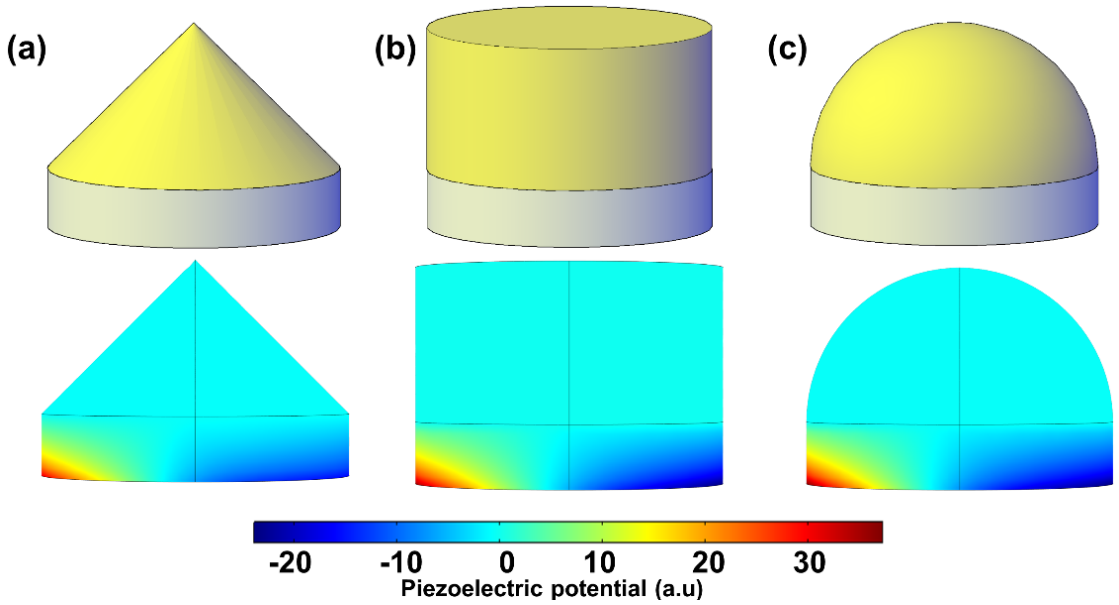

Figure 3.10. The pair of the 3D CAD design for simulation and results (a) cone, (b) cylinder, and (c) dome structure.

3.4. Interaction mechanism between dome structure and surface material

The pressure sensor detecting the force of normal direction is generally fabricated with flat surface because of simple fabrication process and device structure. Additionally, the flat surface of pressure sensor is a little bit more advantageous than that having special structure such as bump, pillar, or curved shape because certain structure distorts the delivery of force to the sensor. However, these flat surfaces are very disadvantageous when the sensor should obtain the surface information by sensing the shear force because the flat surface of sensor can't interact with random structure of certain materials like Figure 3.9(a). However, for instance, if the dome structure is applied to the tactile sensor like Figure 3.9(b) and (c), the surface structure of the materials is interacted with the dome structure well.[23-30] In this case, the interaction between the dome and the materials generates the shear force and deforms the dome structure. The shear force generated by the interaction is converted to the force of normal direction. As a result, the converted normal force pushes the piezoelectric

element like Figure 3.9(b) and (c). If the surface structure having low depth is applied to the dome structure, the low piezoelectric voltage is generated due to low shear and converted normal force in Figure 3.9(b). On the contrary, the materials having deep depth result in the higher interaction and piezoelectric effect like Figure 3.9(c). The difference of the piezoelectric effect according to the depth of surface structure consequently reflects the surface information.

3.5. Simulation and Experimental result comparing cone, cylinder, and dome structure

To confirm the amplifying effect by various structure such as cone, cylinder, and dome, FEM simulation and pressure sensitivity are carried out in Figure 3.10 and Figure 3.11. For similar situation in simulation, PVDF layer and the shape are designed by 3D CAD program like Figure 3.10 (a) to (c). The image of simulation in Figure 3.10 is the piezoelectric potential at PVDF layer when the shear force of 1 N is applied to PDMS structure. In Figure 3.11(a), the simulation result with increasing the force indicates that the cylinder and dome structure well convert the shear force to the normal force. As a result, the piezoelectric potential in PVDF film is higher than that of cone structure. Then, to prove the simulation result about the pressure sensitivity and confirm the durability of PDMS structure, the sliding test is carried out. Figure 3.11(b) to (c) show the pressure sensitivity in accordance with the structure shape. In the result, the pressure sensitivity of cone (Figure 3.11(b)) and dome (Figure 3.11(d)) shape indicates more linear property than that of cylinder shape (Figure 3.9(c)). This is probably because it is weak durability. Actually, the cylinder shape is destroyed after several measurement process even if the pressure sensitivity is higher than that of cone shape. In the case of cone shape, even if the durability is the best, the amplifying

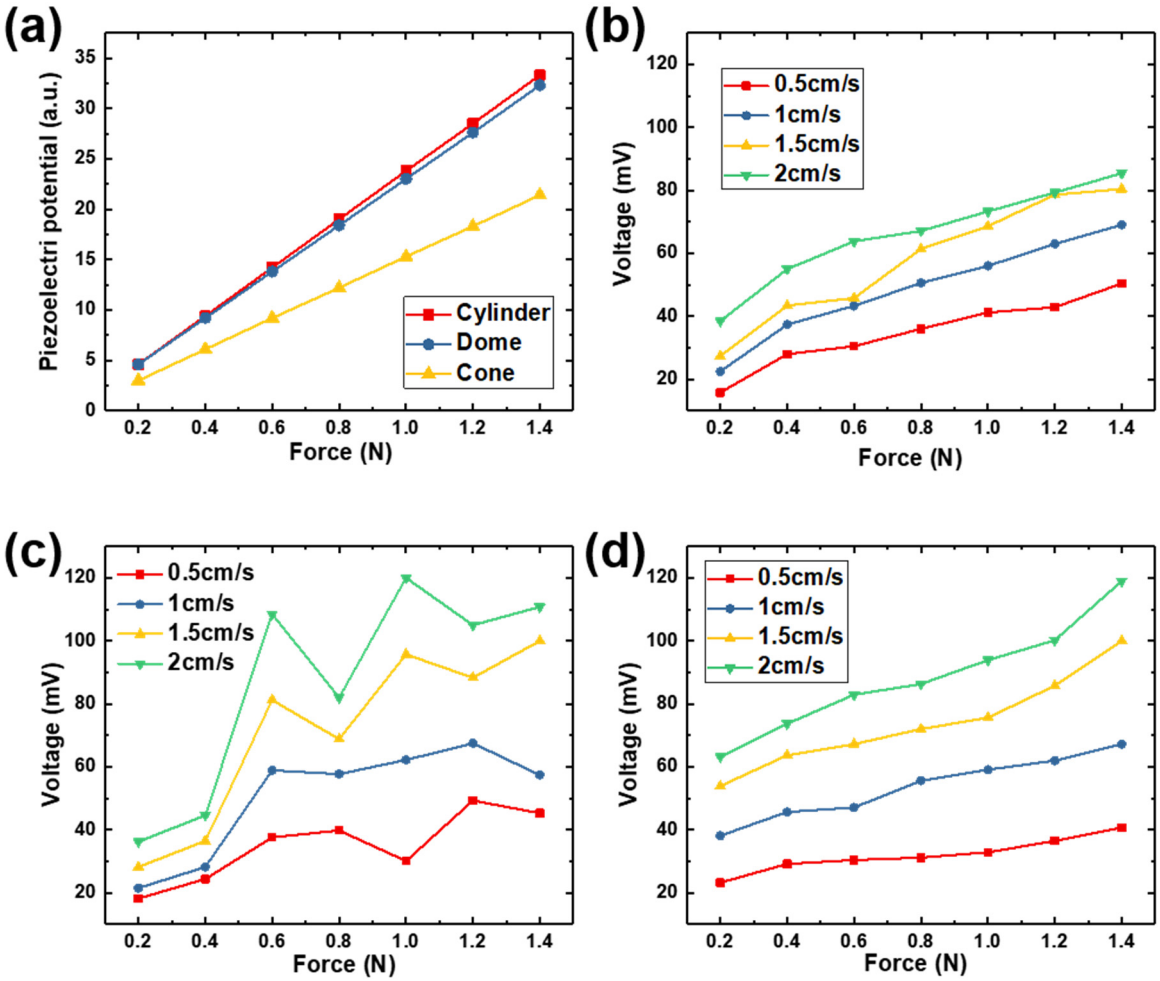

Figure 3.11. The pressure sensitivity according to the shape of dome structure, (a) simulation result, (b) cone, (c) cylinder, and (d) dome structure.

effect is poorer than other shape. The superior durability of cone shape probably results from weak interaction between the surface material and structure. However, in the case of dome structure in Figure 3.11(d), the durability and linear pressure sensitivity are satisfied simultaneously.

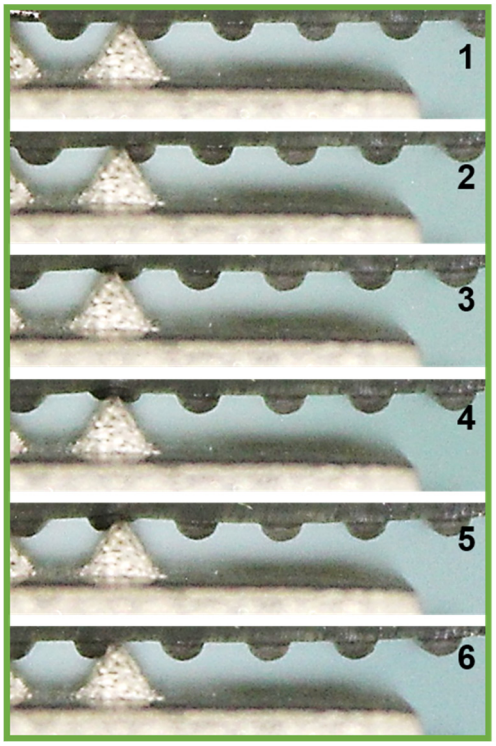

Figure 3.12. 6 images at moment when the surface materials and dome structure is interacted each other.

3.6. Simulation and Experimental result of the sensitivity enhancement effect by dome structure

In this study, a polydimethylsiloxane (PDMS) dome structure of 500um height is mainly installed on top of the tactile sensor to amplify the piezoelectric signal and thereby obtain more precise information regarding the material surface. Therefore, various experiment and result to confirm the amplifying effect of dome structure is demonstrated in following. The six images in Figure 3.12, show the tactile sensor sliding across a pyramidal object. As shown in these figures, the dome is deformed, and transferred the applied force well to the piezoelectric sensing cell when the surface structure of the tactile material contacted the dome structure. Then, basic electric characteristics is demonstrated in Figure 3.13. The sensor system can measure dynamic stimuli, such as high-frequency signals arising

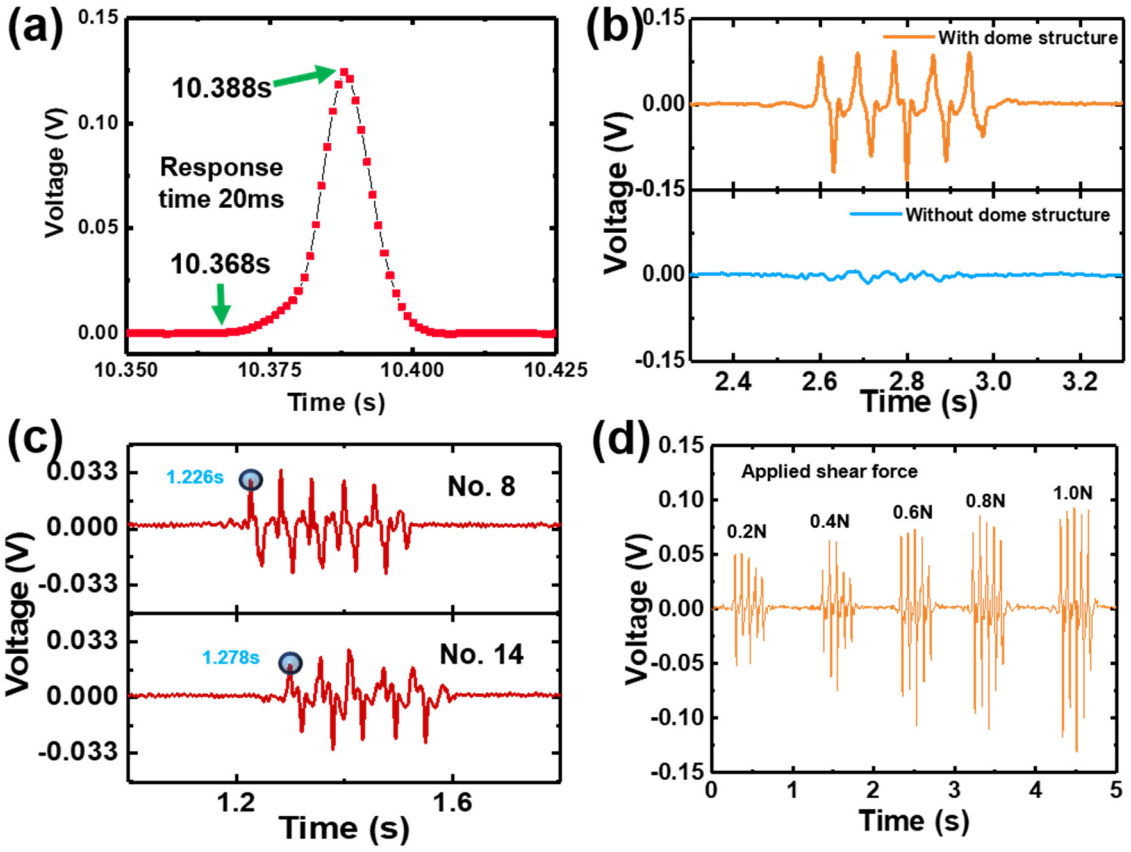

Figure 3.13. The electrical characteristics of tactile sensor (a) response time, (b) the piezoelectric voltage with and without dome structure (c) the (d) the pressure-sensitive piezoelectric voltage.

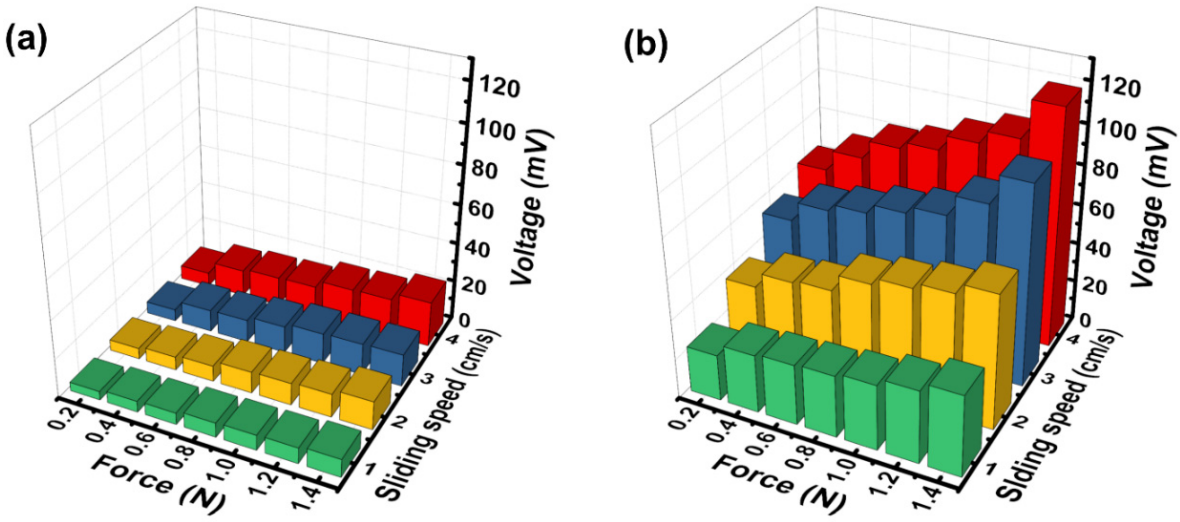

Figure 3.14. The pressure and speed sensitivity of tactile sensor (a) with, (b) without dome structure

from sliding, and has a fast response time of 20 ms in Figure 3.13(a). The different initial piezoelectric signals for the simple planar sensor structure and the sensor with the dome structure are measured in Figure 3.13(b). This result indicates clearly the signal amplifying effect of dome structure.

The sliding velocity is another important surface parameter because velocity sensing is a problem with other sensors. Figure 3.13(c) shows the piezoelectric signals arising from two seriate sensor cells (No. 8 and No. 14 cell in Figure 3.7(b)) as the sensor slid across a fabric. The multiarray structure of the sensor could readily determine the sliding velocity based on the measured piezoelectric signal without any speedometer. Therefore, our sensor could obtain surface information regardless of the various sliding velocities. Because the sliding direction and pitch of the sensor cells were fixed, the velocity could be calculated from the piezoelectric signal of each cell. For example, in Figure 3.13(c), the time interval between two peaks is 0.052 s and the moving distance is 2 mm. The calculated velocity is then 3.85 cm/s, which is in good agreement with the actual velocity of the XYZ stage. Finally, in Figure 3.13(d), the increasing of piezoelectric voltage is measured by sliding stepwise across the surface of a given material with increasing applied force and the measurement method is demonstrated in Figure 3.9.

Then, to confirm the pressure and velocity sensitivity with and without dome structure, the voltage is measured increasing the sliding pressure and velocity in Figure 3.14(a) and (b). As a result, the dome structure always yielded higher voltage and sensitivity. The relationship between the applied force and piezoelectric effect is well-known. The following equation relates the piezoelectric effect to rubbing velocity:

$$Q_{piezo} = d_{piezo}F \tag{3.4}$$

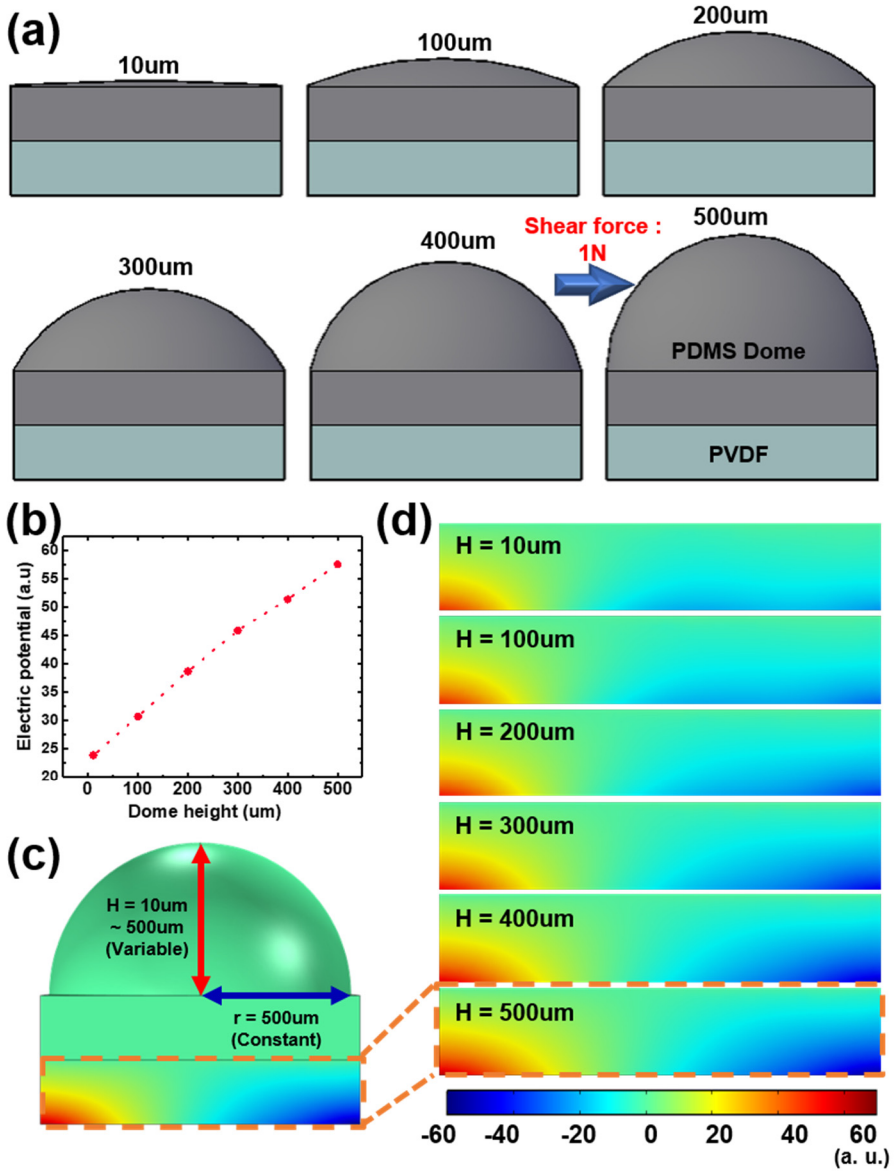

Figure 3.15. The simulation results according to the variation of dome height. (a) CAD design used for the simulation, (b) the increasing piezoelectric potential with the increase of dome height, and (c) overall structure of simulation result when the shear force of 1N is applied and (d) the magnitude image of P(VDF-TrFE) region.

$$I_{piezo} = {dQ_{piezo}}/{dt} = {d\left(d_{piezo}F\right)}/{dt} \tag{3.5}$$

$$V_{piezo} = I_{piezo}R_{external} \tag{3.6}$$

where Q_{piezo}, I_{piezo}, d_{piezo}, V_{piezo}, F and $R_{external}$ represent the piezoelectric charge, current, coefficient, voltage, applied force and external resistance, respectively. According to

the equation, the piezoelectric effect is proportional to the applied force and the time interval thereof, such that a larger piezoelectric effect is generated for shorter times for a given force.

The simulation results shown in Figure 3.15 also illustrate the role of the dome structure. To simulate the similar situation, we designed the dome structure having different height (10um, 100um, 200um, 300um, 400um, 500um) and PVDF layer like Figure 3.15(a). The radius of dome structure is constant (500um). The case of 10um height was also designed to simulate the case without dome structure because the shear force couldn't be applied to the tactile sensor and the PVDF layer didn't generate the piezoelectric polarization if the structure is perfectly flat. Then, the shear (lateral) force of 1N (the arrow direction of following figure) is applied to all case because the force is measured by load cells in sliding material at real situation. As a result, from the simulation, the higher dome structure, the higher piezoelectric polarization or potential and the amplifying effect are observed in Figure 3.15(b) to (d). In addition, to experimentally prove the simulation result, the dome structure having different height is fabricated by PDMS solution and 3d printed mold in Figure 3.16. The height from 100 um to 500um at intervals of 100um is chosen to match the cases of simulation design in Figure 3.15. After applying these structures to the tactile sensor, the voltage is measured by changing the force level (0.2N to 1.4N) and sliding velocity (0.5 to 2 cm/s). Although the experiment using the domes structure of 100 um height is also conducted, the results is not attached because the dome height is too low to generate enough piezoelectric voltage. From 200 um case, the meaningful result is observed in Figure 3.17 (a) to (d). In all cases, the measured voltage is linearly increased according to the increase of the pressure and sliding velocity. As a result, the experimental results also show that the higher height of dome structure is, the superior conversion efficiency between shear and normal force is generated similar to the simulation result in Figure 3.15.

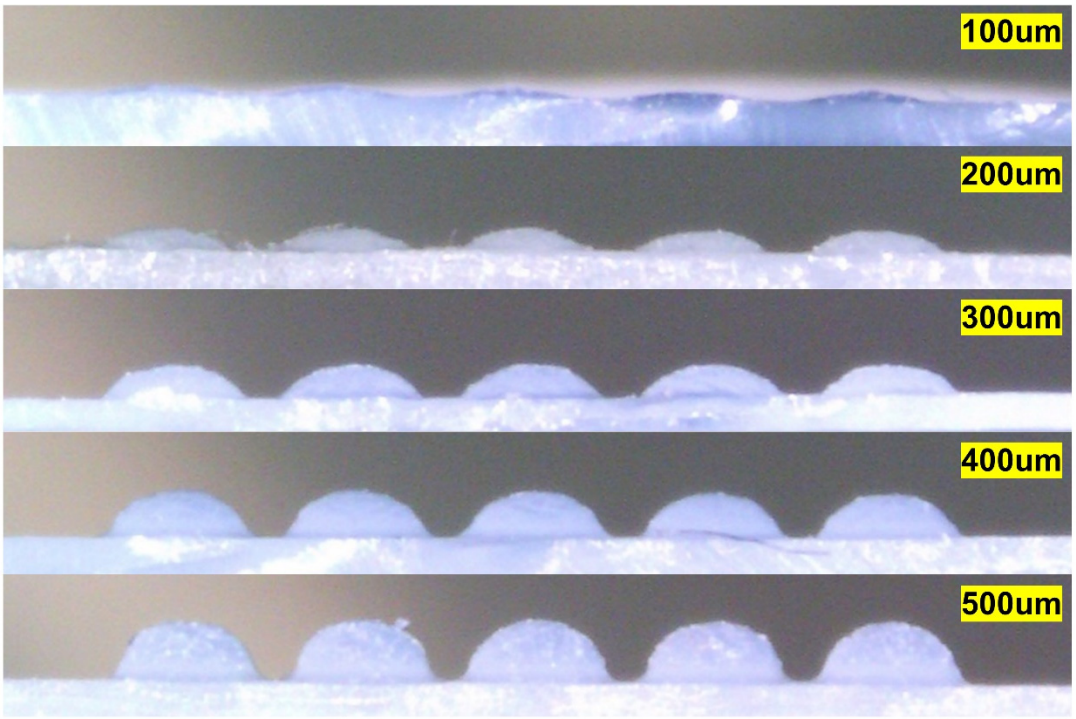

Figure 3.16. The image of dome structure having various height (100 um to 500 um)

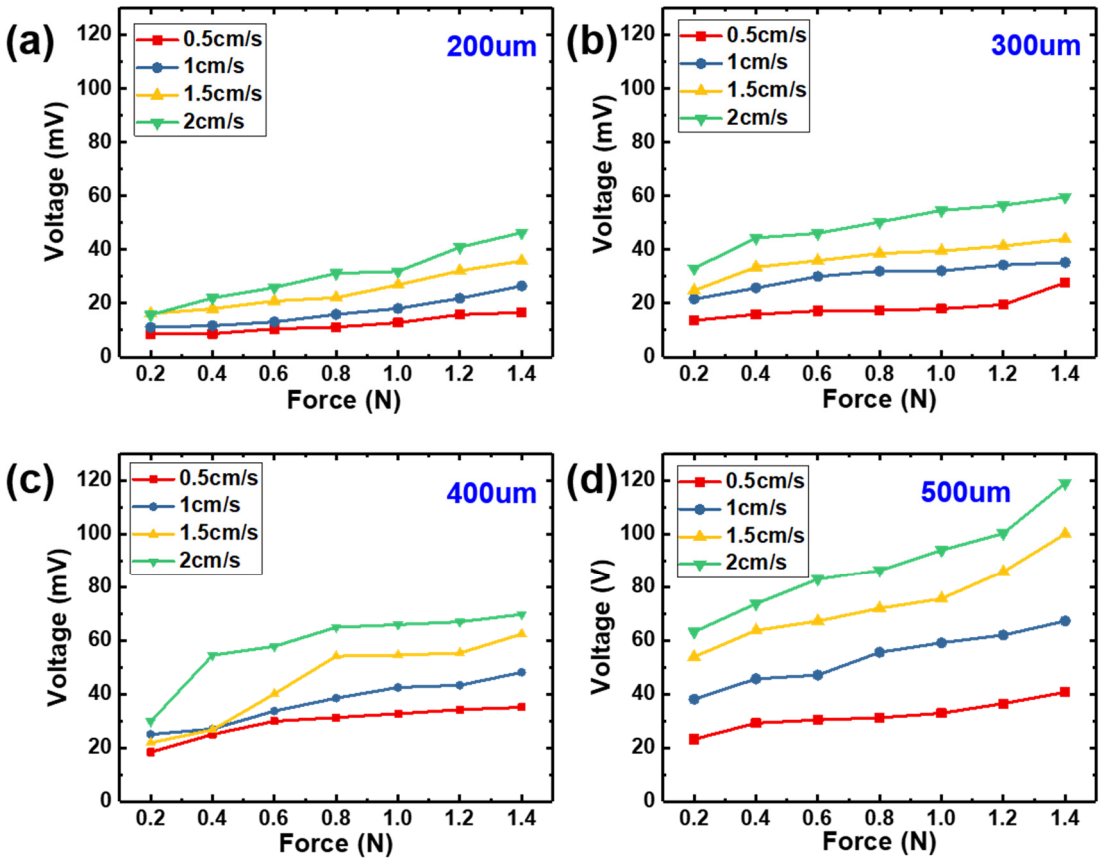

Figure 3.17. The voltage sensitivity by the variation of pressure and speed. The dome height is (a) 200um, (b) 300um, (c) 400um, (d) 500um respectively.

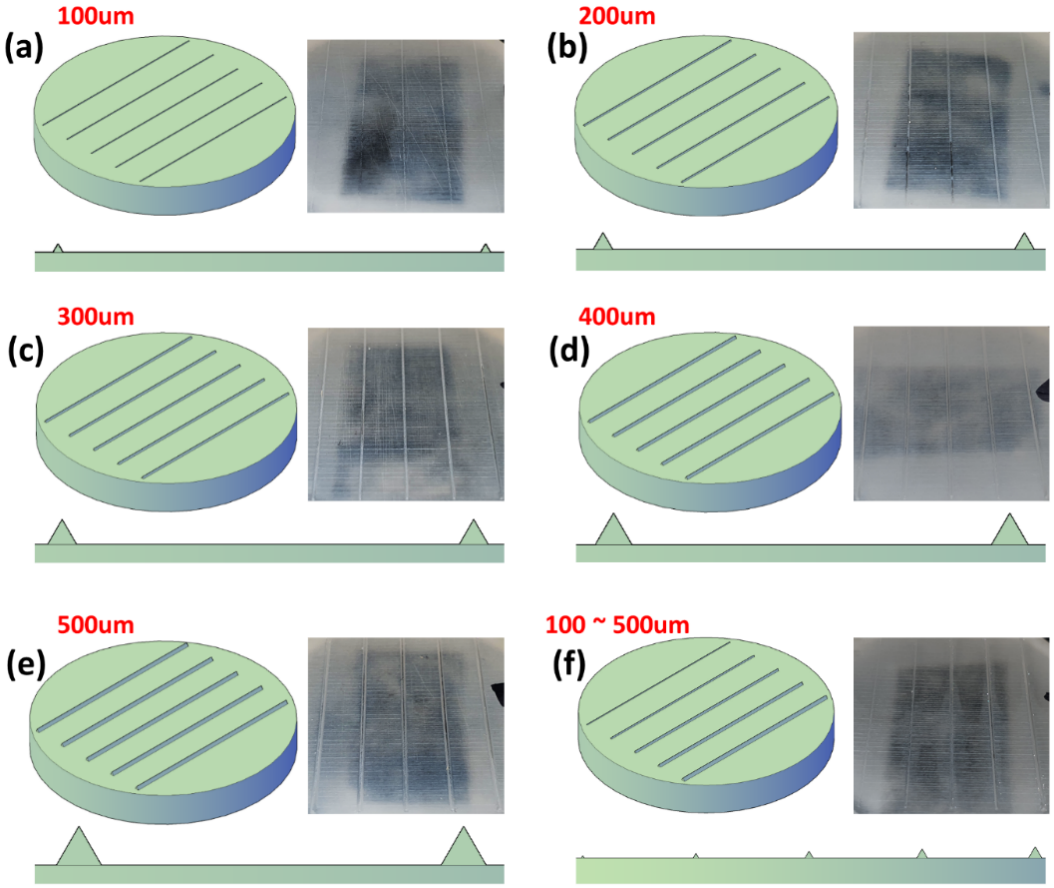

Figure 3.18. CAD design and the image of 3D printed triangle structure for depth cognition test, (a) 100um, (b) 200um, (c) 300um, (d) 400um, (e) 500um, and (f) 100 to 500um at intervals of 100um.

3.7 Depth measurement by tactile sensor with dome structure

The experiment to confirm the depth cognition ability of the tactile sensor with dome structure is carried out. Figure 3.18 shows CAD design and the image of printed structure. Because the height of dome structure used for the test is 500um, theoretically, the tactile sensor can measure the depth profile under 500um. Therefore, the height of triangle structure is fabricated up to 500um at intervals of 100um by 3D printer. The measurement is proceeded following process. The printed structure is attached to the XYZ moving equipment and the distance between the structure and dome is minimalized to precisely measure the height of structure only like Figure 3.9(c). Then, when the moving equipment is moved with

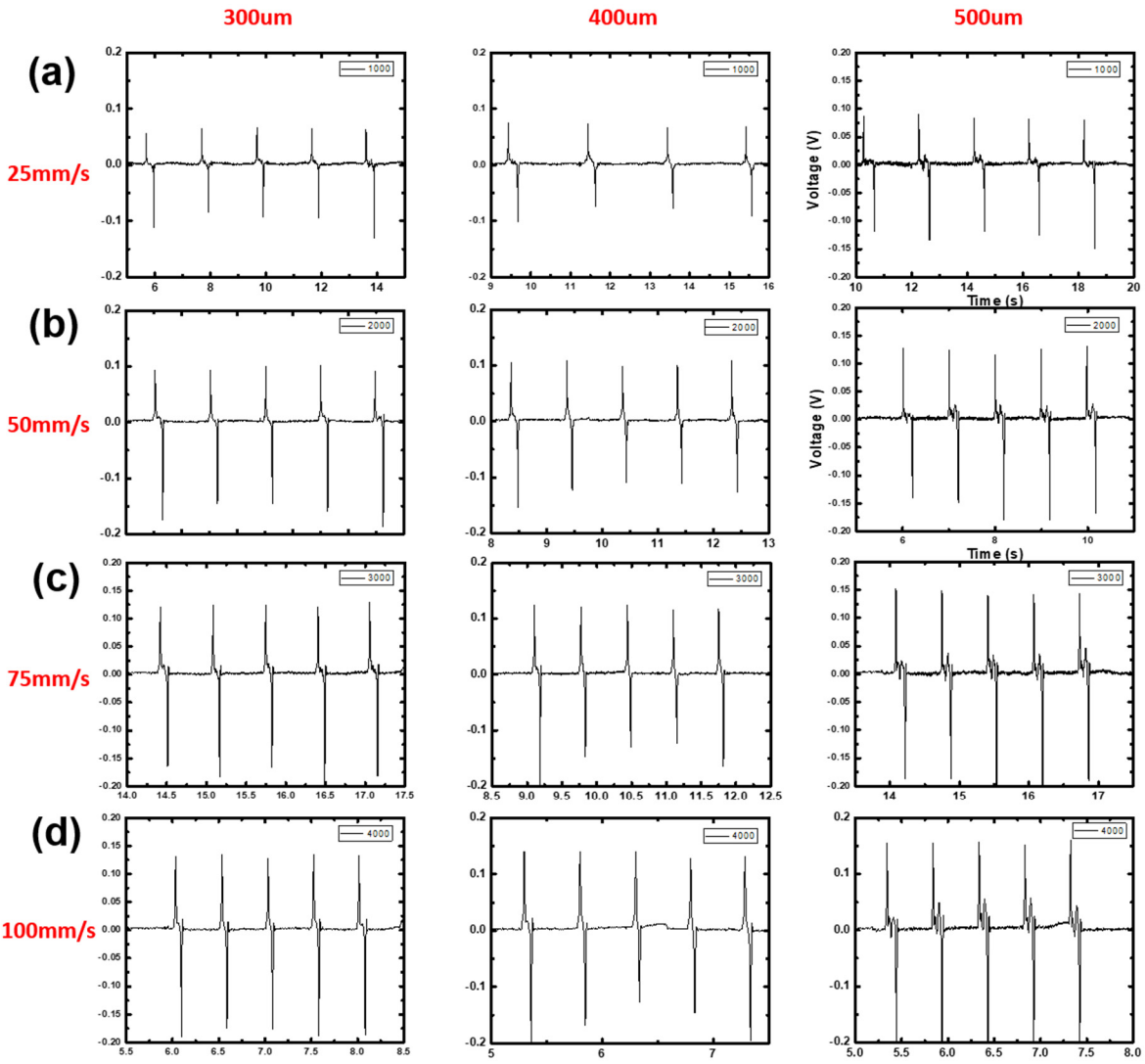

Figure 3.19. The measurement voltage by different height and sliding velocity.

various speed condition (2.5 mm/s, 5 mm/s 7.5 mm/s, 10 mm/s), at that time, the shear force generated by the interaction between the structure and dome is applied to the dome and the dome structure converts the shear force to normal force. The piezoelectric effect according to various condition is measured in Figure 3.19. Because the piezoelectric voltages of the cases of 100 um and 200 um are too small, the results are excluded. The measured voltage and integral value of each condition are presented in Figure 3.20. When the measured parameter is the piezoelectric voltage, the results in Figure 3.20(a) and (b) are linearly increased whether the variable is the depth or sliding speed. This means that the piezoelectric

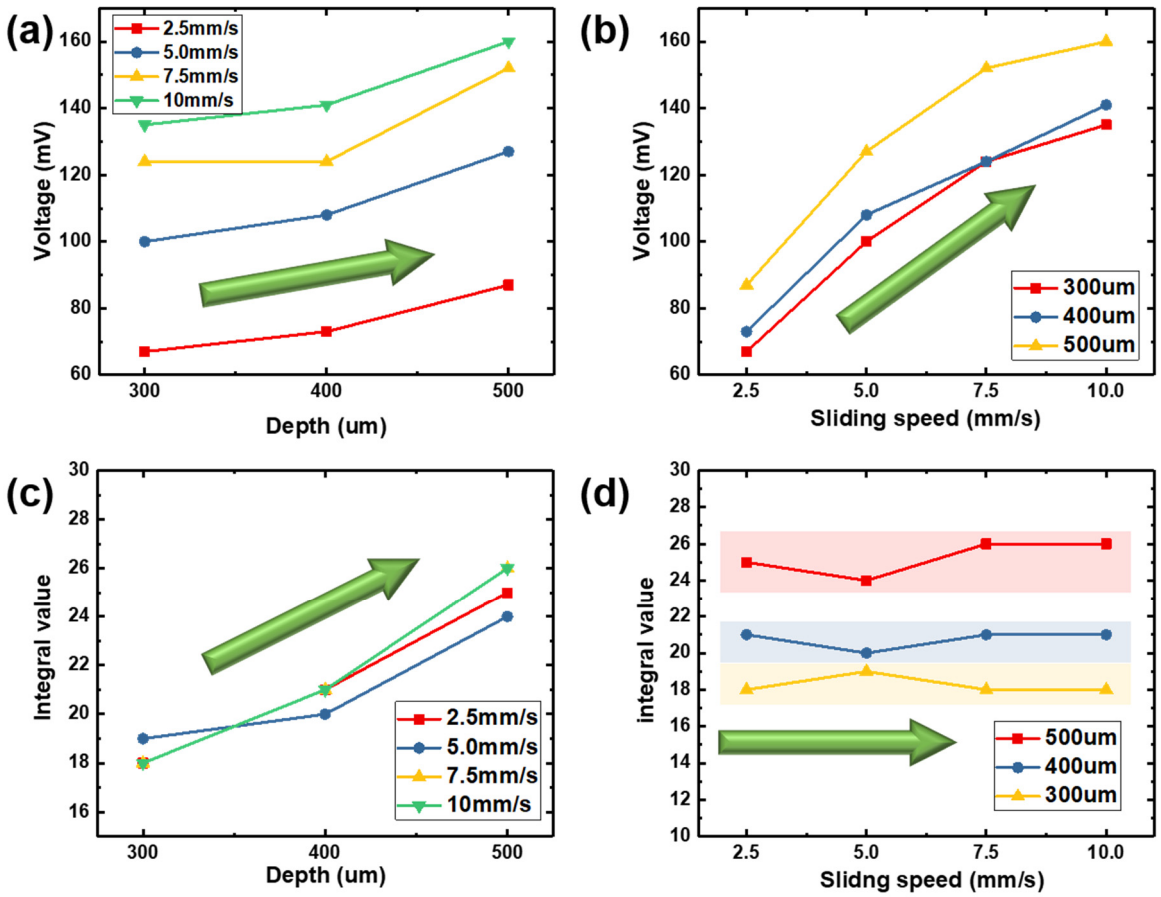

Figure 3.20. The increasing piezoelectric according to (a) the depth and (b) sliding speed and integral value according to (a) the depth and (b) sliding speed.

voltage is affected by the depth and sliding speed, simultaneously and the depth can't be distinguished by the piezoelectric voltage. However, if the piezoelectric voltage is integrated to the form of the piezoelectric charge, the different relationship between the integral value and other parameters is observed in Figure 3.20(c) and(d). The integral value is increased according to the variation of depth in Figure 3.20(c). However, the sliding speed does not affect the integral value of piezoelectric voltage like Figure 3.20(d). Therefore, this means that the integral value is only affected by the variation of depth. Additionally, to limit the unknown variable, the triangle structure having different height is printed on one substrate like Figure 3.18(f) and the top image of Figure 3.21. Then, the similar test is carried out.

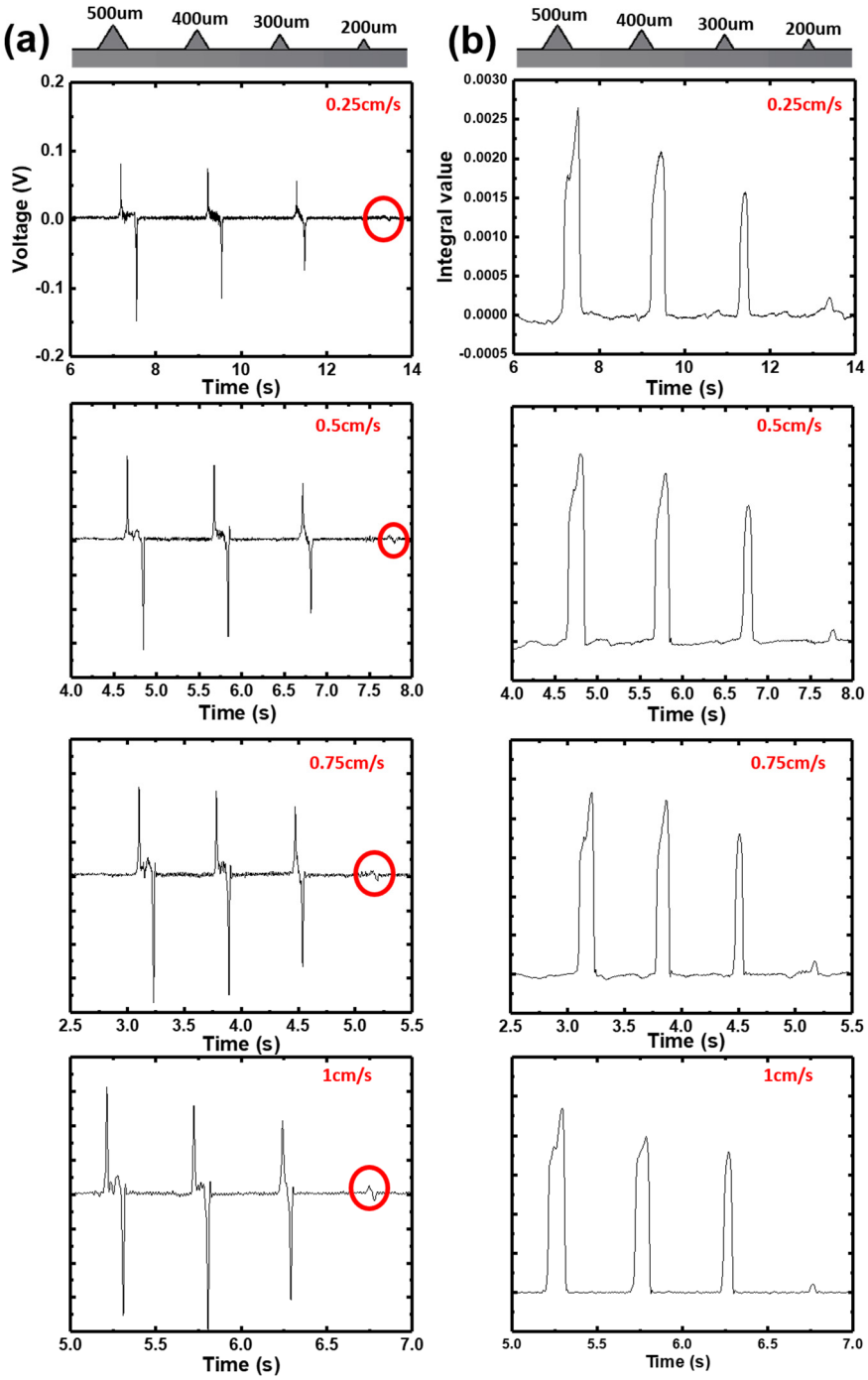

Figure 3.21. The voltage and integral value of depth cognition test

The result is similar to previous case. In this case, the piezoelectric voltage by 200 um height is observed but the level is still too low. The measured voltage and integral value for each condition are presented in Figure 3.21. This result in Figure 3.22 indicates and also supports the fact that the integral value is only affected by the variation of depth even in limited situation.

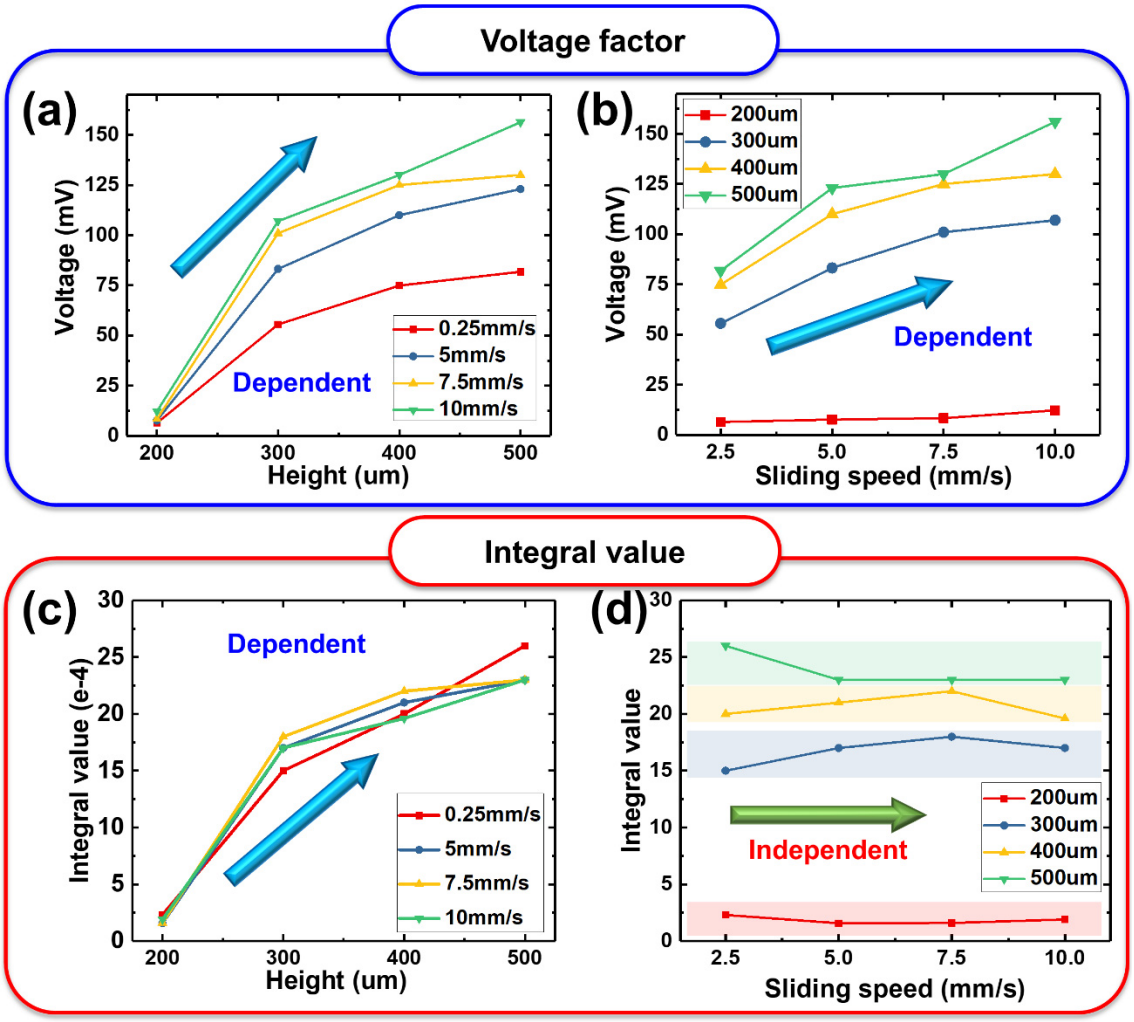

Figure 3.22. The variation tendency of the voltage and integral value by depth test

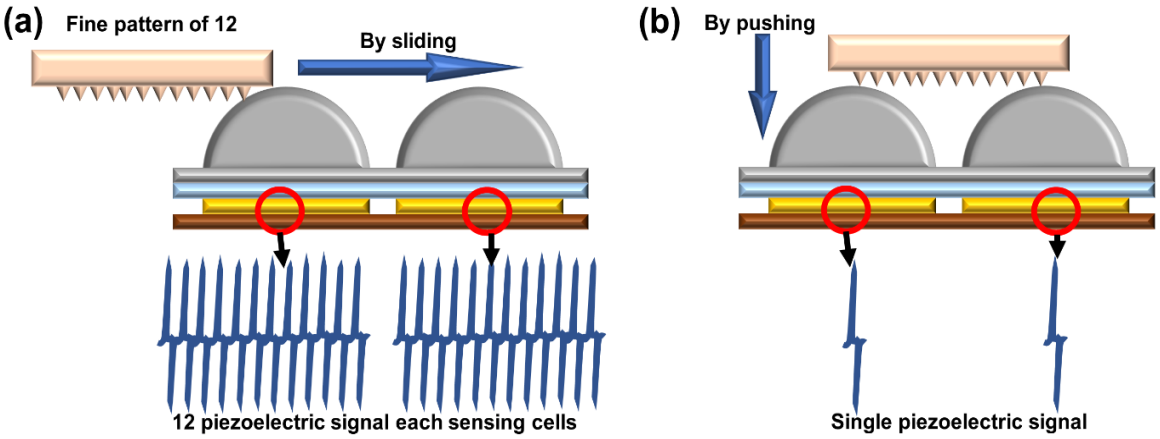

Figure 3.23. The principle to measure the fine pattern by sliding the materials

3.8. Pattern of pitch by multi-array tactile sensor with dome structure

In Figure 3.23, the principle to measure fine pitch by the sensor of 2mm pitch is demonstrated. If the fabric sample is touched by the sensing unit of tactile sensor along the normal direction, the fine pitch cannot be distinguished like Figure 3.23(b). However, because the voltage in Figure 3.23(a) is measured by sliding motion the fine pitch can be distinguished like following figure even if the size of sensing unit is 1mm. Ideally, due to sliding motion, there is no resolution limit to the sliding direction.

Human beings require physical information, especially concerning surface topography and hardness, to distinguish between smooth/soft and rough materials. The relationship between the characteristics of material and the measured piezoelectric signal during sliding across a tactile material is investigated. Figure 3.24(a) and (c) show the surface images of two different fabrics. The fabric in (a) has a specific pattern, shown clearly in the inset. The pitch pattern of (a) along the sliding direction is about 400 μm obtained by microscopy. When the tactile sensing system slid across the surface of (a), complex piezoelectric signals are obtained (Figure 3.24(b)). The signals are obtained during touching and sliding according to touching, sliding, and releasing stages. In this study, the touching and sliding signals are used in the analysis of surface information. The pitch is readily obtained from the sliding signal. The time interval between the measured piezoelectric signals is approximately 0.01 s (the lower image of Figure 3.24(b)). The surface pattern pitch can be calculated by multiplying the velocity by the time interval. Because a sliding velocity of ~ 4 cm/s is calculated by signals and the design factors of the sensor, the pitch of sample in Figure 3.24(a) is about 400 μm (4 cm/s × 0.01 s). This value is in good agreement with the measured pitch. Figure 3.24(c) and (d) show other examples of pitch calculation. The surface of sample in Figure 3.24(c) has a check pattern: the pitch is about 4 mm and the calculated value (1.92 cm) is

almost identical to the actual value. The small difference (~ 0.08 mm) is caused by the softness of the fabric material of sample. Thus, when the tactile sensor slid across the surface of the sample, the surface is easily deformed by shear and normal forces because of the softness. Notably, this deformation results in only a very small mismatch between the calculated and real value. Furthermore, the time interval of the sliding process (0.48 s) is very close to the real value (0.5 s).

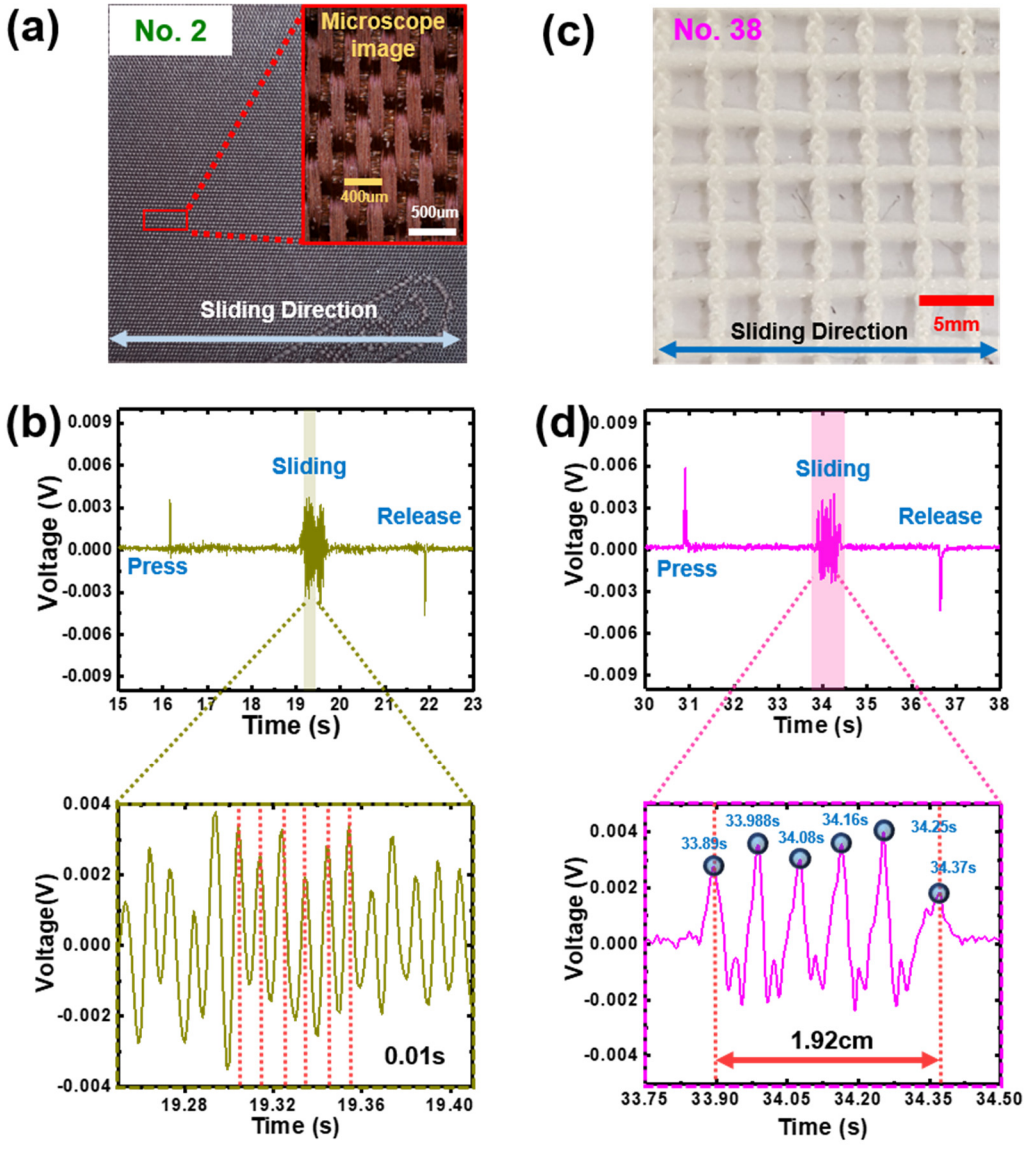

Figure 3.24. The measurement of the pitch of fabric samples (a) the fabric sample having the pitch of 400um and (b) the measured piezoelectric effect by rubbing, (b) the fabric sample having the pitch of 4mm and (b) the measured piezoelectric effect by rubbing.

(a)

(b)

(c)

	1	2	3	4	5	6	7	8	9	10	11	12	13	14	15	16	17	18	19	20	21
Group 1 (20 ~ 40)																					
Group 2 (40 ~ 50)	43	68	58.7	54	42	48	58.3	29.4	85.1	42.5	41.4	38.5	40	47.5	62.6	48.1	60.7	55.1	42.2	36.7	47.5
Group 3 (50 ~ 60)																					
Group 4 (60 ~ 70)	22	23	24	25	26	27	28	29	30	31	32	33	34	35	36	37	38	39	40	41	42
Group 5 (70 ~) : 9																					
	50.2	52.9	30	38.7	43.2	33.3	37.4	58.8	34.1	61.9	56.1	63.1	47.2	58.3	20.5	46.6	54.1	34.4	42.2	23.3	38.2

Figure 3.25. (a) 42 fabric materials and (b) commercial durometer used for the hardness measurement, and (c) the measured hardness of 42 materials by commercial durometer and categorized in five groups

3.9 Hardness measurement by the tactile sensor with dome structure

The tactile sensor with dome structure should also measure the material hardness because this is one of the various parameters determining the texture feeling of material. Therefore, the modeling and method for the hardness measurement are also proposed. First, following equations demonstrate simple modeling explaining the hardness measurement mechanism.

$$\mathrm{F} = k_t x_t = k_1 x_1 = k_2 x_2 \tag{3.7}$$

$$x_t = \frac{F}{k_t}, \quad x_1 = \frac{F}{k_1}, \quad x_2 = \frac{F}{k_2} \tag{3.8}$$

$$x_t = x_1 + x_2 \tag{3.9}$$

$$\frac{F}{k_t} = \frac{F}{k_1} + \frac{F}{k_2} \tag{3.10}$$

$$\frac{1}{k_t} = \frac{1}{k_2} + \frac{1}{k_3} \tag{3.11}$$

$$\therefore k_t = \frac{k_1 k_2}{k_1 + k_2} \tag{3.12}$$

Here, k_1 and k_2 are the spring constant of PDMS and measured materials, respectively. k_t is the total spring constant in measuring the hardness. Therefore, the total spring constant is affected and determined by measured materials because the spring constant is constant in measurement setup. This means that the total compressed distance x_t is increased or decreased by the value of k_t because the force is constant in measuring the hardness. The relationship between the spring constant and the piezoelectric effect of tactile sensor is demonstrated in following equation.

$$I_{piezo} = \frac{dq}{dt} = d_{33}\frac{dF}{dt} = d_{33}k_t\frac{dx_t}{dt} = d_{33}\frac{(k_1 k_2)}{(k_1 + k_2)}\frac{dx_t}{dt} \tag{3.13}$$

$$\therefore \quad I_{piezo} \quad \propto \quad k_t = \frac{k_1 k_2}{k_1 + k_2} \tag{3.14}$$

To measure the material hardness using our tactile sensor, 42 fabric materials in Figure 3.25(a) having different hardness are used. To measure and compare the materials hardness, the hardness value of 5 materials value is measured by commercialized durometer in Figure 3.25(b) and we obtain the piezoelectric effect by pressing like this Figure. Generally, the piezoelectric effect is generated through 2 steps like Figure 3.26(a). The first slope is related to material hardness and second slope reflect the substrate hardness. Therefore, the ratio between 1st and 2nd is determined by the thickness of samples. And because the region of first slope is proportional to thickness of prepared sample, enough thickness and slow push speed are important to determine the hardness. As a result, regardless of measured voltage level, the first slope of generated voltage is proportional to hardness level like this graph. The hardness of a fabric material is measured using a commercial durometer. The values for the 42 materials are categorized into five groups: 1: 20–40, 2: 41–50, 3: 51–60,

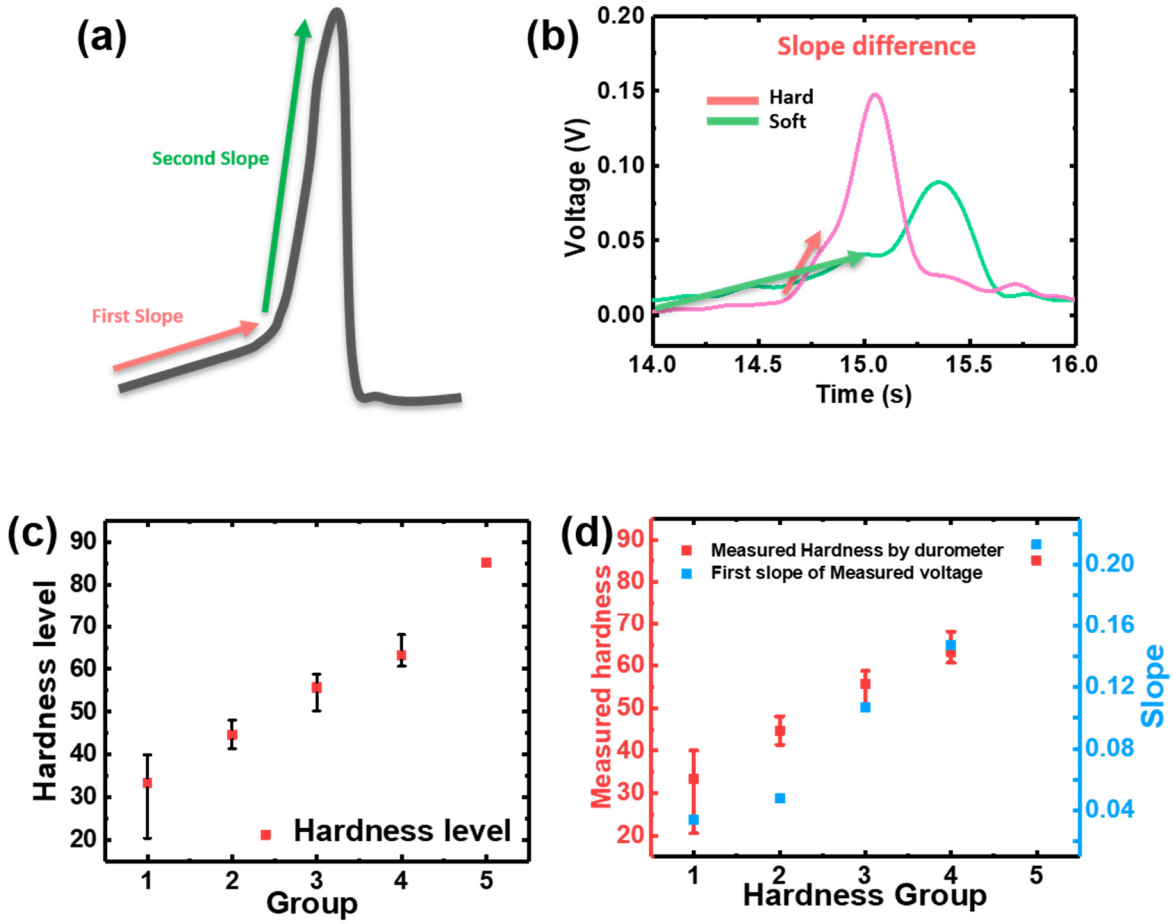

Figure 3.26. (a) The first slope and second slope of the piezoelectric voltage, (b) the piezoelectric voltage when the fabric NO. 9 and No. 36 push the tactile sensor, (c) the categorized hardness of 42 materials, and (d) comparison the hardness measured by the durometer and piezoelectric slope.

4: 61–70, and 5: 71–90 (Figure 3.25(c) and Figure 3.26(c)). The hardness of a fabric is determined based on the piezoelectric signals. The slope of the generated piezoelectric signal differs with the hardness level; the slope of the signal in the touched state is shown in Figure 3.26(b). The durometer values of samples No. 2 and No. 38 were 85.1 and 24.9, respectively. Under the same test conditions, the harder the material, the steeper is the initial slope of the generated piezoelectric signal. The slope of the measured signal in Figure 3.26(b) shows that the hardness of fabric No. 2 is larger than that of sample No. 38, consistent with their durometer values. The measured piezoelectric slopes and durometer hardness are compared in Figure 3.26(d). Analysis revealed that the initial slope is proportional

to the durometer hardness of the fabric. Therefore, a relative hardness value can be obtained by the piezoelectric signals during the touching motion of tactile sensor.

In this chapter, the novel structure based on PDMS to measure the surface information is suggested. This structure plays an important role of the fingerprint of human skin. To find optimized structure, three shape (cone, cylinder and dome) are applied to the tactile sensor and the FEM simulation supports the experimental result. Additionally, the amplifying effect according to the height of dome structure is also investigated. As a result, our tactile sensor with optimized dome structure shows the superior performance such as high shear force sensitivity, fast response time, stability, and durability and so on. Specially, the high sensitivity about the shear force enables the tactile sensor to measure the various surface information such as the depth, pitch of pattern, hardness and so on. Therefore, in the future, we expect that this research will be fundamental study for the tactile sensor detecting the surface roughness and applied to the various applications such as the artificial electronic skin, touch panel, wearable device health care applications and so on.

3.10 Reference

[1] Wan, Y., Qiu, Z., Hong, Y., Wang, Y., Zhang, J., Liu, Q., Wu, Z., and Guo, C. F. "A Highly Sensitive Flexible Capacitive Tactile Sensor with Sparse and High-Aspect-Ratio Microstructures", Advanced Electronic Materials, 4(4), 2018, 1700586.

[2] Zhu, B., Niu, Z., Wang, H., Leow, W. R., Wang, H., Li, Y., Zheng, L., Wei, J., Huo, F and Chen, X. "Microstructured graphene arrays for highly sensitive flexible tactile sensors", Small, 10(18), 2014, pp. 3625-3631.

[3] Zhu, G., Yang, W. Q., Zhang, T., Jing, Q., Chen, J., Zhou, Y. S., Bai, Peng., and Wang, Z. L. "Self-powered, ultrasensitive, flexible tactile sensors based on contact electrification", Nano letters, 14(6), 2014, pp. 3208-3213.

[4] Rasel, M. S., Maharjan, P., Salauddin, M., Rahman, M. T., Cho, H. O., Kim, J. W., and Park, J. Y. "An impedance tunable and highly efficient triboelectric nanogenerator for large-scale, ultra-sensitive pressure sensing applications", Nano Energy, 49, 2018, pp. 603-613.

[5] Yeo, J. C., Yu, J., Loh, K. P., Wang, Z., and Lim, C. T. "Triple-state liquid-based microfluidic tactile sensor with high flexibility, durability, and sensitivity", Acs Sensors, 1(5), 2016, pp.543-551.

[6] Lee, D., Lee, H., Jeong, Y., Ahn, Y., Nam, G., and Lee, Y. "Highly Sensitive, Transparent, and Durable Pressure Sensors Based on Sea-Urchin Shaped Metal Nanoparticles. Advanced Materials, 28(42), 216, pp.9364-9369.

[7] Chun, S., Son, W., Kim, H., Lim, S. K., Pang, C., and Choi, C. "Self-powered pressure- and vibration-sensitive tactile sensors for learning technique-based neural finger skin" Nano letters, 19(5), 2019, pp. 3305-3312.

[8] Yi, Z., Zhang, Y., and Peters, J. "Bioinspired tactile sensor for surface roughness discrimination", Sensors and Actuators A: Physical, 255, 2017, pp. 46-53.

[9] Zou, L., Ge, C., Wang, Z. J., Cretu, E., and Li, X. "Novel tactile sensor technology and smart tactile sensing systems: A review", Sensors, 17(11), 2017, 2653.

[10] Kroemer, O., Lampert, C. H., and Peters, J. "Learning dynamic tactile sensing with

robust vision-based training", IEEE transactions on robotics, 27(3), 2011, pp. 545-557.

[11] Spiers, A. J., Liarokapis, M. V., Calli, B., and Dollar, A. M. "Single-grasp object classification and feature extraction with simple robot hands and tactile sensors", IEEE transactions on haptics, 9(2), 2016, pp. 207-220.

[12] Sohn, K. S., Chung, J., Cho, M. Y., Timilsina, S., Park, W. B., Pyo, M., Shin, N., Sohn, K., and Kim, J. S. "An extremely simple macroscale electronic skin realized by deep machine learning", Scientific reports, 7(1), 2017, pp. 1-10.

[13] Gandarias, J. M., Garcia-Cerezo, A. J., and Gomez-de-Gabriel, J. M. "CNN-based methods for object recognition with high-resolution tactile sensors", IEEE Sensors Journal, 19(16), 2019, pp. 6872-6882.

[14] Scheibert, J., Leurent, S., Prevost, A., and Debrégeas, G., "The role of fingerprints in the coding of tactile information probed with a biomimetic sensor", Science, 323(5920), 2009, pp. 1503-1506.

[15] Cao, Y., Li, T., Gu, Y., Luo, H., Wang, S., and Zhang, T. "Fingerprint-inspired flexible tactile sensor for accurately discerning surface texture", Small, 14(16), 2018, 1703902.

[16] Harada, S., Kanao, K., Yamamoto, Y., Arie, T., Akita, S., and Takei, K. "Fully printed flexible fingerprint-like three-axis tactile and slip force and temperature sensors for artificial skin", ACS nano, 8(12), 2014, pp. 12851-12857.

[17] Chun, S., Son, W., Kim, H., Lim, S. K., Pang, C., and Choi, C. "Self-powered pressure- and vibration-sensitive tactile sensors for learning technique-based neural finger skin" Nano letters, 19(5), 2019, pp. 3305-3312.

[18] Chun, S., Kim, Y., Oh, H. S., Bae, G., and Park, W. "A highly sensitive pressure sensor using a double-layered graphene structure for tactile sensing", Nanoscale, 7(27), 2015, pp. 11652-11659.

[19] Shin, K., Kim, D., Park, H., Sim, M., Jang, H., Sohn, J. I., Cha, S. N., and Jang, J. E. "Artificial Tactile Sensor With Pin-type Module for Depth Profile and Surface Topography Detection", IEEE Transactions on Industrial Electronics, 67(1), 2019, pp. 637-646.

[20] Tichý, J., Erhart, J., Kittinger, E., and Privratska, J. “Fundamentals of piezoelectric sensorics: mechanical, dielectric, and thermo dynamical properties of piezoelectric materials”, Springer Science & Business Media, 2010.

[21] Sharma, T., Je, S. S., Gill, B., and Zhang, J. X. “Patterning piezoelectric thin film PVDF–TrFE based pressure sensor for catheter application” Sensors and Actuators A: physical, 177, 2012, pp. 87-92.

[22] Constantino, C. J. L., Job, A. E., Simoes, R. D., Giacometti, J. A., Zucolotto, V., Oliveira Jr, O. N., Gozzi, G., Chinaglia, D. L. “Phase transition in poly (vinylidene fluoride) investigated with micro-Raman spectroscopy”, Applied spectroscopy, 59(3), 2005, pp. 275-279.

[23] Li, C., Wu, P. M., Lee, S., Gorton, A., Schulz, M. J., and Ahn, C. H. “Flexible dome and bump shape piezoelectric tactile sensors using PVDF-TrFE copolymer”, Journal of Microelectromechanical Systems, 17(2), 2008, pp. 334-341.

[24] Lee, H. K., Chung, J., Chang, S. I., and Yoon, E., “Normal and shear force measurement using a flexible polymer tactile sensor with embedded multiple capacitors”, Journal of Microelectromechanical Systems, 17(4), pp. 934-942.

[25] Yu, P., Liu, W., Gu, C., Cheng, X., and Fu, X. “Flexible piezoelectric tactile sensor array for dynamic three-axis force measurement”, Sensors, 16(6), 2016, 819.

[26] Kim, M. S., Ahn, H. R., Lee, S., Kim, C., and Kim, Y. J. “A dome-shaped piezoelectric tactile sensor arrays fabricated by an air inflation technique”, Sensors and Actuators A: Physical, 212, 2014, pp. 151-158.

[27] Chun, S., Choi, Y., Suh, D. I., Bae, G. Y., Hyun, S., and Park, W. “A tactile sensor using single layer graphene for surface texture recognition”, Nanoscale, 9(29), 2014, pp. 10248-10255.

[28] Chen, X., Shao, J., Tian, H., Li, X., Tian, Y., and Wang, C., “Flexible three-axial tactile sensors with microstructure-enhanced piezoelectric effect and specially-arranged piezoelectric arrays”, Smart Materials and Structures, 27(2), 2018, 025018.

[29] Chun, S., Jung, H., Choi, Y., Bae, G., Kil, J. P., and Park, W. “A tactile sensor using a graphene film formed by the reduced graphene oxide flakes and its detection of surface

morphology", Carbon, 94, 2015, pp. 982-987.

[30] Choi, D., Jang, S., Kim, J. S., Kim, H. J., Kim, D. H., and Kwon, J. Y. "A Highly Sensitive Tactile Sensor Using a Pyramid-Plug Structure for Detecting Pressure, Shear Force, and Torsion", Advanced Materials Technologies, 4(3), 2019, 1800284.

IV. ZIG-ZAG ARRAYED TACTILE SENSOR BASED ON PIEZOELECTRIC-RESISTIVE MECHANISM TO DETECT THE SURFACE TOPOGRAPHY AND TEMPERATURE

4.1. Introduction

In order to improve or alternate the human sensations, bio-mimicked applications such as artificial retina,[1-3] electronic nose,[4-6] artificial cochlear,[7,8] electronic tongue,[9,10] the tactile sensor[11,12] and so on have been considerably attracted by many researchers. Most of all, recently, the research to develop the tactile sensor similar to human touch sensation have been actively studied. To develop the human-like tactile sensor, many mechanisms are converting the external stimulus into the various signal. Especially, after the touch screen application of Apple's iPhone, the capacitive sensing mechanism has been much used in industrial fields due to their various advantage such as high sensitivity, large-area fabrication, multi-touch ability, wiring problems and so on. Even if commercialized touch applications show the excellent performance to measure and detect the pressure and pressed position, the demand for the human-like tactile device is gradually increased in the field of medical or robotic engineering. Over the current tactile applications based on the pressure sensor, the future device should detect the various stimuli such as the pressure, temperature, smooth/roughness of the surface and so on. Therefore, recently, many kinds of research to detect the pressure and temperature at the same time has been actively reported.[13-16] Then, the roughness feeling of human sensation results from the combined feeling by various surface parameters like hardness, quality of the materials, surface topography and so on. Since these parameters should be considered at the same time, it is difficult to decide the surface roughness like a human by the signal analysis from the tactile sensor. To solve these problems, other researches have combined roughness detection with machine learning. Even if

this method didn't consider complex parameters, the system should collect big data and be heavier than simple processing without machine learning. Therefore, to lighten the system, the new method analyzing the measured signal should be developed. In this study, among various parameters, we suggest 3D rendering method to restore the surface topography our tactile sensor is based on the piezoelectric effect generating the electrical voltage by external pressure or temperature change.

4.2. Device Fabrication

Since, in our previous study,[17] one cell is used to render the surface structure, repetitive sensing process should be needed to measure the piezoelectric signal for wide region. Therefore, the Zig-Zag multi array electrodes are applied to this study for reducing the number of measurement repetition and enhancing the resolution compared to matrix array electrode case. The structure of fabricated sensor is demonstrated in Fig 4.1(a). The tactile sensor consists of bottom electrode on polyimide film, P(VDF-TrFE) as the sensing materials, Au top electrode and dome structure amplifying the piezoelectric signal by converting the shear force to normal force like the fingerprint of human.

The fabrication process of Zig-Zag arrayed tactile sensors is demonstrated in Fig 4.1(a). Firstly, for thin and flexible tactile sensor, the polyimide film of 75 um was used for the substrate material. However, existing polyimide film had various defects on surface. Therefore, for the uniformity of polyimide film and removing the defects on the surface, the polyimide film was spin-coated by polyimide solution at 2000 rpm. After the spin coating, the film was exposed on UV light (200mJ/cm^2) and the coated film was placed for 1 hour in convection oven at 190 ℃. Then, A 2×5 Zig-Zag electrode and a temperature sensing part between electrodes were patterned on a substrate by photolithography;

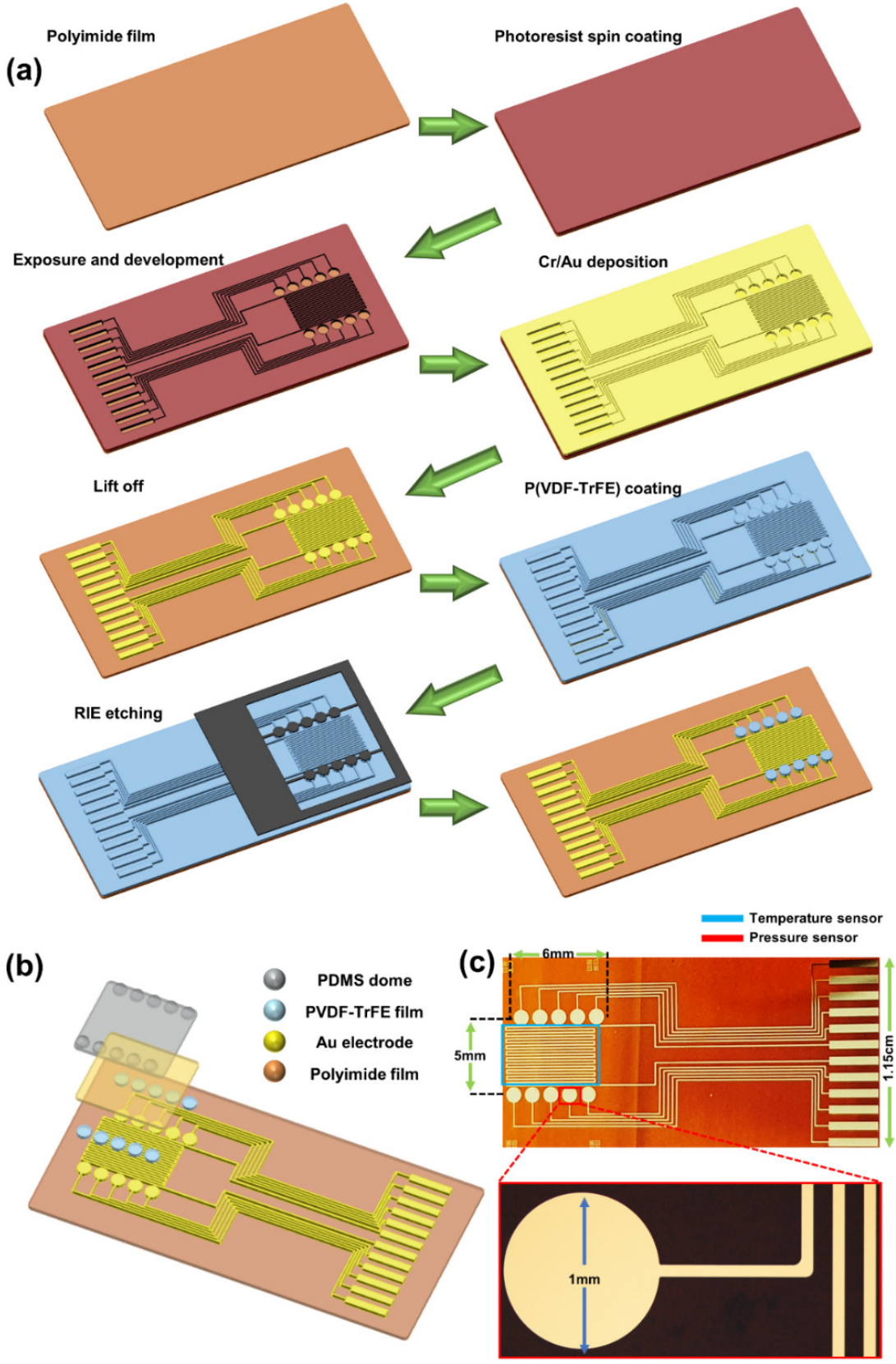

Figure 4.1. The schematic of fabrication process of Zig-Zag tactile sensor and fabricated sensor.

since the dome structure was applied on each sensing cells, the sensing cells of the circle shape was designed circle and the diameter of cells was 1mm. The fabrication process of dome structure was demonstrated in previous chapter. A Cr/Au(10nm/100nm) layer was deposited by using a radio frequency magnetron sputtering. Then, the deposited metal layer was removed by a lift off process. As the sensing materials, the P(VDF-TrFE) piezoelectric film was fabricated by simple process. First, the P(VDF-TrFE) (75/25) powder of Piezotech was dissolved in 2-butanone to make a 15 wt% P(VDF-TrFE) solution. The mixture of powder and solvent was stirred at 600 rpm without heating for 2 hours to dissolve the P(VDF-TrFE) powder. After dissolving the powder, the solution was spin-coated on the Zig-Zag bottom electrode array at 3000 rpm. Finally, thermal annealing of P(VDF-TrFE) at 130°C for 2 h enabled beta-phase crystallization to enhance the piezoelectric effect. Then, to reduce the cross-talk between sensing cells, the P(VDF-TrFE) layer coated on unnecessary area is etched by RIE etching process. Finally, the Zig-Zag tactile sensor is completed by placing the common top electrode and PDMS dome structure on the sensing cells in Figure 4.1(b). Figure 4.1(c) shows the fabricated tactile sensor with Zig-Zag electrode array.

4.3. Piezoelectric characteristics of fabricated tactile sensor

After the fabrication, the piezoelectric property and the data collection for rendering was carried out following set-up. The sensing characteristics of tactile sensor was measured using a digital oscilloscope. Then, a multi-source data acquisition system (PXIE-5105; National Instruments) was used to measure the data from the Zig-Zag electrodes in sliding the surface material on the tactile sensor. The sampling rate of 1k/s was used to obtain the piezoelectric signal. Then, to remove the small fluctuation and noise signal, a low-pass filter of LabView DAQ system. The sliding velocity are fixed at 0.5, 1, 1.5 and 2 cm/s.

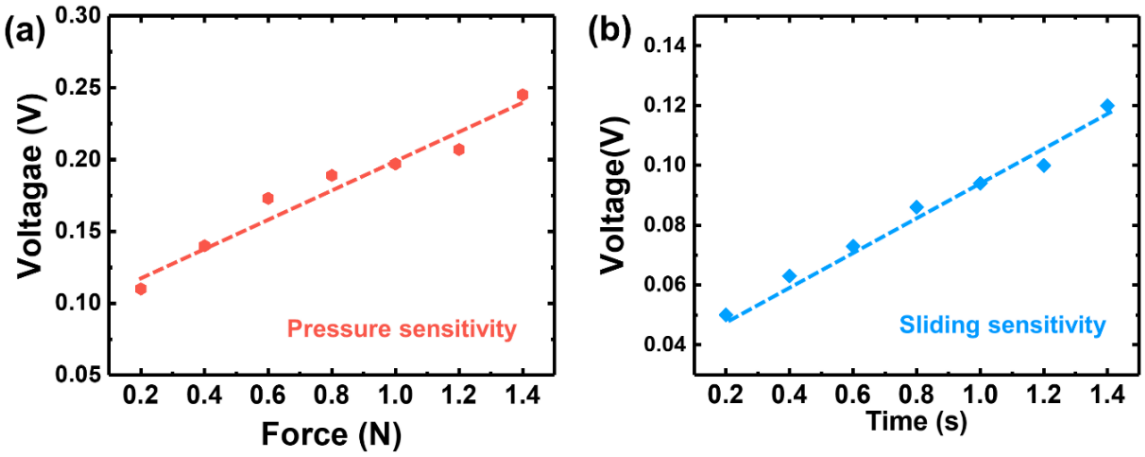

Figure 4.2. (a) The pressure and (b) sliding sensitivity of Zig-Zag arrayed tactile sensor

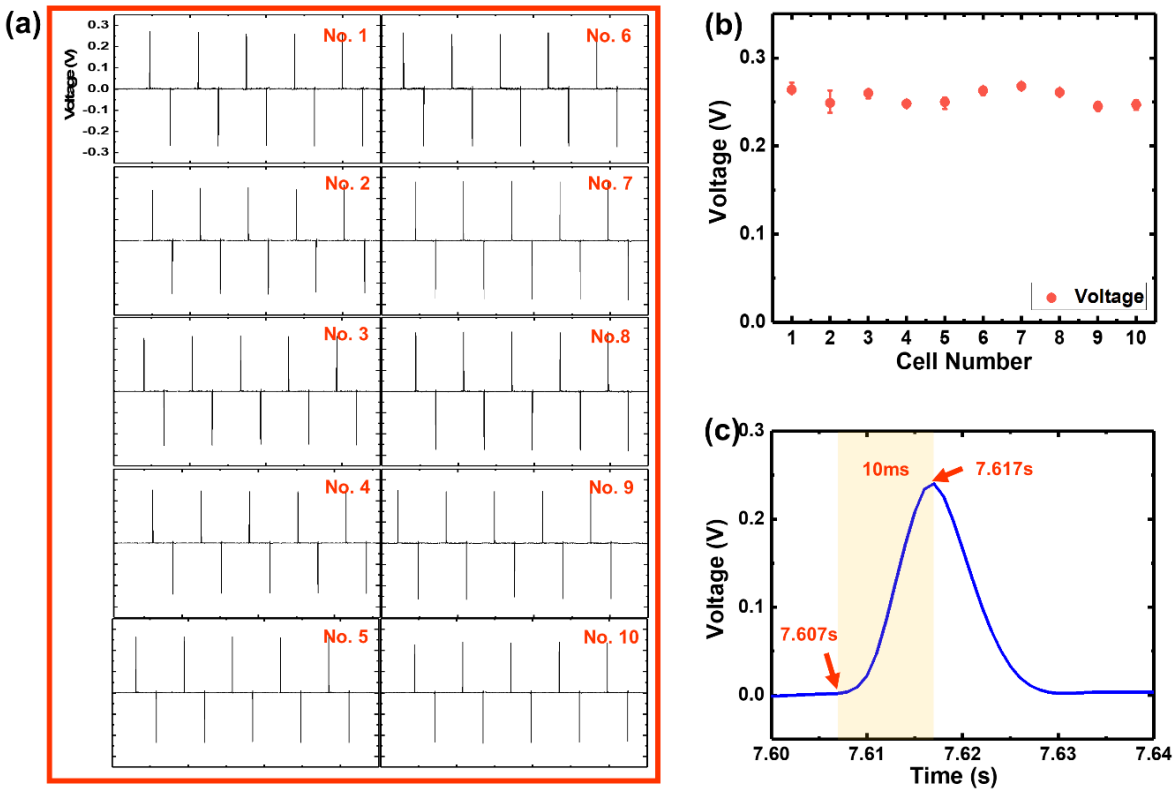

Figure 4.3. (a) The measured and (b) variation piezoelectric voltage at each cell and the response time of this sensor.

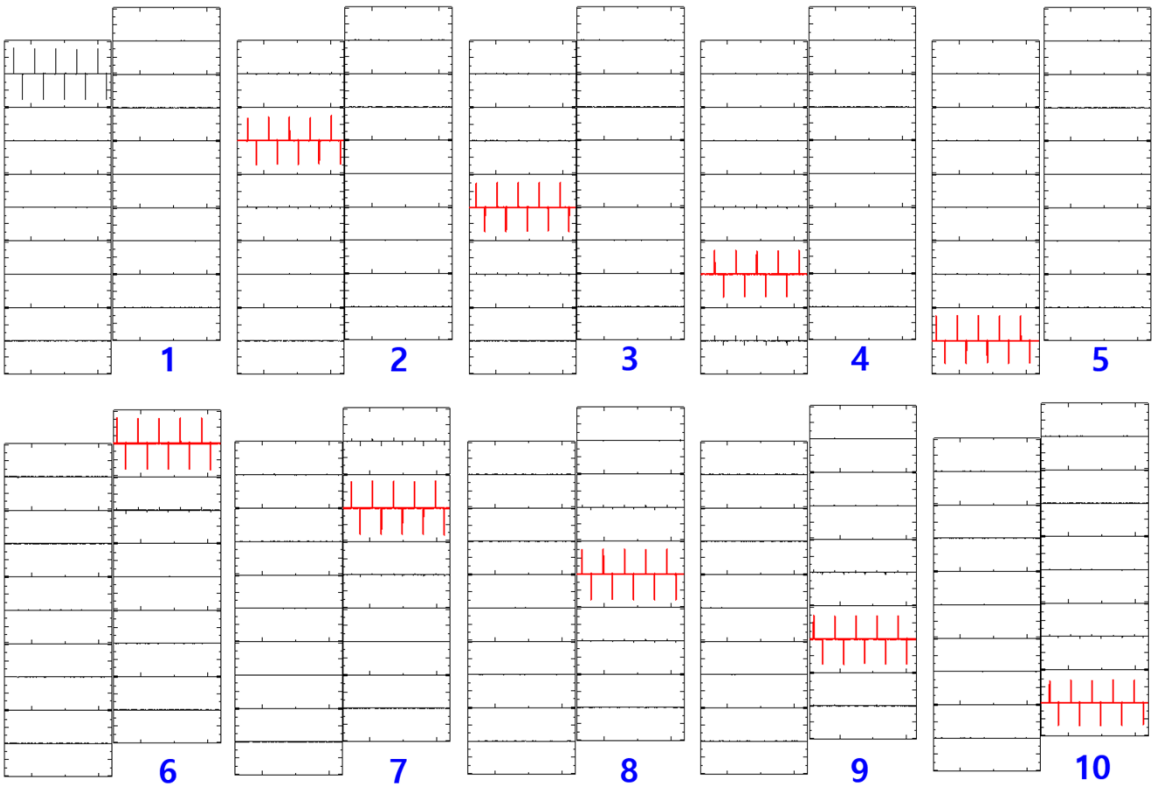

Figure 4.4. No cross-talk among 10 cells by pressing.

Then, in Figure 4.2 and 4.3, the performance and characteristics of sensor are demonstrated. Our sensor mainly consists of the piezoelectric sensing part and dome structure to amplify the piezoelectric effect by sliding. So, the sensitivities by push and sliding action were measured in Figure 4.2(a) and (b). The sensitivity by push and sliding action is about 113mV/N and 58.3mV/N respectively. The sensitivity shows the linear property with increasing the applied force. The sliding sensitivity of the tactile sensor with dome structure is higher than that of the case without dome structure because of amplifying effect of PDMS dome structure. The detail is presented at previous chapter 3.

Then, because the uniformity between cells is also one of the important factors to reconstruct the surface topography precisely, the uniformity of 10 sensing cells should be investigated. As a measured result, the measured voltages at each cell are in Figure 4.3(a) and the voltage variation of 10 sensing cells is from 246mV to 264mV at 1.4N in Figure

4.3(b) and the result shows the superior uniformity of our tactile sensor. When the surface information is obtained by the certain tactile sensor, the response time is very important to reduce the data loss because the measured signal by sliding is very dynamic. The measured response time of our sensor is about 10ms in Figure 4.3(c). Since the piezoelectric sensor is more effective to measure dynamic sensing, this value is superior to other sensors using other sensing mechanisms such as capacitive, resistive and triboelectric effect. In addition, because the stability of the certain sensor is very impossible for commercialization, the measurement of the piezoelectric effect during 3000 cycles is carried out in Figure 4.5. From the result, the uniform voltage is generated during 3000 cycles at the pressure of 1.0N. The first image in red box is the first 50 signals, and the second image in blue box is the last 50 signals.

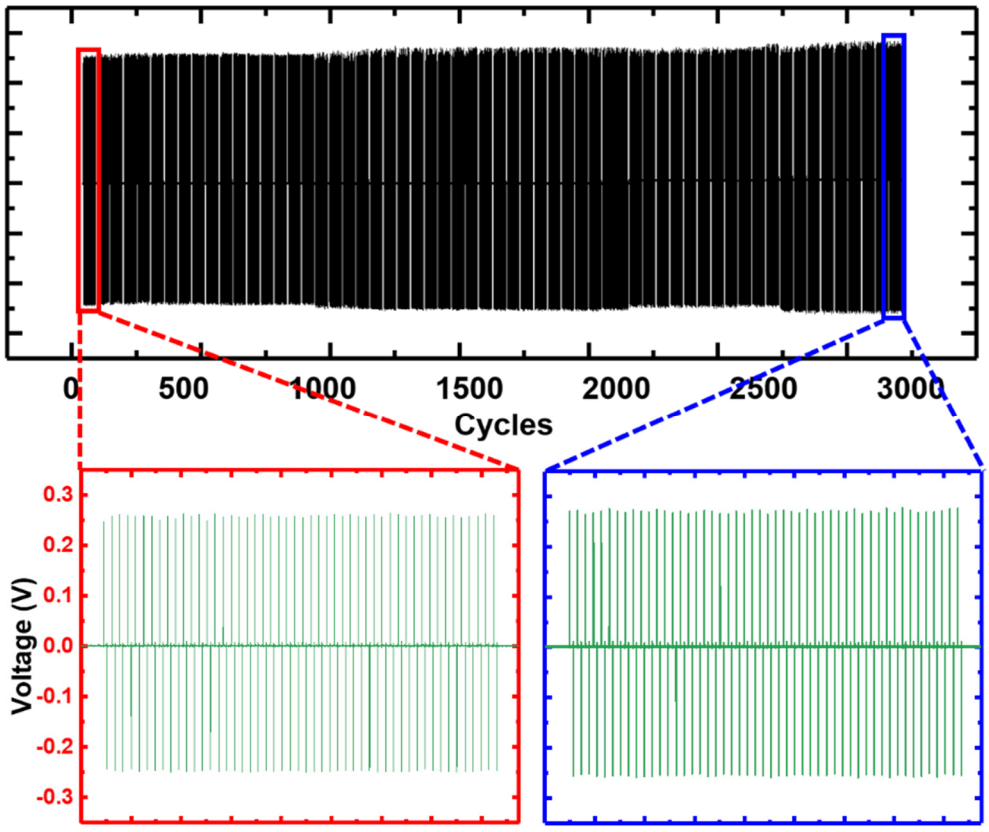

Figure 4.5. The stability of the Zig-Zag arrayed tactile sensor during 3000 cycles. First (red box) and last (blue box) 50 piezoelectric voltage.

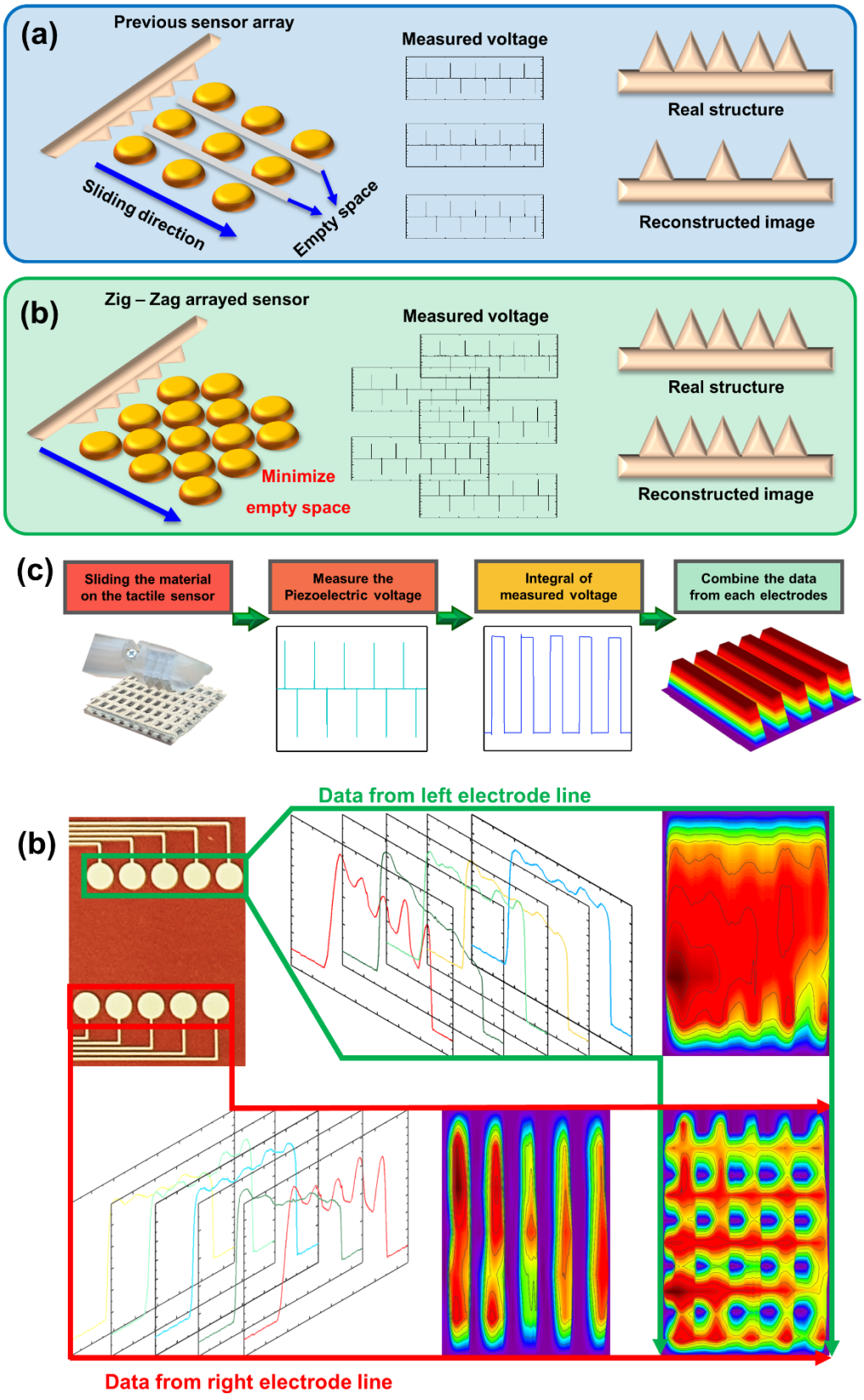

Figure 4.6. The concept schematic of surface rendering by (a) the matrix and (b) Zig-Zag arrayed tactile sensor, (c) the process and (d) method of surface rendering by Zig-Zag arrayed tactile sensor

4.4. Surface rendering method by the piezoelectric effect

When certain material is rubbed on the tactile sensor, the surface structure interacted with the electrode. Generally, the electrodes of the multi-array tactile sensor are constructed like cross-matrix array of other tactile sensors like the left of Figure 4.6(a). In this case, since the space between sensing cells were empty, the tactile sensor is not interacted with the surface topography of this space. In this case, there is empty space between the sensing unit in Figure 4.6(a). As a result, the voltage is not obtained at this region and the reconstructed image by the voltage is not similar to real structure like the right of Figure 4.6(a). However, suggested Zig-Zag arrayed sensor can minimize empty space like the left of Figure 4.6(b). As a result, the reconstructed image is much similar to the real surface topography like the right of Figure 4.6(b). As the rendering process in Figure 4.6(c), the tactile sensor with the piezoelectric materials and dome structure rubs the surface of certain materials. Then, the dome structure on the tactile sensor interacts with the surface structure of rubbed materials and the interaction results in the shear force in the first image of Figure 4.6(c) As a result, the piezoelectric materials embedded in the tactile sensor generates the voltage signal by the normal force converted by the dome structure like the second image of Figure 4.6(c). To reconstruct the topography from the dynamic piezoelectric signal, the measured voltage is integrated like the third image of Figure 4.6(c). This integrated piezoelectric voltage means the piezoelectric charge and the charge reflects the surface topography because the charge generation is dynamically changed by the interaction situation between the dome structure and the surface of certain materials. Finally, based on the integral data, 3D surface structure is reconstructed like fourth of Figure 4.6(c). Figure 4.6(d) shows the reconstruction method of wide area by the Zig-Zag arrayed tactile sensor. Above mentioned, the reason of Zig-Zag arrayed electrode is to enhance the resolution of rendering image by reducing no interacted

region. The piezoelectric signal is measured from left and right electrodes, respectively. The reconstruction from the straight-line electrode may be possible like middle image of Figure 4.6(d). However, the rendering results is different with real structure because of the empty space between each cell. In other studies, the tactile sensor having matrix array with row and column line electrode have similar problem because of empty space. Therefore, in this study, to fill this space, we arrange the right electrode of tactile sensor intercrossed with the left electrode line like the image of Figure 4.6(d).

4.5. Surface rendering result of 3D printed materials

To test the reconstruction of the surface topography, the structures are printed by 3D printer. The structures consist of the shape of check, line, dot pattern and word (DGIST) to confirm the advantages of the Zig-Zag electrodes array in Figure 4.7(a) to (d). This means that certain space or structure between patterns is intentionally placed at the location where the morphology cannot be measured unless the design of tactile sensor is Zig-Zag array. Then, to obtain the surface information, the tactile sensor rubs these printed materials and the piezoelectric voltage is collected from left and right electrodes, respectively.

Figure 4.8 and 4.9 are the rendering results by the piezoelectric signal of left and right side of Zig-Zag electrode array, respectively. The results indicate that the rendering result is considerably different to real case since the surface information between sensing cells are not obtained by the tactile sensor. Comparing rendering image, the result by left side electrodes are similar between Figure 4.8(a) and (b) but the results by right side electrodes are very different like Figure 4.9(a) and (b). In addition, although Figure 4.9(b) and (c) reconstructed by right side seems same or similar structure like empty space, the (b) and (c) of Figure 4.8 by left side show the different structure. Then, when the word structure

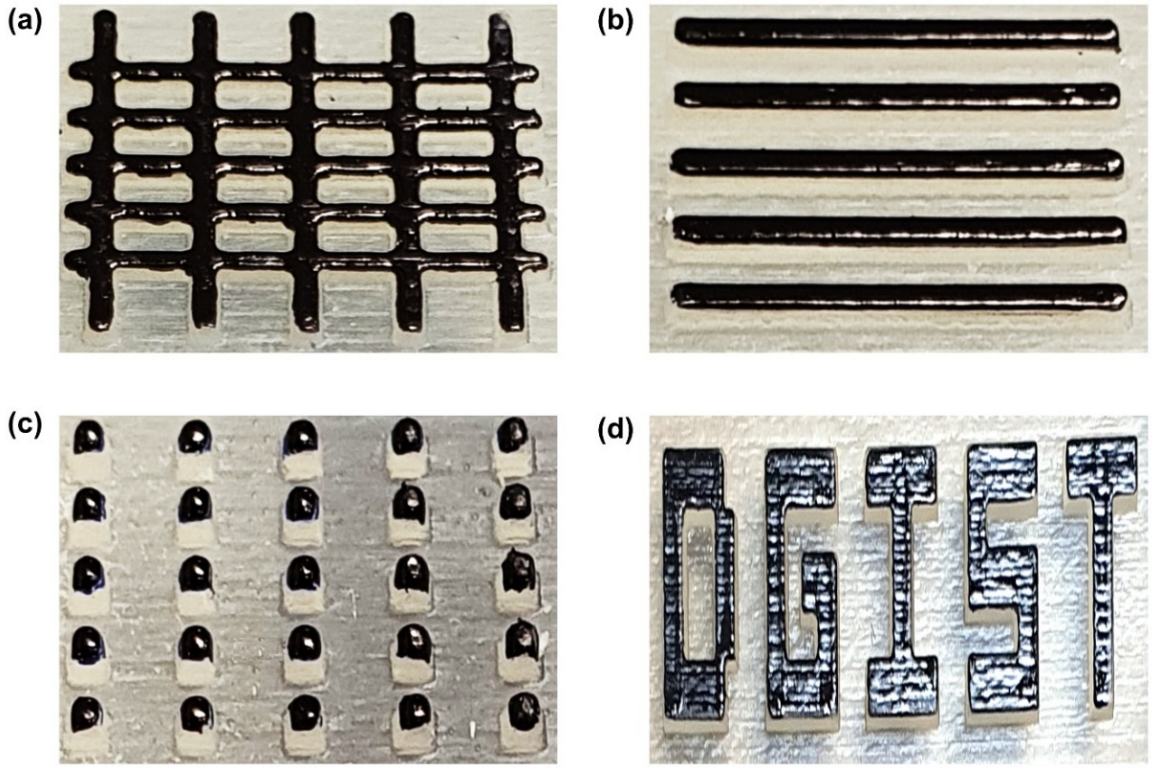

Figure 4.7. 3D printed materials for the rendering test

(DGIST) rubs the tactile sensor, the rendering result is also measured in (d) of Figure 4.8 and 4.9. Although the rendering results of two cases seem to be reconstructed well, the detail point like the edge of each character shows broader image than the image of real structure (Figure 4.7(d)). Additionally, the character S does not be rendered by the data from right electrode (Figure 4.9(d)). These comparing result indicate that the data loss is happened when the parallel-like straight-line or matrix type electrode array measure the information about surface topography. However, if the data obtained from left and right electrode arrayed Zig – Zag type is applied to the rendering, the reconstructed images in Figure 4.10 are much more similar to the real cases (Figure 4.7) than the images of the previous cases in Figure 4.8 and 4.9. In this results, narrow space not interacted with dome structure in the previous case is well realized. Specially, the shape of the word (DGIST) in Figure 4.10(d) is shaper and more delicate than the previous results.

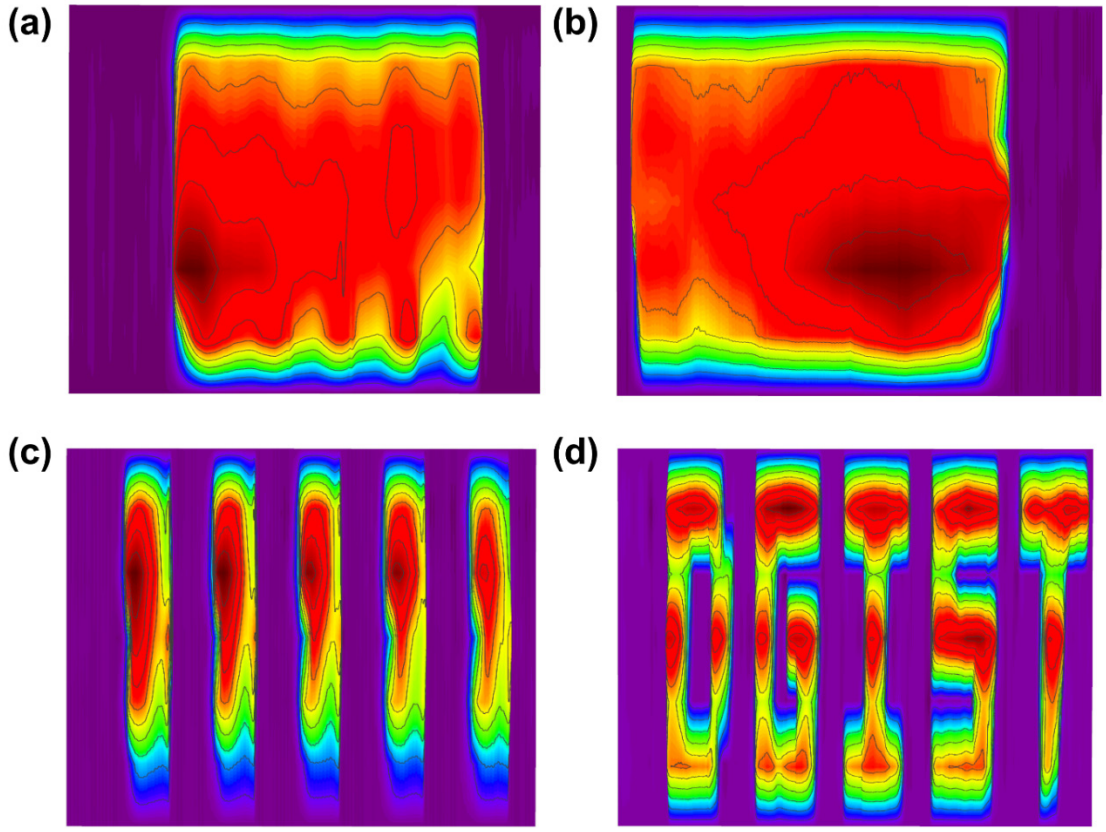

Figure 4.8. 3D rendering result based on the data from only left electrodes

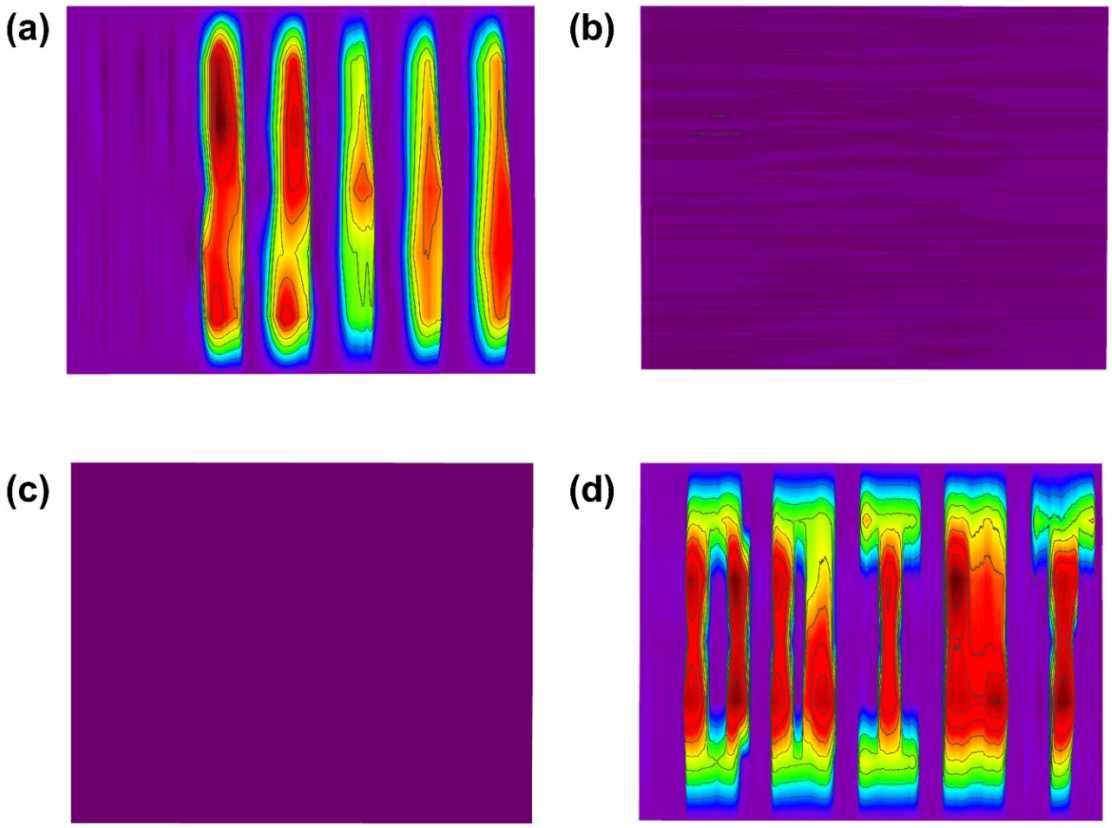

Figure 4.9. 3D rendering result based on the data form only right electrodes

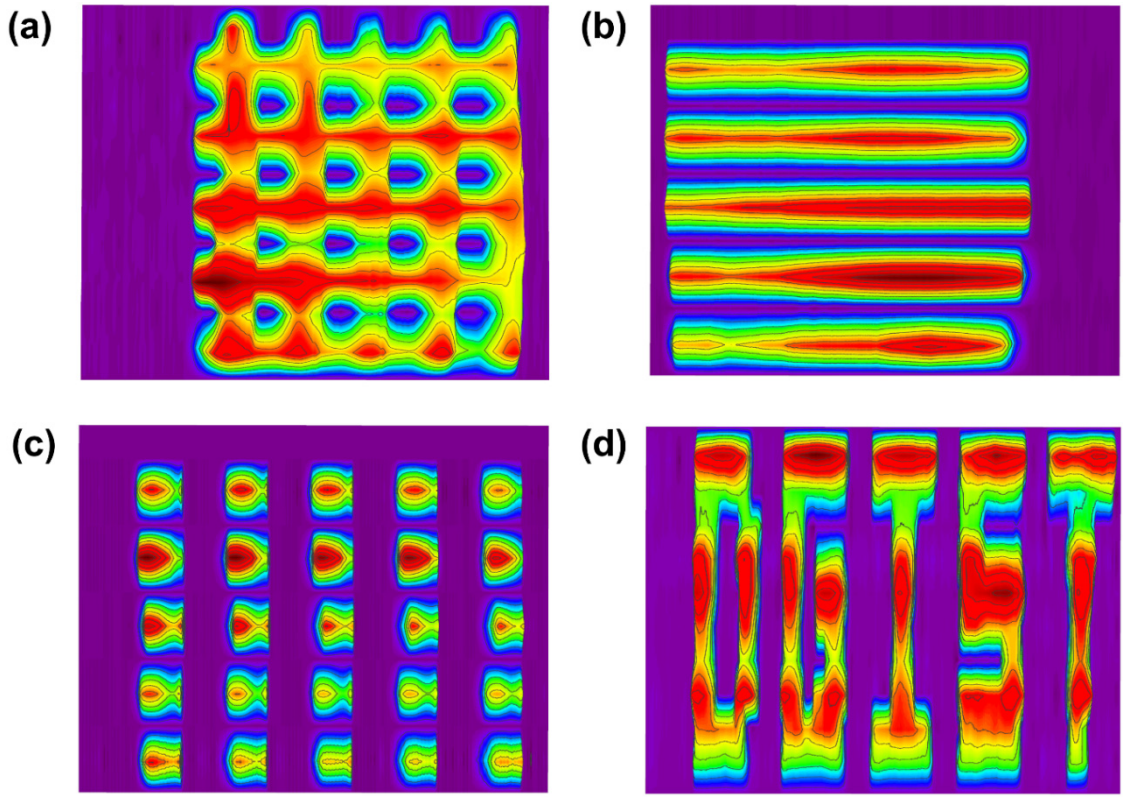

Figure 4.10. 3D rendering result based on the combined data of left and right electrodes.

4.6. Temperature sensing in sliding the high temperature material on Zig-Zag tactile sensor

Zig-Zag tactile sensor is designed to measure not only surface morphology but also temperature by placing the temperature sensing part between the electrodes like Figure 4.1(a). This part plays a role as the thermistor. Therefore, basically, the relationship between the temperature and resistance variation is expressed by following equation.

$$\Delta R = \kappa \Delta T \tag{4.1}$$

Here, ΔR is the resistance change, ΔT is the change in temperature and κ is the first-order temperature coefficient of the material. Because κ is the unique value of the material, the resistance variation may be changed by base material of thermistor.

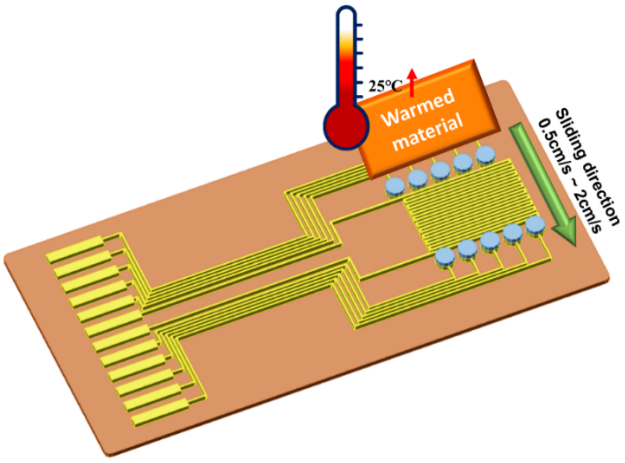

Figure 4.11. The temperature measurement setup.

The warmed material from 30 to 60℃ is used for the temperature measurement at intervals of 5℃. The temperature sensing is carried out by sliding the high temperature material on the sensor like Figure 4.11. Specially, the sliding velocity is also controlled by moving equipment from 0.5 cm/s to 2.0 cm/s at intervals of 0.5cm/s. Because the degree of resistance change by temperature may not be constant in accordance with the sliding velocity, it is important to match the resistance change by the sliding velocity. The temperature sensing result is indicated in Figure 4.12. The resistance of temperature sensor between Zig-Zag arrayed tactile sensor tends to increase when the material with high temperature pass on the temperature sensor. The changed resistance is from 3 % to 97 % and defined by following equation.

$$\text{Chagned value} = \frac{R_0 - \Delta R}{R_0} \times 100\% \tag{4.2}$$

R_0 is the original resistance of temperature sensor and ΔR is the changed resistance by temperature. This tendency is commonly applied to all measurement cases whether the sliding velocity is fast or not in Figure 4.12(a) to (d). However, the result indicates that the slower sliding velocity is, the larger resistance change is generated. The reason is that the resistance of temperature sensor is less changed, if the materials as thermal source pass on the tactile sensor with fast velocity. The temperature sensitivity is presented in Figure 4.13.

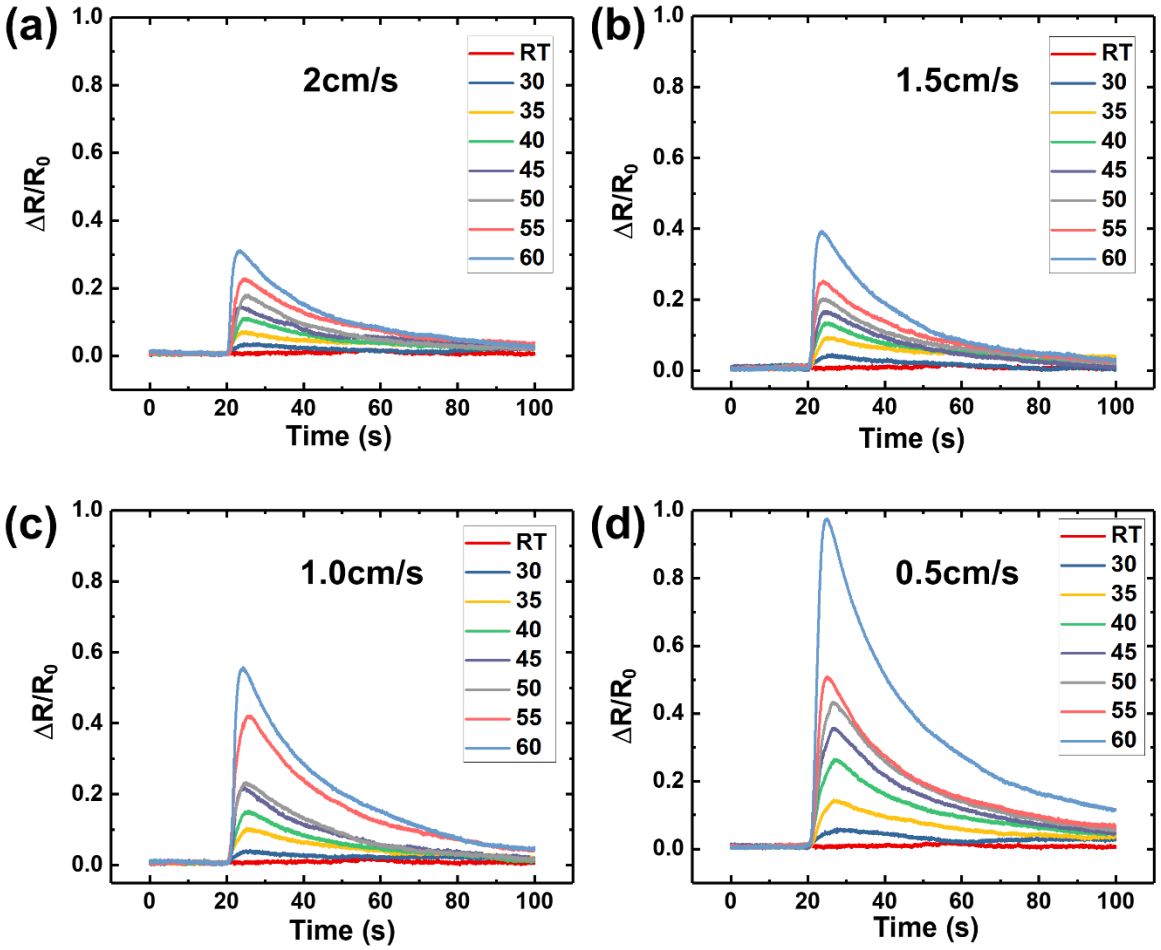

Figure 4.12. The schematic of temperature measurement by sliding the certain materials on the tactile sensor.

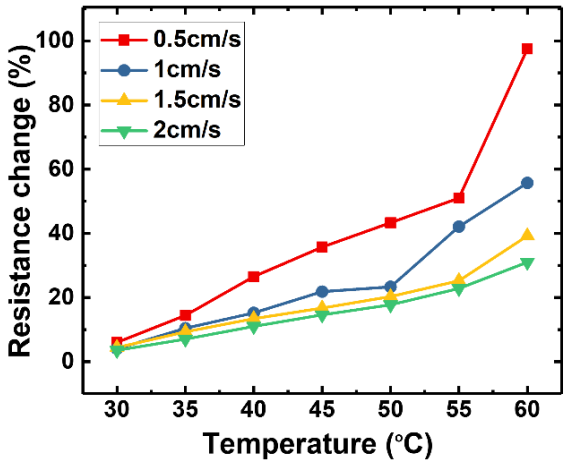

Figure 4.13. The temperature sensitivity of the tactile sensor by sliding.

In this chapter, we suggested novel Zig-Zag arrayed tactile sensor to obtain the surface topography and temperature of sliding certain material. Because the electrode array of our sensor minimizes the data loss from the surface information, it is useful to reconstruct the surface information with high resolution by the haptic application. As a result, the surface topography was successfully reconstructed with a 3D structure. The proposed method not only rendered the shape of 3D structure but also calculated their size due to the multi-array sensor. In addition, by installing the temperature sensing part between left and right electrode of tactile sensor, the temperature of sliding materials with various speed can be successfully measured. Therefore, we expect that our result can be applied to the novel haptic system, touch screen, or other electronic skin applications like VR equipment for the improvement or replacement of the human skin system.

4.7 Reference

[1] Yang, X., Xiong, Z., Chen, Y., Ren, Y., Zhou, L., Li, H., Zhou, Ye., Pan, F., and Han, S. T. "A self-powered artificial retina perception system for image preprocessing based on photovoltaic devices and memristive arrays", Nano Energy, 78, 2020, 105246.

[2] Chow, A. Y., Chow, V. Y., Packo, K. H., Pollack, J. S., Peyman, G. A., and Schuchard, R. "The artificial silicon retina microchip for the treatment of visionloss from retinitis pigmentosa", Archives of ophthalmology, 122(4), pp. 460-469.

[3] Kyuma, K., Lange, E., Ohta, J., Hermanns, A., Banish, B., and Oita, M "Artificial retinas—fast, versatile image processors", Nature, 372(6502), 1994, pp. 197-198.

[4] Röck, F., Barsan, N., and Weimar, U. "Electronic nose: current status and future trends", Chemical reviews, 108(2), 2008, pp. 705-725.

[5] Di Rosa, A. R., Leone, F., Cheli, F., & Chiofalo, V. "Fusion of electronic nose, electronic tongue and computer vision for animal source food authentication and quality assessment–A review", Journal of Food Engineering, 210, 2017, pp. 62-75.

[6] Korotcenkov, G. (2013). Handbook of gas sensor materials. Volume 1: Conventional Approaches.

[7] Shintaku, H., Nakagawa, T., Kitagawa, D., Tanujaya, H., Kawano, S., and Ito, J. "Development of piezoelectric acoustic sensor with frequency selectivity for artificial cochlea", Sensors and Actuators A: Physical, 158(2), 2010, pp. 183-192.

[8] Lyon, R. F., and Mead, C. "An analog electronic cochlea", *IEEE Transactions on Acoustics, Speech, and Signal Processing*, 36(7), 1988, pp. 1119-1134.

[9] Phat, C., Moon, B., and Lee, C. "Evaluation of umami taste in mushroom extracts by chemical analysis, sensory evaluation, and an electronic tongue system", *Food Chemistry*, 192, 2016, pp. 1068-1077.

[10] Ha, D., Sun, Q., Su, K., Wan, H., Li, H., Xu, N., Sun. F, Zhuang. L., Hu. N., and Wang, P. "Recent achievements in electronic tongue and bioelectronic tongue as taste sensors", *Sensors and Actuators B: Chemical*, 207, 2015, pp. 1136-1146.

[11] Chortos, A., Liu, J., and Bao, Z., “Pursuing prosthetic electronic skin”, *Nature materials*, 15(9), 2016, pp. 937-950.

[12] Hammock, M. L., Chortos, A., Tee, B. C. K., Tok, J. B. H., and Bao, Z. “25th anniversary article: the evolution of electronic skin (e-skin): a brief history, design considerations, and recent progress”, *Advanced materials*, 25(42), 2013, pp. 5997-6038.

[13] Sim, M., Lee, K. H., Shin, K. S., Shin, J. H., Choi, J. W., Choi, H., Moon. C., Kim. H. S., Cho. Y., Cha. S. N., Jung. E. J., Sohn. J. I., and Jang. J. E. (2019). Electronic Skin to Feel “Pain”: Detecting “Prick” and “Hot” Pain Sensations. Soft Robotics, 6(6), 745-759.

[14] Lee, J. S., Shin, K. Y., Cheong, O. J., Kim, J. H., and Jang, J. “Highly sensitive and multifunctional tactile sensor using free-standing ZnO/PVDF thin film with graphene electrodes for pressure and temperature monitoring”, Scientific reports, 5, 2015, 7887.

[15] Tien, N. T., Jeon, S., Kim, D. I., Trung, T. Q., Jang, M., Hwang, B. U., Byun. K-E., Bae. J., Lee. E., Tok. J. B., Bao, Z., Lee. N-E and Park. J.-J., “A flexible bimodal sensor array for simultaneous sensing of pressure and temperature”, Advanced Materials, 26(5), 2014, pp. 796-804.

[16] Han, S., Kim, J., Won, S. M., Ma, Y., Kang, D., Xie, Z., Lee. K-T., Chung. H. U., Banks. A., Min. S., Heo. S. Y., Davies. C. R., Lee. J. W., Lee. C.-H., Kim. B. H., Zhou. Y., Wei. Chen., Feng. X., Huang. Y., Rogers. J. A., “Battery-free, wireless sensors for full-body pressure and temperature mapping”, *Science translational medicine*, 10(435), 2018.

[17] Shin, K., Kim, D., Park, H., Sim, M., Jang, H., Sohn, J. I., Cha. S. N., and Jang, J. E., “Artificial Tactile Sensor With Pin-type Module for Depth Profile and Surface Topography Detection”, *IEEE Transactions on Industrial Electronics*, 67(1), 2019, pp. 637-646.

V. TACTILE SENSING SYSTEM FOR PAIN AND SMOOTH/ROUGH DETECTION

5.1. Introduction

Digital experiences based on the five human senses have improved with advancements in electrical devices and signal processing.[1] For example, virtual reality (VR) provides visual and auditory sensations, and more personalized services can be supplied by augmented reality (AR), which delivers three-dimensional (3D) spatial images and stereo sound.[2,3] Digital experiences are used in many fields, including entertainment and internet marketing.[4,5] Furthermore, these technologies were evolved in an attempt to exchange emotions between humans and machines. For a more immersive digital experience, sensing and delivering tactile information is necessary, where touching an object by hands is distinct from seeing and hearing. Therefore, considerable attention has been paid to technologies that provide tactile information, and various tactile sensors and actuators have been proposed and developed.[6-18] However, unlike for vision and hearing, an artificial tactile or haptic system is limited in its ability to directly transfer physical values to humans or machines because of difficulties in generating tactile feelings.

Tactile sensation plays important roles in our interactions with the external world, from both physical and emotional perspectives.[19] On touching or sliding the fingers across an object, individuals may describe the tactile emotional sensation as “soft,” “hard,” “smooth,” “rough,” or even “painful”.[20] Artificial tactile perception relies on the processing capability and hardware. Tactile receptors measure a unique feature of a tactile object, such as hardness, pressure, temperature, friction, or vibration.[21,22] Therefore, an artificial sensor system must obtain the same amount of physical information as a human does. However, the integration of different sensors within a single synthetic finger currently requires a bulky

structure and complex fabrication processes, and is less reliable as well.[23-26] Despite much information obtained by various receptors, the principal components of the tactile sensations experienced by humans can be described mainly as hardness, surface topography, and temperature.[27] Therefore, a single multifunctional tactile sensor detecting various parameters is required. Artificial tactile cognition has been studied to resemble the human brain processing.[28-31] The material classification ability of these systems, based on texture detection, has become similar to those of humans.[32] Over the hardware issue, recently, deep learning has been employed in this field, especially to differentiate various types of materials, and it has improved the accuracy of material classification.[33-35] However, these tactile material classifications do not represent the overall tactile sensation of human. Because the processing of tactile feeling by the human brain has not yet been revealed clearly and tactile responses vary among humans, it is challenging to imitate the tactile sensation by an artificial system.

Herein, based on the researches of previous chapters, an artificial tactile sensing system is established in this chapter. This system can preferentially generate pain waring signal by high pressure and temperature in accordance with the predefined process. After that, the other system determining the roughness of materials; “smooth/soft” or “rough”. The reference value for pain or roughness sensation is based on the human test. In other words, participants touch the sharp or hot materials to confirm the threshold of pain sensing or rub the fabric materials to feel the roughness of materials.

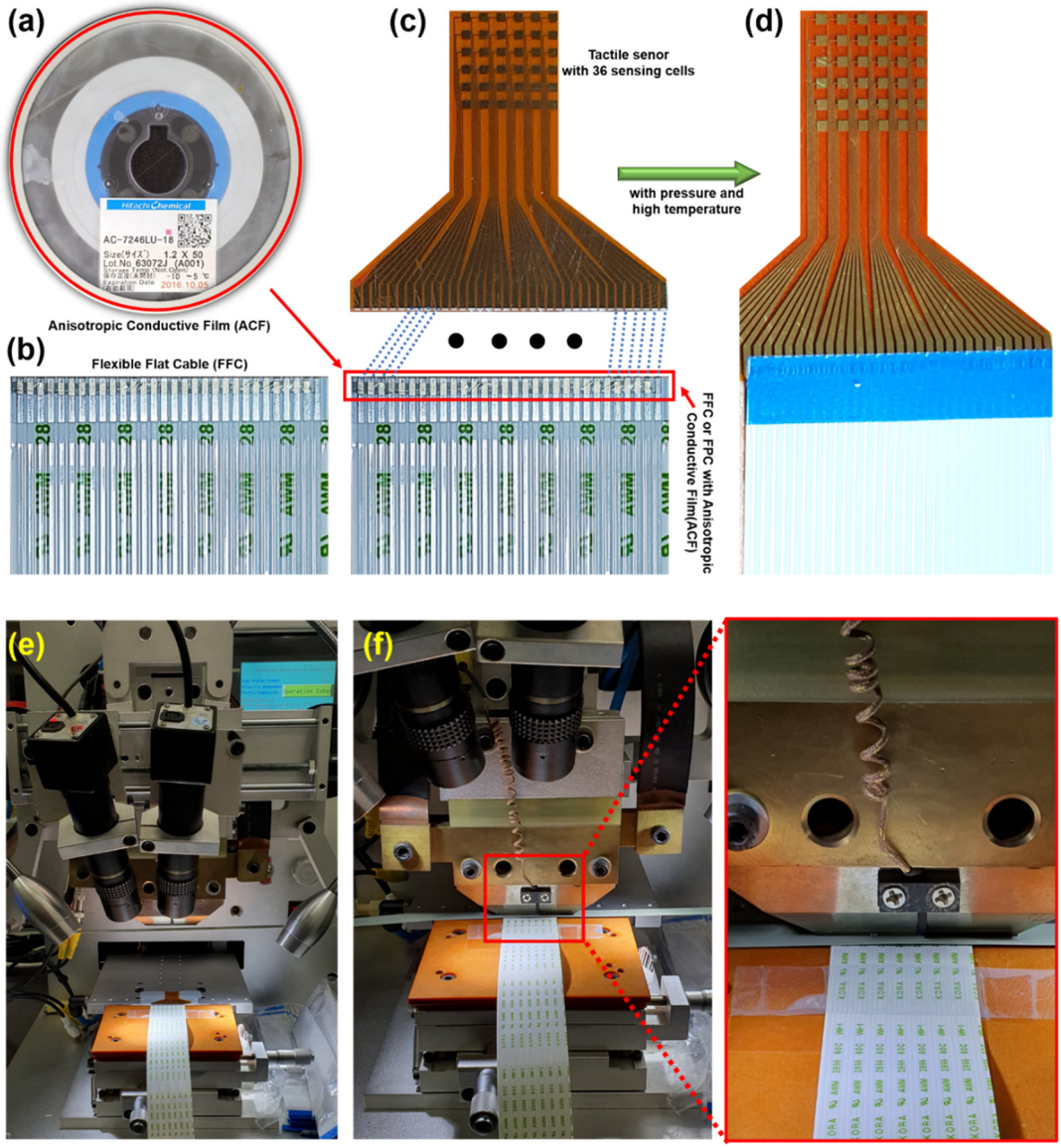

Figure 5.1. The images for the connection between the sensor and the sensing system, (a) Anisotropic Conductive Film (ACF), (b) Flexible Flat Cable (FFC), (c) before and (d) after the connection of the FFC and tactile sensor, (e) FPC bonding machine (f) pressing the interconnected region with high temperature.

5.2. Components of the tactile sensing system

The interconnection between tactile sensor and multichannel sensing system is demonstrated in following. For this system, the tactile sensor with the 30 sensing cells should be connected with the multichannel tactile system. To overcome the wiring issue of

multiarray tactile sensor, the tactile sensor is attached with Flexible Flat Cable (FFC, Figure 5.1(a)) by using Anisotropic Conductive Film (ACF, Figure 5.1(b)). Because the ACF have the conductive grain in adhesive tape, the electrode pads of tactile sensor are conductively connected with FFC. In Figure 5.1(c), each pad is matched to FFC with ACF. Because of the limitation of the number of multichannel oscilloscopes, only 30 cells of the tactile sensor (5×6) are used for the tactile sensing system like Figure 5.1(c). The bonding of the FFC and the tactile sensor is processed by FPC bonding machine. High temperature about 280℃ and a little pressure are applied to the interconnected region of the FFC and the tactile sensor in Figure 5.1(e) and (f). In this research, basic sensing performance of artificial tactile sensor is carried out a digital oscilloscope and a low-noise current preamplifier (Stanford Research System, Model: SR570). Then, artificial tactile system distinguishing pain or roughness consists of a multi-source data acquisition system (PXIe-5105) of National Instrument Co, XYZ moving equipment, and the control system embedded in the computer (Figure 5.2). In two measurement setup, sampling rate is 1k/s and little fluctuation and signal noise are removed by low pass filtering system (cut off frequency: 60Hz) of LabVIEW program and low-noise current preamplifier to enhance SNR.

5.3. Artificial tactile sensing system for generating the pain warning

Based on the piezo-seebeck signal from 30 cells of our sensor, the pain feeling by sharp or prick and hot feeling by hot material can be generated by our system. Warning signal by the stimulus is determined by the process of Figure 5.3. First, the system decides that the contacted materials is sharp or not based on the number of sensors generating signals. If the number of the sensor generating signal is smaller than predefined number, the contacted materials is considered to be sharp or prick. After the decision about the shape

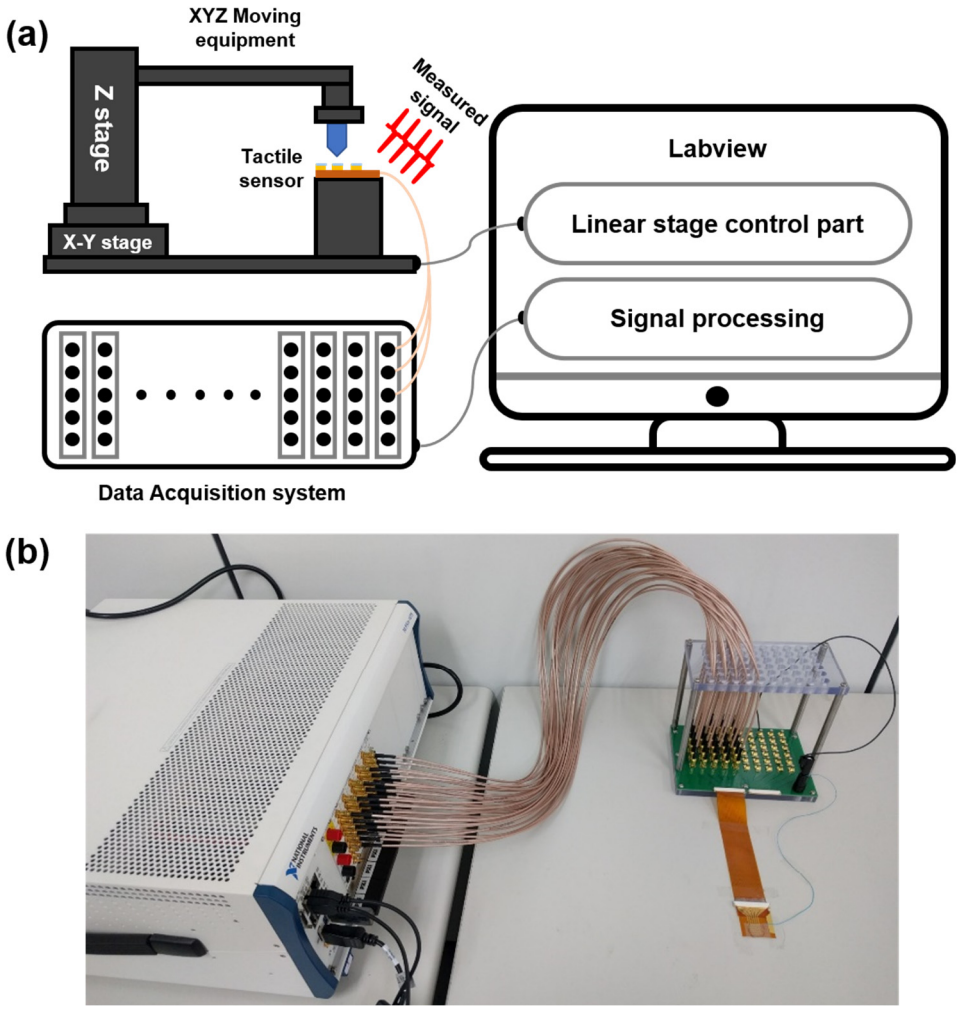

Figure 5.2. (a) The schematic and (b) real image explaining the process of Multichannel Data Acquisition system for the tactile sensing system

of materials, the warning signal is generated if the level of the piezoelectric signal is higher than the threshold. In contrast, if the number of the sensor generating signal is more than predefined number, the stimulus is considered to be hot or a blunt material. To distinguish the kinds of stimulus which is the pressure or the temperature, the number of 1st derivative value similar to zero and the output level over the zero are considered by the system simultaneously. If the values of two factors are higher than pre-defined value, the system decides that the stimulus is the temperature variation. Then, if the high temperature is applied to the tactile sensor, the output value by the seebeck effect is higher than threshold and the system generates the ‘hot’ warning signal.

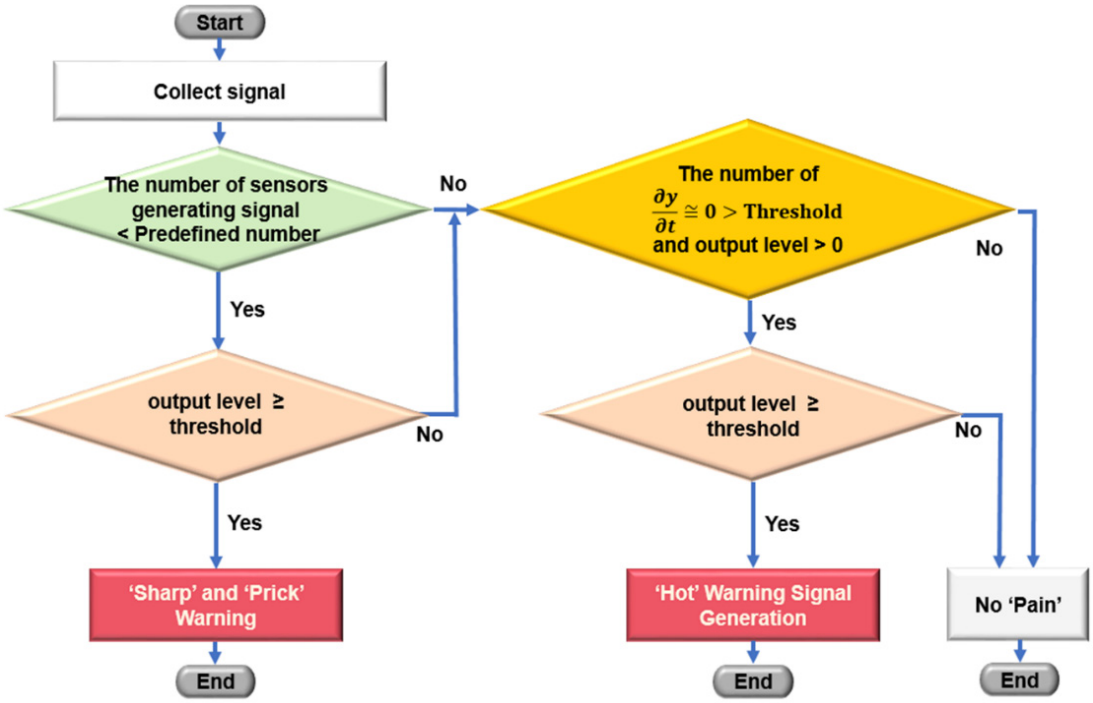

Figure 5.3. The pain sensing process by high pressure or temperature.

Figure 5.4 (a) and (b) show the voltage and current signals corresponding to the input pressure and the current output signals depending on the various temperature conditions, respectively. The signal level is high enough to be detected by a general electrical measurement system. The red regions in Figure 5.4(a) are that people generally begin to feel the pain. For the real case, the pain threshold range was measured by participants in Figure 5.4(a). The method is that sharp pencil about 1mm of diameter prick the real skin of participants by fixed force. The calculated pressure is about 95kPa. When this pressure is compared with the force of pressure measurement system, corresponding point is about 1.1N. Then, participants feel the pain by high temperature about 55 °C. Therefore, the red region in Figure 5.4(b) means the pain threshold of this sensor. The measured pain threshold of participants was presented in Table 5.1. The level can be threshold range to produce 'pain' feeling.

	Pain threshold by prick	Pain threshold by hot
Participant 1	93kPa	55°C
Participant 2	97kPa	60°C
Participant 3	87kPa	58°C
Participant 4	88kPa	64°C
Participant 5	105kPa	68°C

Table 5.1. The pain threshold by participants

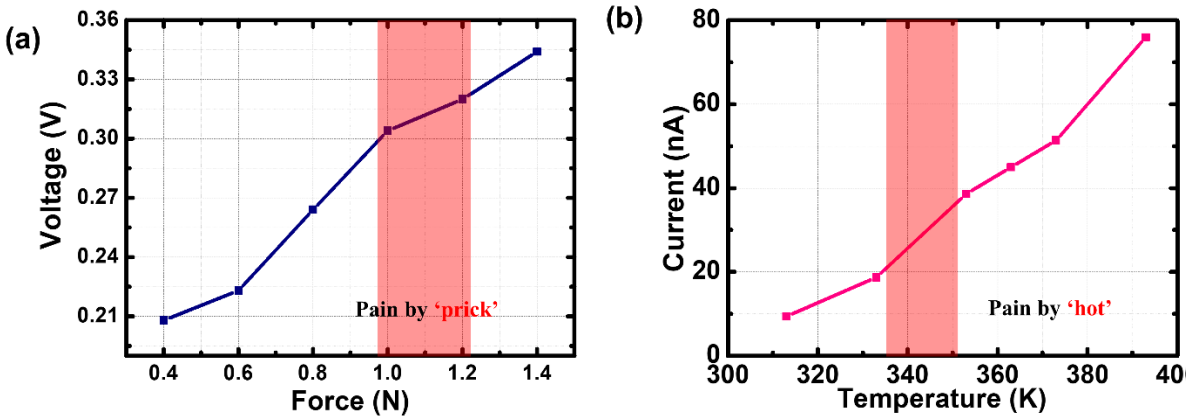

Figure 5.4. (a) The voltage sensitivity by pressure and (b) the current sensitivity by temperature variation, the red region is the starting point that the human feels pain by high pressure or temperature.

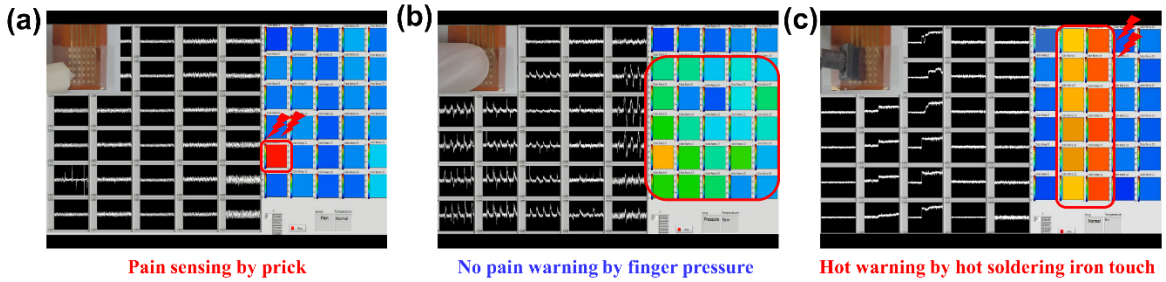

Figure 5.5. The captured image of the final, (a) 'prick', 'blunt' and (c) 'hot' feeling generation depending on various stimuli.

To realize the pain warning system by high pressure and temperature, the detail of experiment setup for multichannel data acquisition is following. This experiment is conducted by multi-channel data acquisition system (National instrument Co.) and the algorithm for signal processing is formed based on the flow chart in Figure 5.3. By this system, the operation display of this system is captured in Figure 5.5 when the various stimuli are applied to this system. As shown in Figure 5.5(a), the system shows 'prick pain' warning when tactile sensor is pressed by sharp material with high pressure, whereas, the system does not display warning signal when tactile sensor is pressed by blunt material (a finger) with high pressure in Figure 5.5(b). The Figure 5.5(c) shows 'hot' warning by hot material. The system shows 'hot' warning when hot material is in contact with tactile sensor.

5.4. Artificial tactile sensing system for smooth/rough sensing

Our artificial sensing finger with touch and slide sensors was designed to resemble human tactile sensing. The tactile sensing system consisted of a tactile sensor and 3D-printed artificial finger with movement capabilities. The tactile sensor, made from piezoelectric material, was combined with the artificial finger (Figure 5.6(d)) and equipment to enable movement (Figure 5.6(a) and (b)). The sensing process comprised the touching, sliding, and release stages. 42 fabric samples were used in this study (Figure 5.6(e)), and the order of presentation thereof depended on the degree of feeling (smooth/soft to rough) reported by each participant. To collect surface information for the fabric samples, the system touched and slid the sample materials. After measuring the signal arising from the sensing system, the data were transferred to the signal processing system. At this stage, the tactile feeling level was determined, i.e., smoother or less smooth relative to the judgment of the human participant.

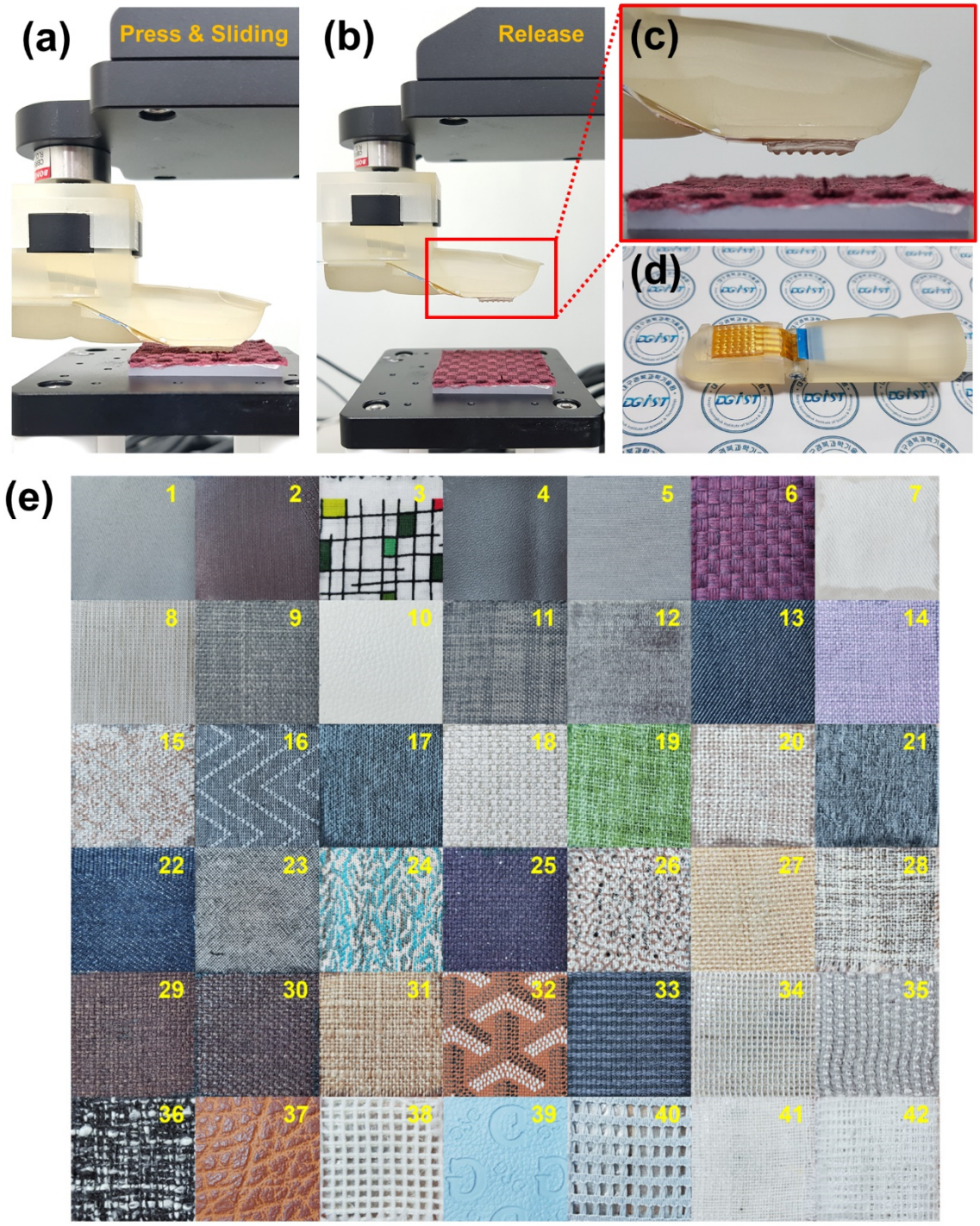

Figure 5.6. The setup of roughness sensing system with moving equipment and fabric samples for human test, (a) the touching, sliding, (b) release state of customized moving equipment, (c) the magnitude image of tactile sensor and rubbed surface material, (d) the tactile sensor with 3D-printed artificial finger model, (e) 42 of fabric used for this study.

	Trial 1	Trial 2	Trial 3	Trial 4	Trial 5	Trial 6	Trial 7	Trial 8	Trial 9	Trial 10	Trial 11	Trial 12	Trial 13	Trial 14	Trial 15	Trial 16	Trial 17	Trial 18	Trial 19	Trial 20
Soft	7	7	7	7	7	9	9	9	9	9	7	7	7	7	9	7	7	9	7	7
	9	9	9	9	9	7	7	7	7	7	9	9	9	9	35	9	9	7	9	9
	29	29	35	35	35	2	35	35	2	2	35	35	35	35	7	35	2	2	2	2
	15	2	29	2	29	15	2	2	35	35	2	2	2	2	2	2	35	35	35	35
	35	15	15	15	2	35	4	4	4	15	15	4	29	34	34	4	4	4	15	15
	17	1	34	29	15	29	15	15	15	4	4	15	4	29	15	34	29	15	34	34
	34	4	2	34	4	1	1	17	29	34	34	29	15	15	6	23	15	17	29	29
	2	6	17	1	13	4	29	3	6	6	29	1	34	4	17	15	34	34	4	17
	25	25	1	4	1	6	6	34	34	1	30	6	6	6	25	1	17	23	6	6
	1	13	30	6	34	13	13	6	1	30	6	34	17	1	1	25	23	1	30	4
	13	35	19	17	17	17	34	30	13	13	1	19	30	17	26	6	25	30	25	1
	22	30	4	13	6	30	25	1	17	24	25	17	13	26	23	17	6	6	1	13
	6	17	25	25	3	25	17	23	30	29	17	30	25	25	30	26	3	29	17	25
	30	26	23	23	30	34	26	13	25	25	26	13	1	30	5	29	1	13	26	30
	19	3	26	30	26	23	30	26	3	17	13	23	26	23	4	13	30	3	13	23
	23	23	3	26	25	5	21	5	23	3	19	25	23	13	29	19	26	25	24	26
	4	34	13	24	19	26	23	25	19	26	23	26	3	20	13	30	5	26	3	19
	26	11	6	21	12	19	3	29	21	23	21	24	21	24	3	5	21	21	19	3
	3	12	12	5	5	12	5	24	5	21	3	21	19	5	24	24	13	19	10	24
	5	24	16	19	20	24	24	20	10	19	10	3	24	21	20	11	19	10	21	21
	14	10	10	3	10	3	19	21	26	5	5	16	16	3	18	18	40	18	5	16
	12	20	5	16	23	21	16	18	40	16	16	5	10	18	11	20	11	20	16	12
	24	21	32	12	21	11	20	22	24	10	24	20	5	19	21	12	16	24	23	22
	21	27	14	10	24	18	18	40	16	28	20	11	18	11	19	3	10	5	20	10
	11	22	28	40	18	16	11	16	18	22	18	18	27	40	10	40	20	16	18	11
	16	19	27	20	32	20	32	10	11	12	11	40	20	39	12	21	18	27	11	5
	10	5	22	11	16	27	12	11	20	11	12	12	22	12	16	27	22	11	27	20
	32	40	24	22	11	22	27	19	12	20	22	28	11	27	22	39	27	12	39	18
	28	18	21	28	27	40	10	12	32	18	40	27	28	32	32	22	12	22	12	27
	27	28	11	32	39	39	22	27	22	27	39	10	12	16	27	32	24	40	40	40
	18	16	18	27	8	10	40	32	28	40	28	14	32	22	39	16	39	39	22	39
	20	32	20	14	36	32	28	14	27	39	36	22	14	10	40	10	28	14	14	28
	8	14	40	18	22	8	14	28	39	36	27	39	39	36	28	28	32	32	36	14
	40	39	8	39	31	31	8	39	14	32	14	32	40	28	38	37	14	28	28	36
	39	8	31	36	33	33	31	8	8	8	32	8	37	14	36	14	31	8	32	38
	31	36	33	38	28	28	33	36	31	31	8	36	8	8	31	8	33	31	31	32
	33	38	39	8	40	14	39	31	38	33	31	31	31	38	33	31	36	33	33	31
	37	37	36	33	14	38	38	33	33	14	33	37	33	31	8	33	38	37	8	33
	36	33	38	31	38	36	36	38	36	38	38	33	36	33	37	36	8	36	37	8
	38	31	42	37	37	42	37	37	37	42	37	38	38	37	14	38	42	38	38	37
	42	42	37	42	41	37	41	41	42	37	42	41	42	42	42	42	41	41	42	42
Rough	41	41	41	41	42	41	42	42	41	41	41	42	41	41	41	41	37	42	41	41

Figure 5.7. The ranked 42 fabric samples by participant No. 1.

Ten participants (three females and seven males) of age 22–33 years participated in the experiments. The participants are asked to rank 42 tactile samples (Figure 5.6(e)) from smooth/soft to rough; no time limit is imposed. The participants used both hands (all fingers) during the task; they are allowed to rub and touch the tactile materials with their fingertips,

but not scratch them with their nails. Each participant completed 20 trials. The sample materials are randomly distributed at the beginning of each trial to prevent memorization. There is an interval of at least 4 h between repeated trials. The ranked 42 fabric samples by participant No. 1 is presented in Figure 5.7. After more than 1 year, we perform a tactile cognition test with limited number of samples. Three materials are presented as anchor materials with rank scores (#1, #21, and #42) for the participants. Based on the known scores of the anchors, the participants perform scoring of the eight given test materials. The anchor materials and the eight given test materials are chosen differently from the previous tactile cognition test.

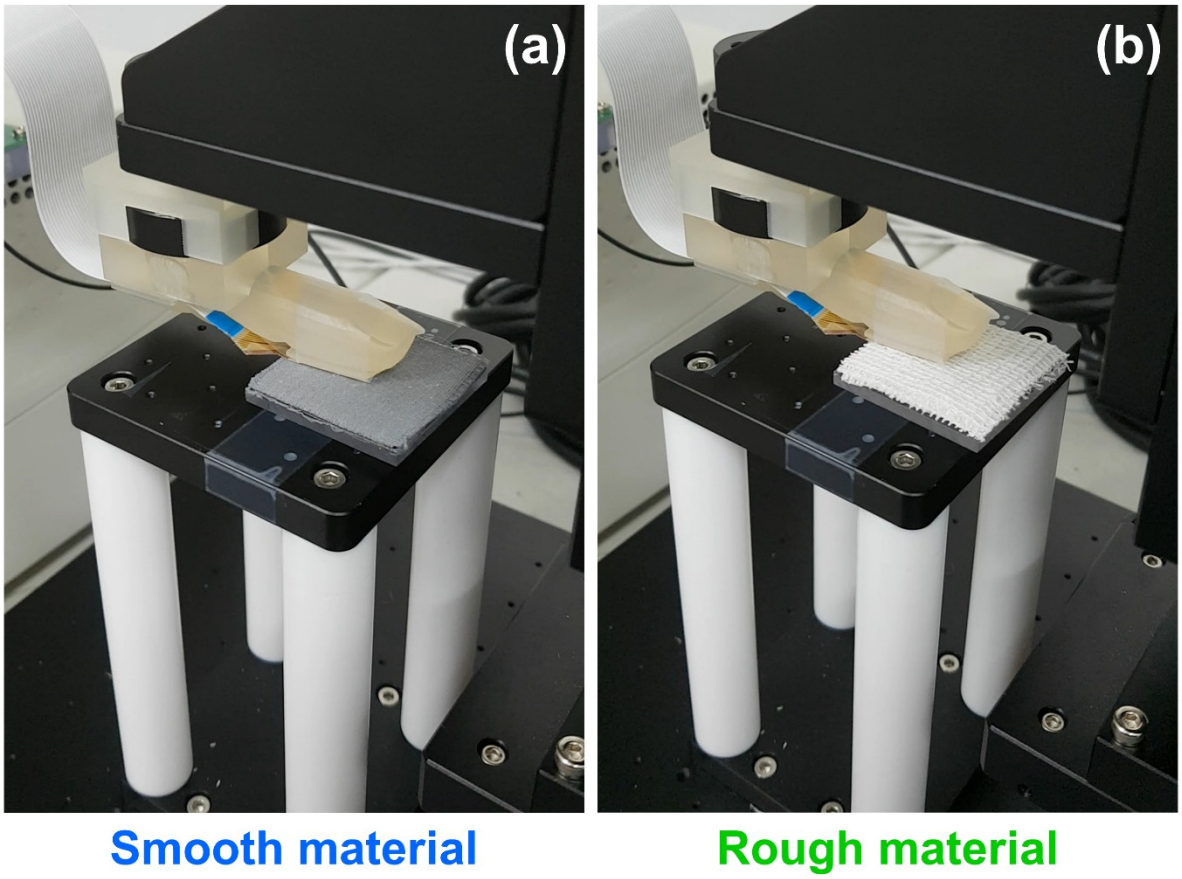

Figure 5.8. The tactile avatar system. (a) smooth/soft or (b) rough feeling signal was generated depending on tactile material feature when the material is not sharp after touching and sliding.

After that, the tactile system is designed to generate artificial tactile feeling in accordance with the feeling of a specific person (master) in Figure 5.8(a) and (b). If not sharp, the finger touches and slides on the material, and finally, produces the smooth/soft or rough tactile sensations. Since this sensation is trained by human tactile feeling, this system can be operated as the human. The tactile sensing system can generate feeling, ‘smooth/soft’ or ‘rough’ to unexperienced materials like human.

The importance of digital applications will continue to increase, and tactile systems representing the interaction of hands with objects will become important. In this chapter, we suggest a tactile avatar system generating the pain waring signal by sharp and hot material and feeling the roughness sensation like human. For the system, we adopt a systematic approach to mimic human tactile cognition. As a result, the system enables pressure and temperature stimuli to be detected and verified in a manner equivalent to an intelligent human brain. In addition, the principal tactile components experienced by humans, i.e., hardness and roughness, is processed by separable network layers that were designed for different functions to mimic the roughness sensation of human. Even in the difficult case of predicting the rank of a previously unexperienced tactile sample, the developed system performed similar to a human with the knowledge gained from previous experience. Ultimately, the system can distinguish the kinds of stimuli and generate artificial tactile signal such as the pain, smooth or roughness. Future research should improve the ability of the artificial tactile system to process more various tactile information, which will in turn allow machines to replace humans for a variety of the electronics, robotics, virtual spaces (i.e., VR and AR) or online environments.

5.5. Reference

[1] Svechtarova, Mila I, I. Buzzacchera, B. J. Toebes, J. Lauko, N. Anton and C. J. Wilson, Electroanalysis. 2016, 28, 1201.

[2] M. Slater, Front. Robot. AI. 2014. 1, 1.

[3] M. Billinghurst, A. Clark, and G. Lee, Foundations and Trends® in Human–Computer Interaction, 2015, 8, 73.

[4] W. Piekarski, and B. Thomas, Commun. ACM, 2002, 45, 36.

[5] P. A. Rauschnabel, R. Felix, and C. Hinsch, J. Retail. Consum. Serv. 2019, 49, 43.

[6] A. Chortos, J. Liu, and Z. Bao, Pursuing prosthetic electronic skin. Nat. Mater. 2016, 15, 937.

[7] S. Chun, I. Y. Choi, W. Son, G. Y. Bae, E. J. Lee, H. Kwon, J. Jung, H. S. Kim, J. K. Kim and W. Park. Adv. Funct. Mater. 2018, 28, 1804132.

[8] S. I. Rich, R. J. Wood, and C. Majidi. Nat. Electron, 2018, 1, 102.

[9] J. Kim, M. Lee, H. J. Shim, R. Ghaffari, H. R. Cho, D. Son, Y. H. Jung, M. Soh, C. Choi, S. Jung, K. Chu, D. Jeon, S-T. Lee, J. H. Kim, S. H. Choi, T. Hyeon and D-H. Kim, Nat. Commun, 2014, 5, 5747.

[10] C. Pang, G-Y Lee, T-I, Kim, S. M. Kim, H. N. Kim, S-H. Ahn and K-Y Suh, Nat. Mater. 2012, 11, 795.

[11] M. Sim, K. H. Lee, K. S. Shin, J. H. Shin, J-W. Choi, H. Choi, C. Moon, H. S. Kim, Y. Cho, S. N. Cha, J. E. Jung, J. I. Sohn and J. E. Jang, Soft. Robot. 2019, 6, 745.

[12] Y. Jeong, M. Sim, J. H. Shin, J-W. Choi, J. I. Sohn, S. N. Cha, H. Choi, C. Moon and J. E. Jang, RSC. Adv. 2015, 5, 40363.

[13] G. Schwartz, B. C-K. Tee, J. Mei, A. L. Appleton, D. H. Kim, H. Wang and Z. Bao, Nat. Commun. 2013, 4, 1859.

[14] R. Hensleigh, H. Cui, Z. Xu, J. Massman, D. Yao, J. Berrigan and X. Zheng, Nat Electron. 2020, 3, 216.

[15] Y-C. Huang, Y. Liu, C. Ma, H-C. Cheng, Q. He, H. Wu, C. Wang, C-Y. Lin, Y. Huang and X. Duan, Nat. Electron, 2020, 3, 59.

[16] K. Shin, D. Kim, H. Park, M. Sim, H. Jang, J. I. Sohn, S. N. Cha, and J. E. Jang IEEE. T. Ind. Electron, 2020, 67, 637.

[17] K. Shin, M. Sim, E. Choi, H. Park, J-W. Choi, Y. Cho, J. I. Sohn, S. N. Cha and J. E. Jang, IEEE/ASME. T. Mech. 2018, 23, 2638.

[18] M. Sim, K. H. Lee, Y. Jeong, J. H. Shin, J. I. Sohn, S. N. Cha and J. E. Jang, IEEE T. NanoBiosci. 2016, 15, 804.

[19] V. S. Ramachandran and D. Brang, Neurocase, 2008, 14, 309.

[20] M. Hollins and S. R. Risner, Percept. Psychophys, 2000, 62, 695.

[21] C. H. Lin, T. W. Erickson, J. A. Fishel, N. Wettels, and G. E. Loeb, in 2009 IEEE Inter. Conf. Robot. Biomimet (ROBIO). 19 Dec, 2009.

[22] R. S. Dahiya, G. Metta, M. Valle and G. Sandini, IEEE. T. Robot. 2010, 26, 1.

[23] S. Gupta, D. Shakthivel, L. Lorenzelli and R. Dahiya, IEEE. Sens. J. 2019, 19, 435.

[24] K. Kanao, S. Harada. Y. Yamamoto, W. Honda, T. Aire, S. Akita and K. Takei, RSC. Adv. 2015, 5, 30170.

[25] J. S. Lee, K-Y. Shin, O. J. Cheong, J. H. Kim and J. Jang, Sci. Rep, 2015, 7887.

[26] S. Harada, K. Kanao, Y. Yamamoto, T. Aire, S. Akita and K. Takei, ACS Nano, 2014, 8, 12851.

[27] S. J. Lederman and R. L. Klatzky, Cognitive. Psychol. 1987, 19, 342.

[28] S. Raspopovic, M. Capogrosso, F. M. Petrini, M. Bonizzato, J. Rigosa, G. D. Pino, J. Carpaneto, M. Controzzi, T. Boretius, E. Fernandes, G. Granata, C. M. oddo, L. Citi, A. L. Ciancio. C. Cipriani, M. C. Carrozza, W. Jensen, E. Guglielmelli, T. Stieglitz, P. M. Rossini and S. Micera. Sci. Transl. Med. 2014, 6, 222ra19.

[29] J. M. Romano, K. Hsiao, G. Niemeyer, S. Chitta and K. J. Kuchenbecker, IEEE. T. Robot. 2011, 27, 1067.

[30] K. Peyre, m. Tourlonias, M-A. Bueno, F. Spano, and Rene. M. Rossi, Tribol. Int. 2019, 130, 155.

[31] Z. Kappassov, J-A. Corrales, and V. Perdereau, Robot. Auton. Syst, 2015, 74, 195.

[32] S. Chun, W. Son, H. Kim, S. K. Lim, C. Pang and C. Choi, Nano letters, 2019, 19, 3305.

[33] Y. Gao, L. A. Hendricks, K. J. Kuchenbecker and T. Darrell, in 2016 IEEE International Conference on Robotics and Automation (ICRA). 16. May, 2016.

[34] M. Strese, C. Schuwerk, A. Iepure, and E. Steinbach, IEEE. T. Haptics, 2016, 10, 226. 10, 226-239 (2016).

[35] H. Zheng, L. Fang, M. Ji, M. Strese, Y. Özer and E. Steinbach, IEEE. T. Multimedia, 2016, 18, 2407.

VI. CONCLUSION

In conclusion, the artificial tactile sensing system and the signal processing method are proposed based on the self-powered piezoelectric tactile sensor. ZnO nanowire and P(VDF-TrFE) are mainly used for the piezoelectric effect. First, the performance enhancement of the tactile sensor based on the ZnO nanowire is achieved by structural and simple fabrication solution and the power generation and pressure sensitivity is dramatically increased from 3 to 11 times. The mechanism enhancing the piezoelectric effect of ZnO nanowire pressure sensor is proved by FEM simulation (COMSOL). Because this solution doesn't need other anneal process compensating oxygen vacancies at high temperature, we expect the applicability of the tactile sensor with flexible substrate.

After the enhancement of the pressure sensor, the effort to detect the surface roughness is followed. Because the roughness sensation is determined by the combination of various parameters, the researches to obtain the surface information such as the hardness, the surface morphology, pitch of pattern and the depth of materials depth is carried out with novel structure like dome structure. To collect the surface information and amplify the piezoelectric signal, the PDMS dome structure is applied to the tactile sensor. As a result, the shear force generated by the interaction between the surface structure and the PDMS dome is successfully transferred to the tactile sensor as the type of normal force. Because the transferred normal force also includes the surface information, various information mentioned above is well obtained by the tactile senor with PDMS dome structure.

Then, because the roughness sensation consists of the combination of various surface information, we suggest the method to obtain the shape of the surface topography. The novel

Zig-Zag type electrode arrays is applied to the tactile sensor to minimize the data loss at the empty space interacting with the tactile sensor. The high-resolution rendering image can indicate the size and shape of surface samples, simultaneously. Also, the temperature information of the sliding samples is also measured on sliding by the embedded temperature sensor between the pressure sensing parts.

Ultimately, because it is important to not only sense various factors but also communicate with brain system based on detected factors, finally, we suggest the artificial tactile sensing system generating the signal by the pain or roughness based on the measured information by the tactile sensor. As a result, our system can immediately generate the warning signal when the sharp or hot material is in contact with the tactile sensor in accordance with pain sensing algorithm. In addition, the roughness sensing system is also developed by the deep learning process. Because it is impossible to predict unexperienced tactile samples by the deep learning process, the human test data is applied to the tactile system and the roughness determination of unexperienced tactile samples was successfully conducted by our artificial tactile system feeling like human.

Even if there are some issue to be solved, the tactile sensor of this research distinguishing various tactile factors (Pressure, Temperature, Surface shape, Hardness, Roughness and so on) can be the foundation of future tactile applications. Therefore, this research can be used for future wearable device, artificial electronic skin for prosthetic, health care monitoring, touch panel, haptic applications, and other electronic device related to touch sensing. Ultimately, through collaborative research with brain science, signal processing and other fields, we expect that the mimicking of the emotion from tactile feeling will be realized for the human-like tactile system.

요 약 문

압전 물질을 이용한 다기능 촉각 센싱 시스템

사람은 외부의 환경과 정보를 주고받는 시각, 청각, 후각, 미각, 촉각 등 다섯 개의 감각을 가지고 있다. 이 중 하나의 감각이라도 이상이 생기면 상당한 불편을 호소할 만큼 인간 생활에 중요한 역할을 한다. 따라서 인간의 감각을 모방하기 위한 많은 연구들이 진행 중이다. 모방해야 하는 인자가 적은 청각(주파수)과 시각(빛의 삼원색, RGB)은 많은 연구를 통해 상당히 높은 수준 또는 인간의 감각보다 훨씬 뛰어난 성능을 가지는 소자나 카메라, TV, 마이크, 스피커 등의 전자기기 형태로의 개발에 성공했다. 하지만 모방해야 할 인자가 많은 촉각, 후각, 미각 등은 아직 복잡한 인간의 감각을 모방하지 못하는 어려움이 있어 더 많은 연구 개발이 필요하다. 그 중에서 촉각은 인간이 정복하지 못한 남은 감각들 중 그나마 모방해야 하는 인자가 적기 때문에 (압력, 온도, 거칠기, 형태 인식, 물체의 질감 등) 현재 많은 연구가 이루어지고 있는 상황이다. 기본적으로 촉각에 대한 모방은 압력이나 온도 센서의 개발에서부터 시작한다. 그 동안의 많은 연구들은 센서의 성능(민감도, Robustness, 반응속도 등)을 향상시키기 위한 연구에 집중하는 경향을 보여왔고 지금도 많은 연구들이 보고되고 있다. 하지만 센서의 개념을 넘어 촉각을 모방해야 하는 입장으로서 센서의 민감도가 아닌 고통이나 거칠기, 뜨거움 등 다양한 정신 감각적인 자극을 인지하는 시스템을 만들어야 한다.

II 장에서는 ZnO 나노와이어를 이용한 압전 센서를 제작하고 구조적인 방식으로 센서의 민감도를 증가시는 연구를 진행했다. ZnO 나노와이어는 압전 물질이면서 n 형 반도체 특성을 가지는 물질이기 때문에 다양한 연구에서 활용되고 있다. 특히 ZnO 나노와이어의 압전 특성을 이용한 자가발전형 압력 센서는 가장 활발하게 연구되고 있는 분야 중 하나이다. 하지만 ZnO 나노와이어는 다양한 장점에도 불구하고 다른 압전 물질에 비해 낮은 압전 계수와 내부의 자유 전자에 의한 압전 효율의 감소 때문에 민감도와 전력 생산성을 개선하기 위한 연구가 많이 진행되고 있다. 따라서 본 연구에서도 ZnO 나노와이어를 이용한 압전 압력 센서를 제작하고 압력에 대한 민감도를 증가시키는 연구를 진행하였다. 일반적으로 ZnO 나노와이어는 n 형 반도체 물질이기 때문에 내부에 자유 전자를 많이 가지고 있다. 이 전자 들은 압전 쌍극자 모멘트가 발생할 때 압전 효과를 상쇄시키는 방향으로 이동 및 축적되기 때문에 이를 제거하기 위해 어닐링이나 도핑 같은 방식을 사용하여 전자를 제거하는 연구가 많이 보고되었지만 본 연구에서는 기존의 방식과 달리

간단하고 구조적인 방법을 사용하여 ZnO 나노와이어가 실제적으로 발생시키는 쌍극자 모멘트의 레벨을 증가시키는 방향으로 압력 센서의 민감도를 증가시키는데 성공했다. 주된 메커니즘은 Buckling effect 이다. Buckling effect 는 나노와이어와 같은 형태를 가진 구조체가 일정 레벨 이상의 힘을 받으면 급격하게 휘어지는 효과를 말한다. 급격하게 휘어질수록 압전 효과가 증가되기 때문에 이 효과를 일으킬 수 있는 나노와이어 숫자를 증가시키기 위해 반도체 공정을 통하여 나노와이어 사이에 공간을 만들어주는 패턴을 제작하였고 성장할 수 있는 공간을 제한하였다. 그 결과 실제로 사각 패턴의 가장자리 부분에 성장한 나노와이어들이 힘을 가했을 때 높은 레벨의 압전 효과를 발생시키는 것을 시뮬레이션을 통해 확인하고 실제 측정 결과에서도 패턴이 없을 때보다 약 3 배에서 최대 11 배 이상의 민감도와 전력생산성이 증가됨을 확인할 수 있었다.

III 장에서는 표면 정보를 수집하기 위해 PDMS 기반의 작고 간단한 구조물을 제작하고 촉각 센서에 적용시켜 표면 형태의 깊이, 간격, 경도 등을 알아올 수 있는 촉각 센서 제작에 대한 연구를 진행하였다. 이 구조물은 마치 인간의 지문과 비슷한 역할을 하기 위해 설계되었다. 먼저 촉각 센서가 표면을 문지를 때 센서와의 상호 작용을 하며 발생하는 전단력(shear force)를 수직력(Normal force)의 형태로 변형시키고 이를 촉각 센서에 전달하여 압전 신호를 증폭시켜 줄 수 있도록 하였다. 최적의 구조물 형태를 찾기 위해 먼저 원뿔, 원기둥, 반구 형태의 구조물 설계하여 시뮬레이션과 문지르기 실험 등을 진행하였다. 그 결과 반구 형태의 구조물이 내구성과 압전 신호 증폭 효과를 모두 만족하였다. 추가적으로 반구 형태의 높이에 따른 증폭 효과를 실험하기 위하여 100um 부터 500um 까지 반구 형태의 구조물을 설계하고 같은 실험을 진행한 결과 구조물의 형태가 높으면 높을수록 증폭 효과가 커짐을 확인하였다. 그리고 높이를 가지는 물체를 제작하였고 이를 문질러 표면 깊이에 대한 정보를 얻어올 수 있는지 확인하였다. 그 결과 문지름에 의해 발생된 압전 신호를 전하량의 형태로 바꿔 주면 문지르는 속도에 관계없이 깊이 정보를 얻어올 수 있음을 확인 하였다. 사용된 구조물이 500 um 높이를 가지기 때문에 깊이 정보 또한 500 um 까지 밖에 측정할 수 없는 단점이 있지만 인간 피부 역시 깊이 정보를 측정하는데 한계가 있는 만큼 표면 정보를 획득하는데 충분한 값이라 생각 한다. 또한 이 구조물을 통해 물체의 경도 역시 측정된 압전 신호의 기울기를 분석함으로써 알아올 수 있었다.

IV 장에서는 다기능 촉각 센싱 시스템을 위해 거칠기 센서에 대한 필요성을 느끼고 진행한 연구이다. 압력과 온도를 감지하는 수준을 넘어 거칠기를 느끼는 센서를 연구하는 것은 인간 촉각을 모사하기 위해 필요한 필수적인 단계이다. 일반적으로 거칠기는 다양한 촉각 정보의 혼합으로 결정된다고 알려져 있기 때문에 가장 모사하기 어렵다는 이유로 머신 러닝 등 신호처리 분야와의 협업이 많이 이루어지고 있는 실정이다. 그러므로 거칠기를

측정하기 위한 다양한 변수 중 센서로 표면 형태를 알아내기 위한 연구를 진행했다. 촉각 센서가 물체를 문지르면 위치에 따른 압전 신호를 측정하게 되고 그 압전 신호를 위치에 따라 대응시켜주면 문지른 물체의 표면 형태를 재구성할 수 있다. 특히 재구성된 이미지의 해상도를 증가시키기 위해 일반적인 십자 매트릭스 형태의 전극 구조를 사용하는 것이 아닌 지그-재그 구조의 전극 어레이를 적용시켰다. 그 결과 십자 매트릭스 전극 사이에서 손실되는 정보를 최소화하고 높은 해상도의 표면 정보를 재구성하는데 성공하였다. 또한 전극 사이에 추가적인 온도 센서를 배치함으로써 물체를 문지를 때 물체의 온도와 표면 형태에 대한 정보를 동시에 얻어올 수 있는 촉각 센서를 제작하였다.

V 장에서는 이전 장에서 연구한 센서를 기반으로 사람처럼 감각을 감지하고 모사하는 시스템을 구축하였다. 뾰족하고 뜨거운 물체를 만졌을 때 느끼는 고통을 모사하기 위해 고통 구분 및 위험신호 발생 알고리즘을 컴퓨터 프로그램(Labview)에 적용시키고 다채널 촉각 센서에서 발생한 신호를 수집하여 판단하도록 하였다. 그 결과 뾰족하고 뜨거운 물체를 구분하고 설정한 한계점을 넘었을 때 시스템이 위험 신호를 발생시킬 수 있음을 확인하였다. 물체의 거칠기를 감지하는 시스템 또한 구축하였다. 이를 위해 시스템에 머신 러닝을 적용시켰다. 머신 러닝을 이용한 타 연구에서는 기존에 학습된 물질을 단순히 매칭시키는 연구들이 대다수이다. 하지만 사람 같은 시스템을 구현하기 위해 실제 사람을 대상으로 42 개의 섬유 물질을 거칠기 순으로 배치하도록 하였고 이 데이터를 머신 러닝에 적용시켰다. 그 결과 41 개의 데이터를 바탕으로 학습되지 않은 나머지 1 개의 거칠기를 구분하는 시스템을 구현하는데 성공하였다.

결과적으로 본 연구는 압전 물질이 가지는 장점(전력소모, 동적 센싱, 간단한 공정과정 등)을 이용하여 자가 발전형 촉각 센서를 제작하였다. 비록 개선되어야 할 몇 가지 문제점이 있지만 이 연구는 압력, 온도, 표면 형태, 경도, 거칠기 등을 측정할 수 있는 조금 더 나은 촉각 센서 연구의 기반이 되는 연구이다. 본 연구의 결과는 앞으로 wearable 기기, 헬스케어 모니터링, 터치 패널, 로봇의 인공피부 등 다양한 분야에 적용될 수 있을 것이라 생각한다. 추후에 뇌 과학, 신호처리 등 다른 연구 분야와의 협업을 통해 촉각 센서가 앞서 언급한 표면 정보를 측정할 수 있을 뿐만 아니라 이 정보를 토대로 인간이 인지할 수 있는 정신 감각적인 부분을 모사하고 외부 환경과 감정적인 교류를 할 수 있는 촉각 시스템으로의 발전을 희망한다.

핵심어: 자가발전, ZnO Nanowire (산화아연 나노와이어), P(VDF-TrFE), 압력 센서, 온도 센서, 거칠기 센서.